Nanomaterials for Molecular Imaging: an Emerging Paradigm

By

Sixiang Shi

A dissertation submitted in partial fulfillment of

the requirements for the degree of

Doctor of Philosophy

(Materials Science)

at the

UNIVERSITY OF WISCONSIN-MADISON

2016

Date of final oral examination: 04/26/2016

The dissertation is approved by the following members of the Final Oral Committee:

Weibo Cai, Associate Professor, Materials Science Program

Ray Vanderby Jr., Professor, Materials Science Program

Shaoqin Gong, Professor, Materials Science Program

Xudong Wang, Associate Professor, Materials Science Program

Robert Jerry Nickles, Professor, Medical Physics

Abstract

Molecular imaging, the “visualization, characterization, and measurement of biological processes at the molecular and cellular levels in humans and other living systems”, has played an important role in cancer diagnosis. With the advances in nanotechnology, nanomaterials have emerged as a promising candidate for molecular imaging, due to their unique properties.

Graphene is one of the most promising nanomaterials, which is intrinsically useful for drug loading and photo therapy of cancer. However, in vivo biodistribution and tumor targeting with graphene nanomaterial is an underexplored area. In this dissertation, we designed a radiolabeled antibody conjugated reduced graphene oxide (RGO) nanoplatform for in vivo positron emission tomography (PET) and tumor vasculature targeting. Excellent tumor uptake was achieved with ^{64}Cu-NOTA-RGO-TRC105, compared to non-targeted RGO conjugate (^{64}Cu-NOTA-RGO). Various experiments were performed, demonstrating that the vasculature targeting is highly specific (Chapter 2). In the following study, graphene oxide (GO), another subtype of graphene nanomaterials, was conjugated with anti-angiogenesis protein vascular endothelial growth factor 121 ($VEGF_{121}$) to further validate the active targeting and imaging of graphene nanomaterials. Significantly enhanced tumor accumulation (>8 %ID/g) as well as high tumor-to-muscle contrast was achieved, showing great potential for future tumor targeted imaging (Chapter 3).

Although traditional chelators are generally utilized in radiolabeling and PET imaging of nanomaterials, a novel chelator-free radiolabeling approach was designed with graphene nanoparticles (Chapter 4). The chelator-free radiolabeled RGO possesses decent labeling

efficiency and enhanced in vivo radiostability over NOTA-chelated RGO, making it especially suitable for nanoparticle-based radiolabeling. Bypassing the use of chemical chelator, the intrinsically radiolabeled nanoparticles are able to maintain the native pharmacokinetics, and therefore more accurately reflect the distribution in vivo. Besides graphene, layered double hydroxide (LDH) and molybdenum disulfide (MoS_2) nanoparticles were also employed for chelator-free radiolabeling and examined in vivo (Chapter 5 and 6). Excellent tumor uptake and in vivo integrity were observed, further validating the potential of chelator-free labeling in molecular imaging.

Taking advantaging of molecular imaging and nanotechnology, a promising multifunctional nanoplatform can be designed for in vivo cancer management. Further efforts are necessary to thoroughly understand the in vivo behavior of nanoparticles and apply them in clinic.

Acknowledgements

I would like to thank, first and foremost, my advisor Prof. Weibo Cai. He has spent tremendous time and effort to guide me, seeing me growing up from a naive student to a self-motivated researcher. His expertise, enthusiasm, and scientific attitude have set the best model for me to explore the mysterious world of science. With time, he has become not only my teacher but also a friend in my life. The tense arguments about work, the heartfelt praise about my achievements, the constructive criticisms about my shortcomings, and the wonderful trips to the conferences: all together form some unforgettable memories of my graduate life.

I also want to thank all the committee members. Prof. Ray Vanderby was the Chair of my program. He provided me with invaluable help and support during my graduate study. I still remember his firm handshake after I completed my RRE presentation, which was the best encouragement prompting me bravely face all the difficulties. Prof. Shaoqin Gong and Prof. Xudong Wang were the teachers of the most attractive courses that I have taken. The knowledge I gained from them in class and the suggestions I got out of the class have become some precious treasures of mine. I want to give my special thanks to Prof. Jerry Nickles, as well as the whole cyclotron gang, including Dr. Todd Barnhart, Hector Valdovinos and Stephen Graves, for the great collaboration during the past five years. Whenever we had any new idea, he was always ready to provide insightful suggestions, and we always got the first access to the new isotopes. Without the support from him and his group, none of our work would have been possible.

In addition, I want to thank all Cai group labmates. Dr. Hao Hong and Dr. Feng Chen were my mentors who taught me how to conceive ideas, how to conduct experiments, and how to process the data. They also acted as my elder brothers to provide the kindest help and support whenever I had any difficulty. Shreya Goel was my best friend in the lab. We have always been working together in the lab. The days and nights that we spent in culturing cells, scanning mice and weighting tubes have become my best time in the graduate life. She also offered tremendous help in my work. All of my writing drafts were firstly revised by her. I want to thank Dr. Haiming Luo, Dr. Liang Cheng, Dr. Yunan Yang, Reinier Hernandez, Dr. Yin Zhang, Dr. Tapas Nayak, Dr. Hakan Orbay, Dr. Haiyan Sun, Emily Ehlerding, Cheng Xu, Dr. Yonghua Zhan, Dr. Anyanee Kamkaew, Dr. Christopher England, Dr. Dawei Jiang and other labmates for the kind help in my research and the happy time that we have spent together. Also thank my undergraduate students Jakob Ohman, Brianne Fliss and Lazura Krasteva for trusting me and working with me.

Furthermore, I want to thank all the other professors, staffs and students who have helped me or collaborated with me in the University of Wisconsin-Madison or other institutes. Diana Rhoads was the program associate in Materials Science Program. She has offered me great help throughout my graduate study. Prof. Jamey Weichert, Justin Jeffery and Mohammed Farhoud in the small animal imaging facility provided the scanning instruments and services which were one of the essential parts of my studies. I want to thank my friends in Materials Science Program, including Zhe Wang, Shenzhen Xu, Xiangyu Xia, Xing Wang and Guojun Chen, for the warm help and the happy times that we have shared. I also appreciate Prof. Zhuang Liu and his students Dr. Kai Yang and Teng Liu from Soochow University, Prof. Zhi Ping Xu and his

students Zi Gu and Yian Zhu from the University of Queensland, Prof. Jonathan Lovell and his student Yumiao Zhang from the University at Buffalo for the exciting collaborations.

Last but not least, I want to thank my parents, grandparents and other family members for their unconditional love and support. Although they are in the distant hometown, their love has always accompanied me and guarded me during my past happy but difficult five years.

Abbreviations

%ID/g	Percentage injected dose per gram
AFM	Atomic force microscopy
CT	X-ray computed tomography
EDTA	Ethylenediaminetetraacetic acid
EPR	Enhanced permeability and retention
DLS	Dynamic light scattering
DMSA	Meso-2,3-dimercaptosuccinnic acid
DOTA	1,4,7,10-tetraazacyclododecane-1,4,7,10-tetraacetic acid
DOX	Doxorubicin
FACS	Fluorescence activated cell sorting
FITC	Fluorescein isothiocyanate
FTIR	Fourier transform infrared spectroscopy
GO	Graphene oxide
HEPES	4-(2-hydroxyethyl)-1-piperazineethanesulfonic acid
HUVEC	Human umbilical vein endothelial cell
IgG	Immunoglobulin G
IONP	Iron oxide nanoparticle
LDH	Layered double hydroxide
MoS_2	Molybdenum disulfide
MR	Magnetic resonance
MRI	Magnetic resonance imaging

NIR	Near-infrared
NOTA	1,4,7-triazacyclononane-1,4,7-triacetic acid
p-SCN-Bn-NOTA	2-S-(4-isothiocyanatobenzyl)-1,4,7-triazacyclononane-1,4,7-triacetic acid
p.i.	Post-injection
PDI	Polydispersity index
PEG	Polyethylene glycol
PET	Positron emission tomography
RES	Reticuloendothelial system
RGO	Reduced graphene oxide
ROI	Region-of-interest
SCM-PEG-Mal	Succinimidyl carboxymethyl PEG maleimide
SEM	Scanning electron microscopy
SH	Thiol
SPECT	Single-photon emission computed tomography
SPION	Superparamagnetic iron oxide
TCEP	Tris(2-carboxyethyl)phosphine
TEM	Transmission electron microscopy
TETA	1,4,8,11-tetraazacyclotetradecane-1,4,8,11-tetraacetic acid
THF	Tetrahydrofuran
TLC	Thin layer chromatography
VEGF	Vascular endothelial growth factor
VEGFR	Vascular endothelial growth factor receptor

Table of Contents

List of Figures

Chapter 1 Introduction

Molecular imaging is the visualization, characterization, and measurement of biological processes at the molecular and cellular levels in humans and other living systems (Society of Nuclear Medicine; http://www.snm.org/index.cfm?PageID=11202). Compared with conventional in vitro imaging techniques, in vivo molecular imaging provides distinct advantages. Via molecular imaging, both the temporal and the spatial biodistribution of a molecular probe and related biological processes can be non-invasively determined in living subjects [1]. Molecular imaging enables disease diagnosis in the earliest pre-symptomatic stage, allows real-time assessment of therapeutic and surgical efficacy, and novel methods to manage symptoms that reduce the quality of life, especially in cancer [2]. Among all the imaging techniques, PET is a highly sensitive and quantitative technique with unlimited tissue penetration, which has become a useful tool for in vivo molecular imaging, treatment monitoring and patient stratification. Besides PET, other imaging modalities including SPECT, optical imaging, MR imaging, ultrasound imaging and photoacoustic imaging have also been employed to achieve molecular and functional information from living systems due to their respective merits[1, 3].

Numerous kinds of agents have been developed for molecular imaging, such as small molecule [4], peptide [5], protein [6], antibody [7], virus [8], cell [9], and particle [2]. Especially, with the advances in nanotechnology, nanomaterials have emerged as a promising platform for molecular imaging. Due to the ultra-small size and extremely large surface-to-volume ratio, nanomaterials-based molecular imaging affords many advantages over conventional approaches [10]. First, more imaging labels or a combination of labels for different modalities can be linked to a single

nanoparticle, thereby leading to dramatic signal amplification. Secondly, larger amount or multiple kinds of targeting ligands can be simultaneously conjugated onto the surface of the nanoparticles, so as to achieve significantly enhance targeting efficiency and specificity. In addition, functionalized nanoparticles can load anticancer drugs or intrinsically serve as therapeutic agents for chemotherapy, photothermal therapy, photodynamic therapy etc, which enables effective tumor eradication [11-13]. Therefore, ingenious combination of nanomaterials with molecular imaging creates a promising theranostic paradigm, which offers superb access to precisely understand and control the in vivo fate (such as pharmacokinetics and pharmacodynamics) of nanomaterials, eventually benefiting the progress and bench-to-bedside transition of nanooncology.

Various kinds of nanoparticles have been developed for molecular imaging and potential therapy. The most well-studied nanomaterials include quantum dots [14, 15], carbon nanotubes [16, 17], nanoshells [18], paramagnetic nanoparticles [19], and many others [10]. In this dissertation, several new nanomaterials, graphene, LDH and MoS_2 nanoparticles are utilized for in vivo tumor imaging. Unlike the conventional spherical nanoparticles, graphene, LDH and MoS_2 nanoparticles exist as ultra-thin sheets or layers. Their extremely large surface can serve as the most desired platform to load chemical drug for cancer therapy or decorate functional agents for enriched functionalities. Surface engineering is critical to fulfill the in vivo applications of nanomaterials. In my study, PEG or BSA were modified on the nanoparticles to improve their in vivo stability and provide functional groups (e.g. NH_2 groups) for further functionalization. The abundant NH_2 groups can be used for covalent conjugation of NOTA for ^{64}Cu labeling, or conjugation of antibodies/proteins for enhanced tumor targeting efficiency and specificity.

Tumor angiogenesis targeting was achieved, by which the nanoparticles can accumulate in the tumor site without the need of extravasation, opening up new perspectives for future research on cancer theranostics using nanomaterials.

Although several nanoparticles have been labeled with radioisotopes and examined by PET imaging in tumor-bearing mice in our studies, radiolabeling is still challenging due to the limitation of coordination chemistry of chelators. Chelator-free labeling with nanoparticles is a relatively unexplored but rapidly surging area of research. Compared with conventional chelator-based labeling, chelator-free labeling can maintain the native properties (e.g. size, structure, drug loading capacity and pharmacokinetics) of nanoparticles, which enables a more precise control over their in vivo fate and thereby aid in their further applications including cancer imaging and therapy. By investigating the labeling efficiency and stability with different nanoparticles, this dissertation might provide important guidance for the future research on chelator-free labeling.

Chapter 2 Tumor Vasculature Targeting and Imaging with Reduced Graphene Oxide

2.1. Background

Graphene, an intriguing nanomaterial with unique mechanical, electronic, optical, and chemical properties, has attracted tremendous interest over the last several years [20-25]. Ultrahigh surface area, excellent electrical conductivity, ideal photothermal property, versatile chemistry, and low toxicity allow graphene-based nanomaterials to have applications in biosensing, tissue engineering, drug delivery, molecular imaging, photothermal therapy, among others [26-29].

An emerging strategy for the development of new anti-cancer therapies is to harness the potential of nanotechnology to improve the therapeutic efficacy [30-32]. Among the different subtypes of graphene-based nanomaterials, RGO is an excellent photothermal agent that enables highly efficient in vivo tumor ablation [33]. In addition, RGO can be used to integrate imaging and therapeutic components for cancer theranostics [34]. Despite the many desirable properties for biomedical applications, the use of RGO conjugates for in vivo tumor targeting has not been reported, which is the focus of this study.

The size of nanomaterials is a significant barrier for extravasation, which limits the use of various nanomaterials for tumor targeting, imaging and therapy [10, 35, 36]. We believe tumor vasculature instead of tumor cell targeting is more desirable for graphene-based nanomaterials, since the targets are immediately accessible upon intravenous injection and extravasation is not required to achieve tumor targeting/contrast. Furthermore, angiogenesis (i.e., new blood vessel

formation) is a critical process in tumor development and metastasis, hence is applicable to all solid tumors [37]. CD105 (i.e., endoglin) is almost exclusively expressed on proliferating tumor endothelial cells, which serves as an ideal vascular target [38-40]. More importantly, the expression level of CD105 is correlated with poor prognosis in more than 10 solid tumor types [41], which makes it a generally applicable prognostic, diagnostic, and therapeutic vascular target in cancer. TRC105, a human/murine chimeric IgG1 monoclonal antibody which binds to both human and murine CD105 [42], was used as the targeting ligand in this work.

The goal of this study was to investigate in vivo tumor vasculature targeting with TRC105-conjugated RGO, which can be non-invasively and quantitatively measured with serial PET imaging. Since PET is widely used in clinical oncology [43-46], the incorporation of a PET isotope in the RGO conjugates can facilitate future translation of graphene-based nanomaterials. PEG chains (5 kDa) were used to modify the surface of RGO for enhanced in vivo stability and biocompatibility, with amine groups at the terminal end for covalent conjugation of various functional entities. ^{64}Cu (half-life: 12.7 h) was used as the PET label, with 1,4,7-triazacyclononane-1,4,7-triacetic acid (NOTA) as the chelator. To demonstrate CD105 specificity of TRC105-conjugated RGO, various in vitro, in vivo, and ex vivo experiments were carried out.

2.2. Materials and methods

2.2.1. Reagents

TRC105 was provided by TRACON Pharmaceuticals Inc. (San Diego, CA). p-SCN-Bn-NOTA was purchased from Macrocyclics, Inc. (Dallas, TX). Chelex 100 resin (50-100 mesh) and FITC

were purchased from Sigma-Aldrich (St. Louis, MO). SCM-PEG-Mal (molecular weight: 5 kDa; Creative PEGworks, Winston Salem, NC), rat anti-mouse CD31 primary antibody (BD Biosciences, San Diego, CA), AlexaFluor488- or Cy3-labeled secondary antibodies (Jackson Immunoresearch Laboratories, Inc., West Grove, CA), and PD-10 desalting columns (GE Healthcare, Piscataway, NJ) were all acquired from commercial sources. Water and all buffers were of Millipore grade and pre-treated with Chelex 100 resin to ensure that the aqueous solution was free of heavy metal. All other reaction buffers and chemicals were obtained from Thermo Fisher Scientific (Fair Lawn, NJ).

2.2.2. Syntheses of the RGO conjugates

RGO-PEG-NH_2 was prepared in a similar fashion as detailed in our previous report [33]. In brief, PEG grafted poly(maleic anhydride-alt-1-octadecene) (abbreviated as C_{18}PMH-PEG_{5000}-NH_2) was synthesized following our previously reported procedure [47]. A 3:1 ratio of mPEG-NH_2 (5 kDa, PEG Bio, China) and Boc-NH-PEG-NH_2 (5 kDa, IRIS Biotech GmbH, Germany) was used to react with C_{18}PMH, obtaining C_{18}PMH-PEG_{5000}-NH_2 after deprotection of the Boc group with trifluoroacetic acid. The C_{18}PMH-PEG_{5000}-NH_2 solution was dialyzed against water using a 14 kDa molecular weight cut-off (MWCO) membrane and then lyophilized. To functionalize RGO via hydrophobic interactions between the C_{18} chains and the RGO surface, 10 mg of C_{18}PMH-PEG_{5000}-NH_2 was mixed with 1 mg of RGO and sonicated for 90 min to yield RGO-PEG-NH_2 (Figure 2.1A). The suspension was centrifuged at 14,800 rpm for 3 h to remove any unstable aggregates. The supernatant was collected and washed through 100 nm filter membrane to remove excess C_{18}PMH-PEG_{5000}-NH_2.

RGO-PEG-NH_2 was mixed with p-SCN-Bn-NOTA or FITC, which has the same chemical reaction between the SCN group and the NH_2 group on RGO, at a molar ratio of 1:10 at pH 9.0 for 2 h. The resulting NOTA-RGO (or FITC-RGO) was purified by centrifugation with 100 kDa MWCO Amicon filters at 8,000 rpm for 15 min. Of note, most NH_2 groups are still present on the surface of NOTA-RGO and FITC-RGO for further functionalization with SCM-PEG-Mal. Subsequently, NOTA-RGO (or FITC-RGO) was reacted with SCM-PEG-Mal at a molar ratio of 1:30 at pH 8.5 for 2 h. The resulting NOTA-RGO-PEG-Mal or FITC-RGO-PEG-Mal was purified by centrifugation with 100 kDa MWCO Amicon filters at 8,000 rpm for 15min.

TRC105 was incubated with Traut's reagent at a molar ratio of 1:25 at pH 8.0 for 2 h. The resulting TRC105-SH was purified by size exclusion column chromatography with PBS (pre-treated with Chelex 100 resin to prevent oxidation of the thiol) as the mobile phase. Afterwards, NOTA-RGO-PEG-Mal (or FITC-RGO-PEG-Mal) was reacted with TRC105-SH at a molar of 1:5 at pH 7.5 in the presence of TCEP (to prevent oxidation of the thiol). The final products were purified by size exclusion column chromatography and termed as NOTA-RGO-TRC105 or FITC-RGO-TRC105.

Although all the RGO conjugates (i.e., NOTA-RGO-TRC105, FITC-RGO-TRC105, NOTA-RGO, and FITC-RGO) have PEG chains on the surface, the term "PEG" was not included in the names for brevity consideration. SEM, AFM, DLS, and zeta-potential measurements were performed to characterize the RGO conjugates.

2.2.3. Cell lines and animal model

4T1 murine breast cancer, MCF-7 human breast cancer, and HUVECs were obtained from the American Type Culture Collection (ATCC, Manassas, VA) and cultured as previously described [33, 48, 49]. Cells were used for in vitro and in vivo experiments when they reached ~80% confluence. All animal studies were conducted under a protocol approved by the University of Wisconsin Institutional Animal Care and Use Committee. Four- to five-week-old female BALB/c mice (Harlan, Indianapolis, IN) were each injected with 2×10^6 4T1 cells in the flank to generate the 4T1 breast cancer model. The mice were used for in vivo experiments when the tumor diameter reached 6-8 mm.

2.2.4. Flow cytometry

HUVECs (CD105 positive) and MCF-7 (CD105 negative) cells [33] were harvested and suspended in cold PBS with 2% bovine serum albumin at a concentration of 5×10^6 cells/mL, incubated with FITC-RGO-TRC105 or FITC-RGO at a concentration of 50 μg/mL (based on RGO) for 30 min at room temperature, centrifuged at 1,000 rpm for 5 min, and washed three times with cold PBS. To further evaluate CD105 specificity of FITC-RGO-TRC105, a blocking experiment was carried out where 500 μg/mL of TRC105 was added to the incubated cells. Subsequently, the cells were analyzed using a BD FACSCalibur 4-color analysis cytometer equipped with 488 nm and 633 nm lasers (Becton-Dickinson, San Jose, CA) and FlowJo analysis software (Tree Star, Inc., Ashland, OR).

2.2.5. ^{64}Cu-labeling and serum stability studies

^{64}Cu was produced with an onsite cyclotron (GE PETrace). $^{64}CuCl_2$ (74 MBq) was diluted in 300 µL of 0.1 M sodium acetate buffer (pH 6.5) and mixed with 50 µg of NOTA-RGO-TRC105 or NOTA-RGO. The reaction was conducted at 37 ºC for 30 min with constant shaking. The resulting ^{64}Cu-NOTA-RGO-TRC105 or ^{64}Cu-NOTA-RGO was purified by size exclusion column chromatography using PBS as the mobile phase. The radioactive fractions containing ^{64}Cu-NOTA-RGO-TRC105 or ^{64}Cu-NOTA-RGO were collected for further in vitro and in vivo studies.

To ensure that ^{64}Cu-NOTA-RGO-TRC105 and ^{64}Cu-NOTA-RGO are sufficiently stable for in vivo applications, serum stability studies were carried out. ^{64}Cu-NOTA-RGO-TRC105 or ^{64}Cu-NOTA-RGO were incubated in complete mouse serum at 37 °C for up to 48 h. Portions of the mixture were sampled at different time points and filtered through 100 kDa MWCO filters. The radioactivity within the filtrate was measured, and the percentages of retained (i.e., intact) ^{64}Cu on the RGO conjugates (^{64}Cu-NOTA-RGO-TRC105 or ^{64}Cu-NOTA-RGO) were calculated using the equation (total radioactivity - radioactivity in filtrate)/total radioactivity × 100%.

2.2.6. PET imaging and biodistribution studies

PET scans of 4T1 tumor-bearing mice (4 mice per group), at various time points p.i. of 5-10 MBq of ^{64}Cu-NOTA-RGO-TRC105 or ^{64}Cu-NOTA-RGO via tail vein, were performed using a microPET/microCT Inveon rodent model scanner (Siemens Medical Solutions USA, Inc.). Detailed procedures for data acquisition, image reconstruction, and ROI analysis of the PET data have been reported previously [33, 48]. Quantitative PET data of the 4T1 tumor and major organs were presented as %ID/g of tissue.

To confirm in vivo CD105 specificity of ^{64}Cu-NOTA-RGO-TRC105, another group of four 4T1 tumor-bearing mice were each injected with 1 mg of TRC105 at 2 h before ^{64}Cu-NOTA-RGO-TRC105 administration and subsequent serial PET imaging. To validate that the %ID/g values based on PET imaging accurately reflected the radioactivity distribution in tumor-bearing mice, biodistribution studies were conducted at 48 h p.i. (at the end of serial PET scans) and 3 h p.i. (when the tumor uptake was at the peak, using a separate cohort of four mice). Mice were euthanized and blood, 4T1 tumor, and major organs/tissues were collected and wet-weighed. The radioactivity in the tissue was measured using a γ counter (PerkinElmer) and presented as %ID/g (mean ± SD).

2.2.7. Histology

A group of three 4T1 tumor-bearing mice was each injected with NOTA-RGO-TRC105 (5 mg/kg of mouse body weight) and euthanized at 3 h p.i. (when 4T1 tumor uptake was at the peak based on PET imaging). The 4T1 tumor, liver, spleen (which has high uptake of ^{64}Cu-NOTA-RGO-TRC105), and muscle (which has low uptake of ^{64}Cu-NOTA-RGO-TRC105 and serves as a control normal organ) were frozen and cryo-sectioned for histological analysis.

Frozen tissue slices of 7 μm thickness were fixed with cold acetone and stained for endothelial marker CD31, as described previously through the use of a rat anti-mouse CD31 antibody and a Cy3-labeled donkey anti-rat IgG [33, 48]. The tissue slices were also incubated with 2 μg/mL of AlexaFluor488-labeled goat anti-human IgG for visualization of NOTA-RGO-TRC105 (i.e., TRC105 within the NOTA-RGO-TRC105 conjugate served as a primary antibody and no

additional TRC105 was used for histology studies). All images were acquired with a Nikon Eclipse Ti microscope.

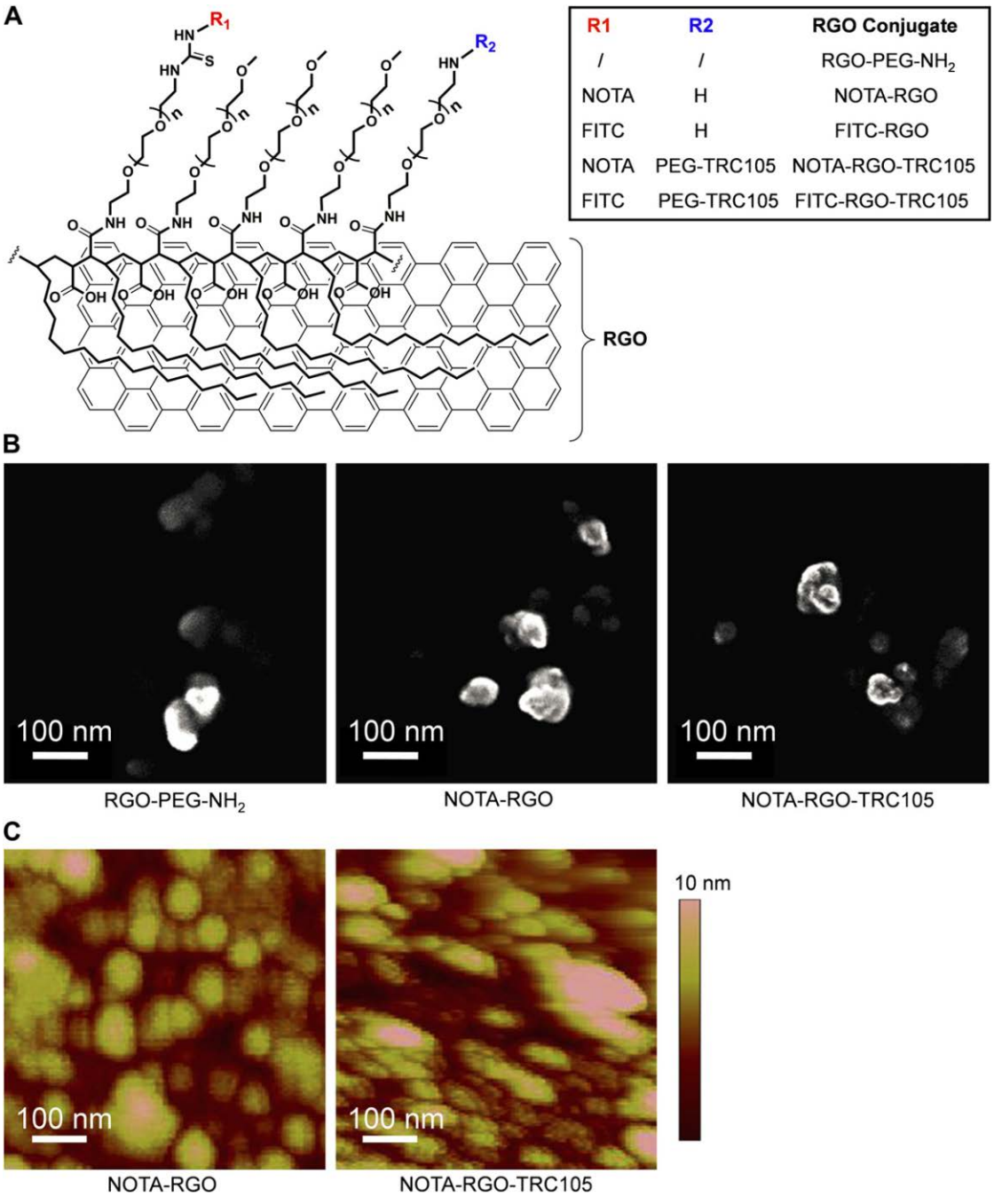

Figure 2.1. (**A**) A schematic diagram of the RGO conjugates. (**B**) SEM images of the RGO conjugates. (**C**) AFM images of the RGO conjugates.

2.3. Results

2.3.1. Syntheses and characterization of the RGO conjugates

A schematic structure of the RGO conjugates is shown in Figure 2.1A. Based on SEM and AFM measurements, RGO-PEG-NH_2, NOTA-RGO, and NOTA-RGO-TRC105 exist as small sheets within a size range of 20-80 nm (Figure 2.1B,C). DLS measurement showed that RGO-PEG-NH_2 has a hydrodynamic diameter of 22.3 ± 3.2 nm, whereas the diameter of NOTA-RGO and NOTA-RGO-TRC105 are 26.2 ± 3.6 nm and 37.0 ± 7.2 nm, respectively. The zeta-potential value of RGO-PEG-NH_2 was -20.3 ± 1.6 mV (which is expected since there are more $–COO^-$ on the RGO surface than $–NH_3^+$). After further conjugation, the zeta-potential values changed significantly to -16.4 ± 4.6 mV (NOTA-RGO) and -2.0 ± 5.2 mV (NOTA-RGO-TRC105), suggesting successful conjugation of NOTA and TRC105 onto the surface of RGO.

2.3.2. Flow cytometry and serum stability studies

As evidenced in Figure 2.2A, the fluorescence signal of CD105 positive HUVECs was significantly enhanced (~25 fold higher than the untreated cells) upon incubation with FITC-RGO-TRC105, whereas no fluorescence enhancement was observed after blocking (with TRC105) or upon FITC-RGO treatment. On CD105 negative MCF-7 cells, the fluorescence signal was minimal for all groups. Taken together, flow cytometry results indicated high CD105 specificity and minimal non-specific binding of TRC105-conjugated RGO in cell culture.

Serum stability studies confirmed that ^{64}Cu-NOTA-RGO-TRC105 and ^{64}Cu-NOTA-RGO are highly stable for in vivo applications. Nearly 90% of ^{64}Cu remained on the RGO conjugates after incubation in complete mouse serum at 37 ºC for 48 h (Figure 2.2B), indicating excellent

stability of the radiolabel (i.e., ^{64}Cu) on NOTA-RGO and NOTA-RGO-TRC105. Since PET imaging detects the radiolabel rather than the RGO conjugates per se, excellent stability of the radiolabel on the RGO conjugates ensures that the signal observed with PET imaging truly reflects distribution of the RGO conjugates.

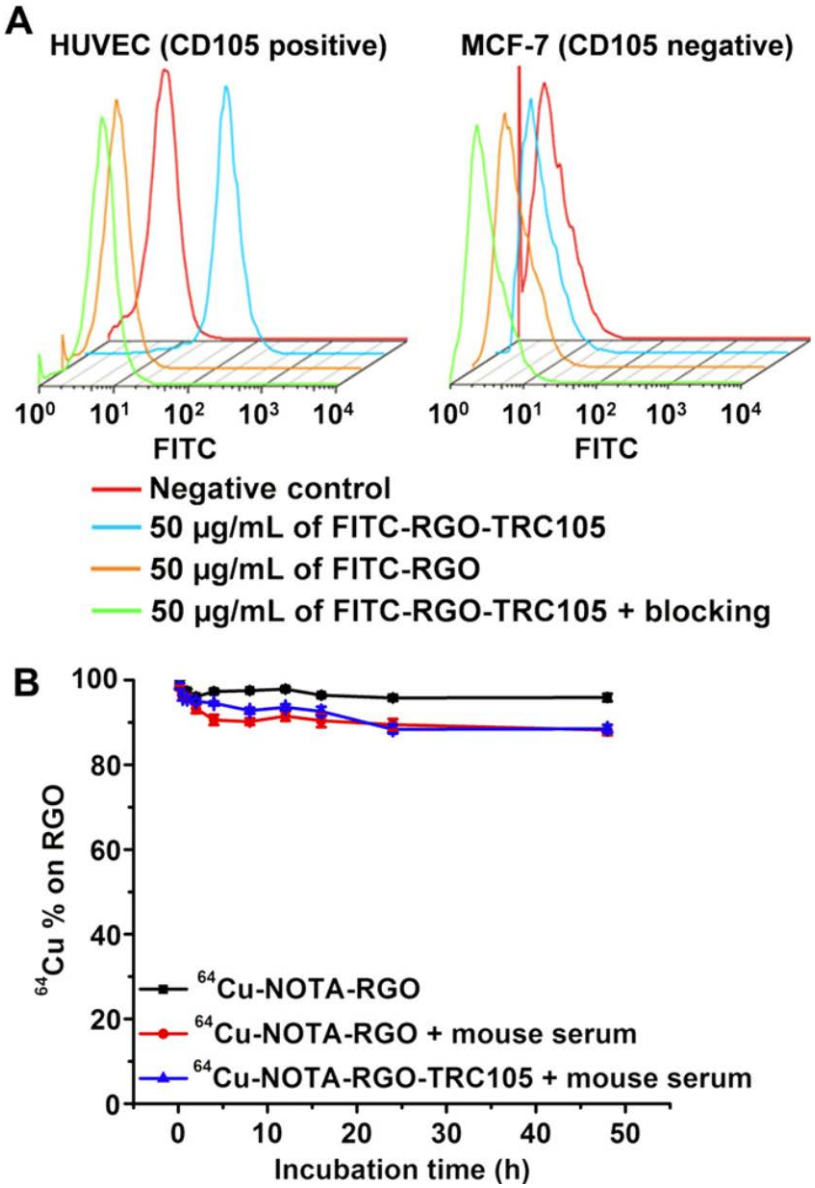

Figure 2.2. (**A**) Flow cytometry analysis of RGO conjugates in HUVECs (CD105 positive) and MCF-7 breast cancer cells (CD105 negative). (**B**) Serum stability studies at 37 ºC.

2.3.3. PET and biodistribution studies

^{64}Cu has a 12.7 h decay half-life. Therefore, the time points of 0.5, 3, 6, 16, 24 and 48 h p.i. were chosen for serial PET scans in 4T1 tumor-bearing mice. The coronal PET images that contain the 4T1 tumors are shown in Figure 2.3, and the quantitative data obtained from ROI analysis of the PET data are shown in Figure 2.4.

Since the size of RGO conjugates is significantly larger than the cutoff for renal filtration (~5 nm) [50], they were cleared from mice mainly through the hepatobiliary pathway. The liver uptake of ^{64}Cu-NOTA-RGO-TRC105 was 18.3 ± 2.8, 16.7 ± 0.9, 16.7 ± 2.0, 13.4 ±1.0, 13.5 ± 0.9, and 11.5 ± 0.5 %ID/g at 0.5, 3, 6, 16, 24, and 48 h p.i. respectively, while the radioactivity in the blood was 4.6 ± 1.6, 3.6 ± 0.4, 3.7 ± 0.5, 3.2 ± 0.1, 3.1 ± 0.1, and 2.9 ± 0.1 %ID/g at 0.5, 3, 6, 16, 24, and 48 h p.i. respectively (n = 4; Figure 2.4A), indicating a short circulation half-life (< 30 min). Importantly, the 4T1 tumor uptake of ^{64}Cu-NOTA-RGO-TRC105 was clearly visible at 0.5 h p.i. (Figure 2.3) and remained stable over time (5.0 ± 0.6, 5.6 ± 0.2, 5.7 ± 0.2, 4.8 ± 0.3, 4.5 ± 0.4, and 4.0 ± 0.5 %ID/g at 0.5, 3, 6, 16, 24, and 48 h p.i. respectively; n = 4; Figure 2.4A,D), which provided excellent tumor contrast.

Pre-injection of a blocking dose of TRC105 significantly reduced the 4T1 tumor uptake of ^{64}Cu-NOTA-RGO-TRC105 to 2.1 ± 0.4, 2.2 ± 0.3, 2.4 ± 0.3, 2.4 ± 0.3, 2.5 ± 0.2, and 2.4 ± 0.3 %ID/g at 0.5, 3, 6, 16, 24, and 48 h p.i. respectively (n = 4; Figure 2.3, 2.4B,D; $P < 0.05$ at all time points when compared to mice injected with ^{64}Cu-NOTA-RGO-TRC105 alone), which demonstrated in vivo specificity of ^{64}Cu-NOTA-RGO-TRC105 for CD105 expressed by

proliferating tumor vasculature. Radioactivity uptake of the liver in the group pre-injected with a blocking dose of TRC105 was similar to mice injected with ^{64}Cu-NOTA-RGO-TRC105 alone, which were 15.6 ± 1.8, 14.4 ± 1.3, 12.7 ± 1.6, 9.9 ± 1.3, 9.7 ± 1.1, and 7.8 ± 1.2 %ID/g at 0.5, 3, 6, 16, 24, and 48 h p.i. respectively (n = 4; Figure 2.4B). Radioactivity in the blood (2.8 ± 0.1, 2.9 ± 0.3, 3.3 ± 0.3, 3.4 ± 0.3, 3.3 ± 0.2, and 3.0 ± 0.4 %ID/g at 0.5, 3, 6, 16, 24, and 48 h p.i. respectively; n = 4; Figure 2.4B) was slightly affected by the blocking dose of TRC105 (i.e., lower blood radioactivity at early time points).

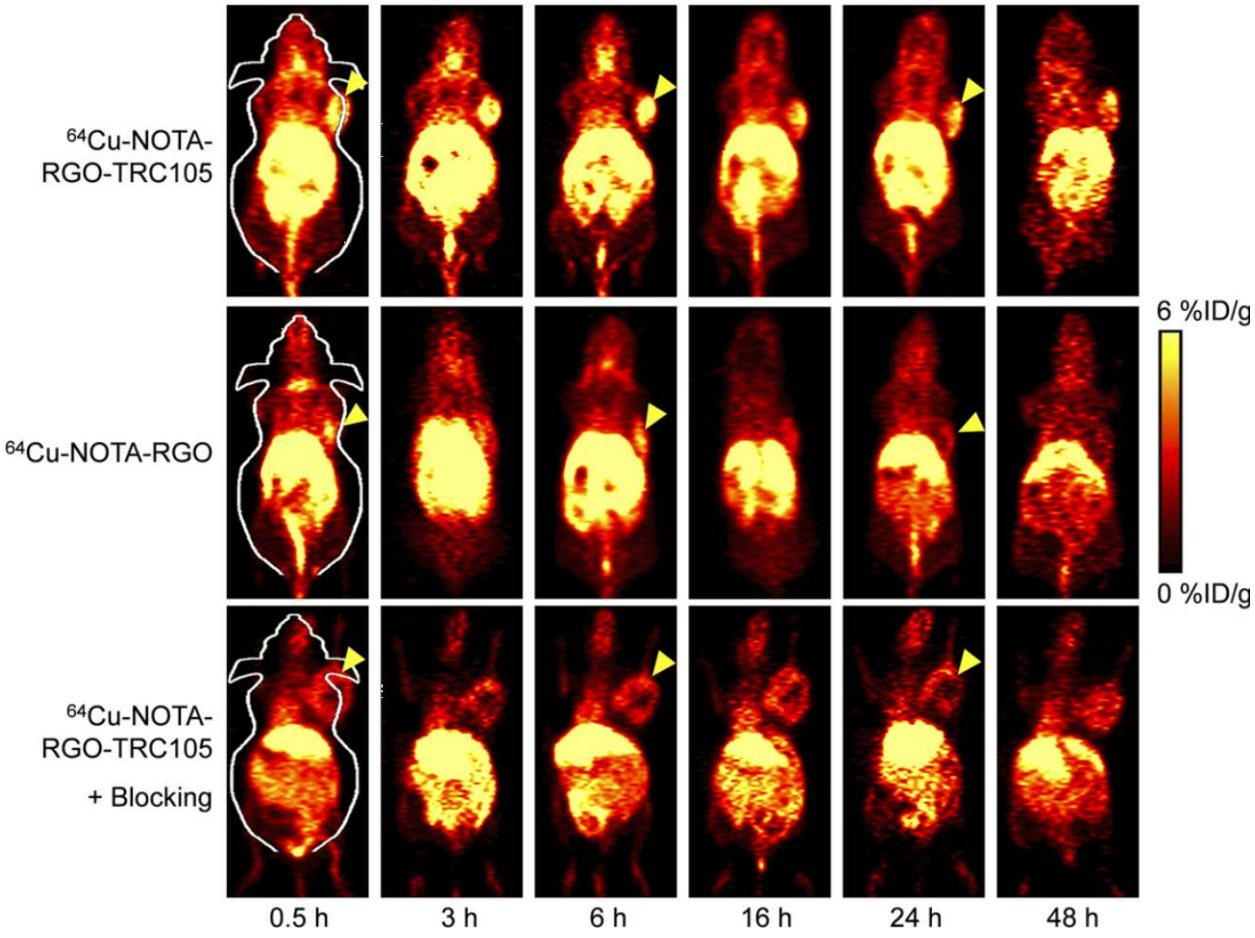

Figure 2.3. Serial coronal PET images of 4T1 tumor-bearing mice at different time points post-injection of ^{64}Cu-NOTA-RGO-TRC105, ^{64}Cu-NOTA-RGO, or ^{64}Cu-NOTA-RGO-TRC105 after a pre-injected blocking dose of TRC105. Tumors are indicated by arrowheads.

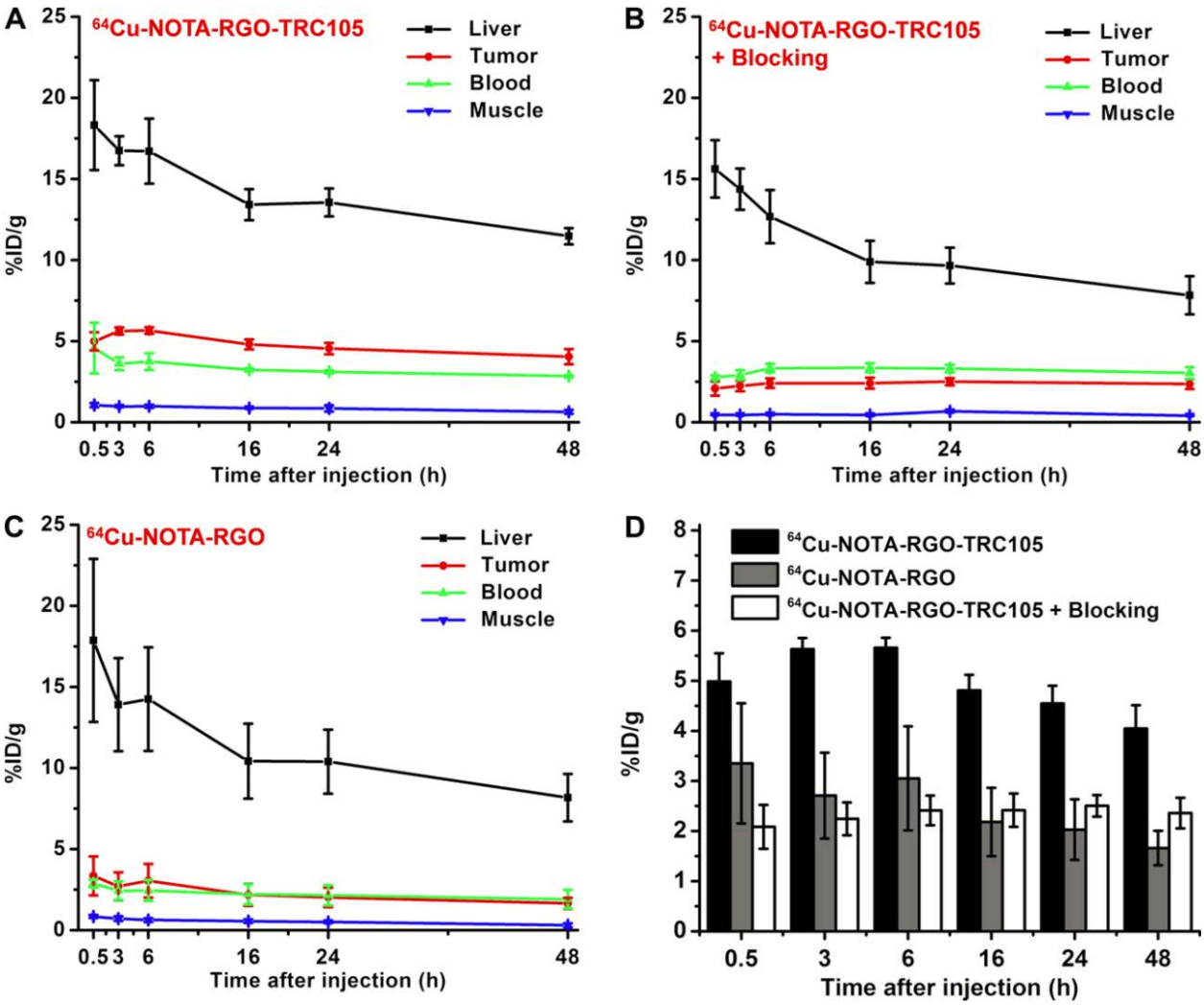

Figure 2.4. Quantitative analysis of the PET data. (**A**) Time□activity curves of the liver, 4T1 tumor, blood, and muscle upon intravenous injection of ^{64}Cu-NOTA-RGO-TRC105. (**B**) Time□activity curves of the liver, 4T1 tumor, blood, and muscle upon intravenous injection of ^{64}Cu-NOTA-RGO-TRC105, after a blocking dose of TRC105. (**C**) Time□activity curves of the liver, 4T1 tumor, blood, and muscle upon intravenous injection of ^{64}Cu-NOTA-RGO. (**D**) Comparison of the 4T1 tumor uptake in the three groups. The differences between 4T1 tumor uptake of ^{64}Cu-NOTA-RGO-TRC105 and the two control groups were statistically significant ($P < 0.05$) at all time points, except at 0.5 h post-injection between ^{64}Cu-NOTA-RGO-TRC105 and ^{64}Cu-NOTA-RGO. All data represent 4 mice per group.

The 4T1 tumor uptake of ^{64}Cu-NOTA-RGO (3.4 ± 1.2, 2.7 ± 0.9, 3.1 ± 1.0, 2.2 ± 0.7, 2.0 ± 0.6, and 1.7 ± 0.3 %ID/g at 0.5, 3, 6, 16, 24, and 48 h p.i. respectively; n = 4; Figure 2.4C,D) was ~2 fold lower than that of ^{64}Cu-NOTA-RGO-TRC105 ($P < 0.05$ at all time points except 0.5 h p.i.), indicating that conjugation of TRC105 to RGO markedly increased tumor uptake through active targeting of CD105 on the tumor vasculature. Liver uptake (17.9 ± 5.0, 13.9 ± 2.9, 14.3 ± 3.2, 10.4 ± 2.3, 10.4 ± 2.0, and 8.2 ± 1.5 %ID/g at 0.5, 3, 6, 16, 24, and 48 h p.i. respectively; n = 4; Figure 2.4C) and radioactivity in the blood (2.9 ± 0.2, 2.4 ± 0.6, 2.5 ± 0.6, 2.2 ± 0.6, 2.2 ± 0.6, and 1.9 ± 0.6 %ID/g at 0.5, 3, 6, 16, 24, and 48 h p.i. respectively; n = 4; Figure 2.4C) for ^{64}Cu-NOTA-RGO were similar as those of mice injected with ^{64}Cu-NOTA-RGO-TRC105.

Biodistribution studies were carried out at 3 h p.i. (Figure 2.5A, when tumor uptake was at the peak based on PET imaging) and 48 h p.i. (Figure 2.5B, following the last PET scans) to validate the PET results. Overall, the quantitative results based on PET and biodistribution studies matched very well, confirming that serial non-invasive PET imaging accurately reflected the distribution of ^{64}Cu-NOTA-RGO-TRC105 and ^{64}Cu-NOTA-RGO in tumor-bearing mice. Because of uptake in the RES and hepatobiliary clearance which is commonly observed for intravenously injected nanomaterials, substantial radioactivity was detected in the liver, spleen, and intestine. Importantly, even at 48 h p.i., the tumor uptake of ^{64}Cu-NOTA-RGO-TRC105 was significantly higher than that of ^{64}Cu-NOTA-RGO and the blocking group, indicating that vascular CD105 targeting with TRC105 as the ligand could effectively enhance the tumor uptake in vivo.

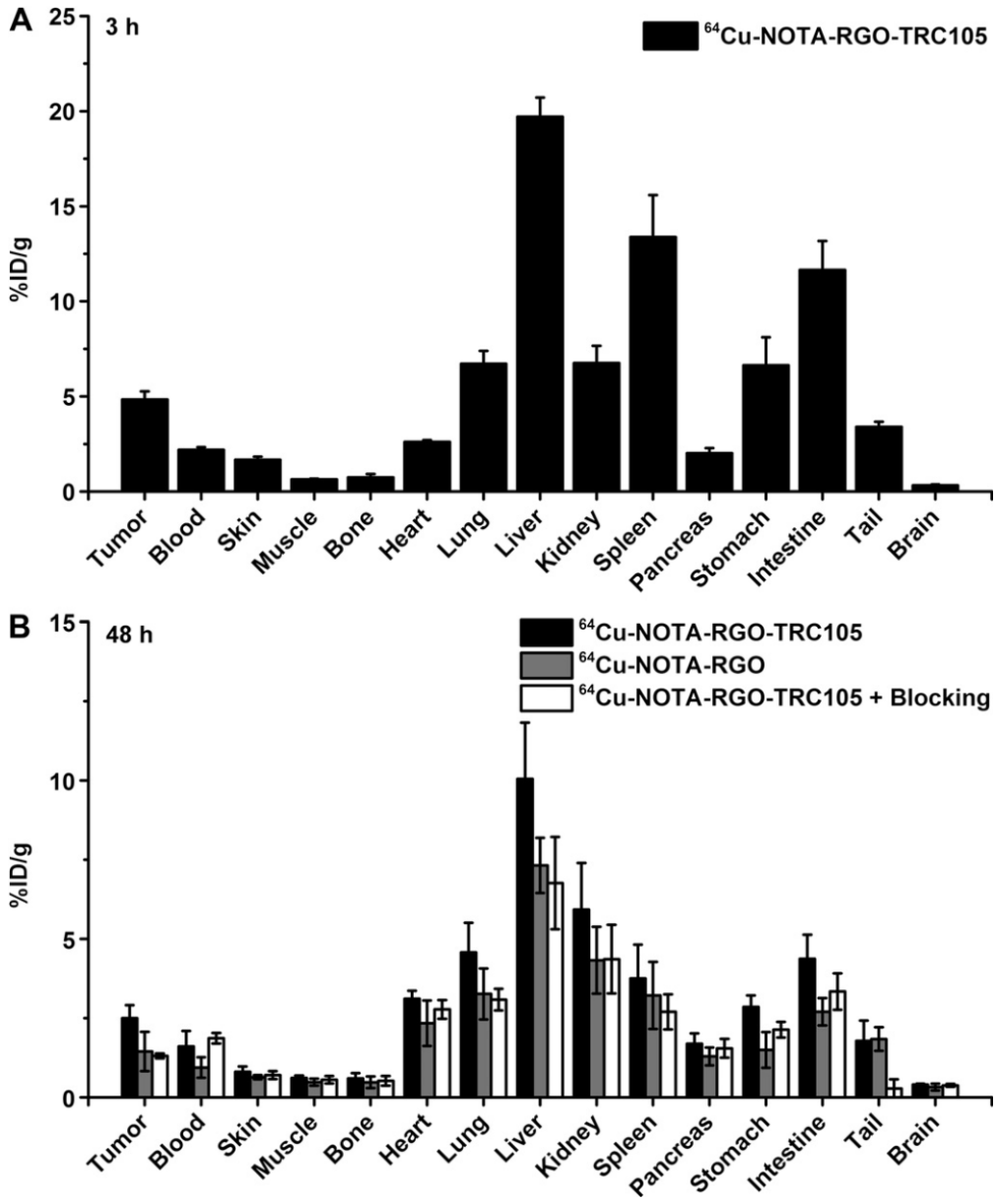

Figure 2.5. Biodistribution studies in 4T1 tumor-bearing mice at 3 h (**A**) and 48 h (**B**) post-injection of the RGO conjugates. All data represent 4 mice per group.

2.3.4. Histology

Histological studies were carried out to confirm that ^{64}Cu-NOTA-RGO-TRC105 was successfully delivered to the tumor vasculature via CD105 targeting, which serves as a critical

cross-validation of the in vivo results since PET only measures the distribution of ^{64}Cu but not the RGO conjugate per se. As indicated in Figure 2.6, NOTA-RGO-TRC105 distribution in the 4T1 tumor was primary on the vasculature (indicated by excellent overlay of the red and green fluorescence signal, which represents CD31 and NOTA-RGO-TRC105, respectively).

Due to the relatively large size of NOTA-RGO-TRC105, little extravasation (i.e., green spots in the merged image) was observed in the 4T1 tumor which confirmed that tumor vasculature targeting is a valid and suitable approach for RGO. On the other hand, the green fluorescence (attributed to NOTA-RGO-TRC105) in the liver and spleen was mostly outside the vasculature (red fluorescence for CD31 staining), suggesting that NOTA-RGO-TRC105 was captured by liver and spleen through non-specific RES uptake instead of CD105 targeting. Little green fluorescence was observed in the muscle, which is consistent with the results of PET and biodistribution studies.

2.4. Discussion

The results from this work are significant in several aspects. First, active tumor targeting in living subjects with RGO has not been reported to date, although in vitro tumor cell targeting has been investigated [51]. The improved tumor uptake of ^{64}Cu-NOTA-RGO-TRC105 via tumor vascular CD105 targeting could be utilized for tumor-targeted drug delivery and/or photothermal therapy of cancer, to enhance therapeutic efficacy and enable cancer theranostics. Of note, RGO has more desirable properties for photothermal therapy than GO (which is more hydrophilic and used in our previous studies [33]) because of its strong absorbance in the near-infrared range [33, 34, 51]. Second, PET has been widely used in clinical oncology for cancer staging and

monitoring the therapeutic response [43, 45, 52, 53]. The wide availability of dedicated small animal PET scanners and clinical PET scanners can enable non-invasive imaging and quantitation of the uptake of RGO conjugates in small animal tumor models and facilitate clinical translation.

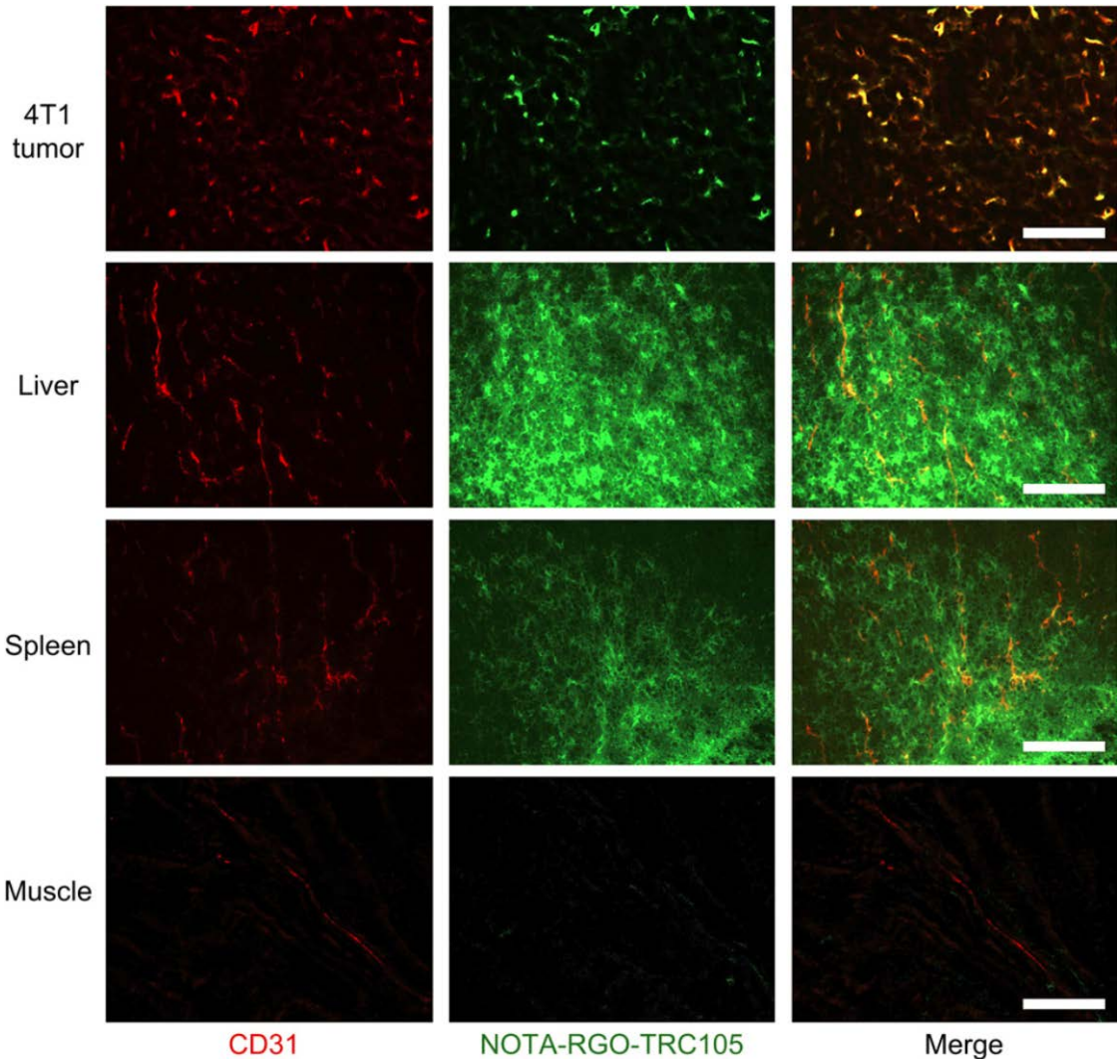

Figure 2.6. Immunofluorescence staining of various tissue slices for CD31 (red, with anti-mouse CD31 primary antibody) and CD105 (green, using TRC105 within NOTA-RGO-TRC105 as the primary antibody). Merged images are also shown. Magnification: 200×. Scale bar: 50 μm.

Third, robust chemistry for RGO functionalization is of utmost importance to future biomedical applications. In vivo stability of the radiolabel is critical for imaging applications. In this regard, the stability of NOTA as a chelator for ^{64}Cu has been well documented in the literature [54, 55]. In addition, the excellent stability for surface conjugation of carbon-based nanomaterials via hydrophobic interactions (e.g., with C_{18} chains) has been well documented in multiple previous reports [33, 34, 47, 51, 56], and was confirmed in our serum stability studies (Figure 2.2B) and corroborated by ex vivo histology (Figure 2.6).

For in vivo tumor targeting using nanomaterials such as RGO, vasculature targeting is a promising approach since many nanomaterials extravasate poorly [57-60]. CD105 is a receptor primarily expressed on tumor neovasculature, independent of its expression on tumor cells [38, 40, 41], and thus can serve as a universal target for multiple solid tumor types. 4T1 breast cancer is a highly vascularized tumor model that grows rapidly upon implantation and provides a sufficient number of vessels for in vivo imaging of angiogenesis (microvessel density of the 4T1 tumor was 205 ± 29 vessels/mm^2 based on CD105 histology; n = 8), while the 4T1 cells themselves do not express significant level of CD105 [33, 48]. Since the 4T1 tumor uptake of ^{64}Cu-NOTA-RGO-TRC105 peaked at 3-6 h p.i., the use of shorter lived PET isotopes (e.g., ^{61}Cu which has a decay half-life of 3.3 h) [29] may also suffice in future studies. Research using graphene-based nanomaterials (especially in their biomedical applications) is still at a nascent stage due to the short time span since the initial report in 2004 [20]. This study serves as an important proof-of-principle for the use of RGO for in vivo tumor vasculature targeting.

2.5. Conclusion

Herein we successfully achieved in vivo tumor vasculature targeting of RGO in a breast cancer model, with ^{64}Cu as the PET label and TRC105 as the targeting ligand. CD105 (the target of TRC105) is specifically and densely expressed on proliferating tumor endothelial cells of many solid tumor types, making it suitable for nanomaterial-based tumor targeting. The RGO conjugates exhibited excellent stability and high specificity for CD105, based on various in vivo/in vitro/ex vivo studies. Serial PET imaging revealed rapid tumor uptake of ^{64}Cu-NOTA-RGO-TRC105, which peaked at 3 h p.i. and remained stable over time. Importantly, ^{64}Cu-NOTA-RGO-TRC105 exhibited little extravasation in the 4T1 tumor, indicating that tumor vasculature (instead of tumor cell) targeting is a valid and preferred approach for nanomaterials.

Chapter 3 VEGFR Targeting Leads to Significantly Enhanced Tumor Uptake of Nanographene Oxide

3.1 Background

Similar to RGO, another subtype of graphene-based nanomaterials, GO, was also widely studied as an excellent platform for applications in biosensor, drug delivery, gene transfection and photothermal therapy due to its unique mechanical, electronic, optical, and chemical properties [40, 47, 61-64]. However, challenges still exist. Most of current studies are focusing on in vivo passive targeted delivery of GO nanoconjugates with only limited tumor accumulation [65, 66]. Developing suitable in vivo active targeting strategies for improving their targeting efficacy is still one of the major challenges in this field.

Although CD105 has been firstly demonstrated as an excellent tumor vasculature targeting ligand [67], further studies are necessary to investigating new targeting ligands for in vivo tumor targeting and imaging with graphene-based nanomaterials. VEGFR is a universal target overexpressed on vasculature of multiple solid tumor types and other disease models [68-70]. Being the naturally existing VEGFR ligand, $VEGF_{121}$ offers several advantages over the synthetic small-molecule VEGFR ligands or anti-VEGFR antibodies, and has much higher binding affinity to VEGFR (nanomolar range) than reported peptidic VEGFR inhibitors (submicromolar to micromolar range) [71]. Therefore, $VEGF_{121}$ could serve as a promising targeting ligand for cancer diagnosis and treatment in preclinical studies and clinical trials. Via VEGFR targeting, we aim for design and synthesis of a new type of GO-based tumor vasculature targeting nanoconjugate by surface engineering of GO with positron emission radioisotopes and

$VEGF_{121}$, forming a novel GO nanoconjugate for non-invasive, quantitative and in vivo vasculature targeted tumor imaging.

3.2. Materials and methods

3.2.1. Reagents

$VEGF_{121}$ was provided by GenScript Corp. (Piscataway, NJ). p-SCN-Bn-NOTA was purchased from Macrocyclics, Inc. (Dallas, TX). Chelex 100 resin (50-100 mesh) and FITC were purchased from Sigma-Aldrich (St. Louis, MO). SCM-PEG-Mal (molecular weight: 5 kDa; Creative PEGworks, Winston Salem, NC), rat anti-mouse CD31 primary antibody (BD Biosciences, San Diego, CA), AlexaFluor488- or Cy3-labeled secondary antibodies (Jackson Immunoresearch Laboratories, Inc., West Grove, CA), Bevacizumab (Avastin, Genentech, San Francisco, CA) and PD-10 desalting columns (GE Healthcare, Piscataway, NJ) were all acquired from commercial sources. Water and all buffers were of Millipore grade and pre-treated with Chelex 100 resin to ensure that the aqueous solution was free of heavy metal. All other reaction buffers and chemicals were obtained from Thermo Fisher Scientific (Fair Lawn, NJ).

3.2.2. Synthesis of GO-PEG-NH_2

GO-PEG-NH_2 was synthesized by a similar process as detailed in our previous report [33, 72]. Briefly, GO was produced by a modified Hummers method, using flake expandable graphite as the original material. The prepared GO was mixed with 6-arm-polyethylene glycol-amine (10 kDa) at a weight ratio of 1:6 and reacted for ~12 h in the presence of N-(3-dimethylaminopropyl-N'-ethylcarbodiimide) hydrochloride to form GO-PEG-NH_2. Excess PEG in the as-synthesized

GO-PEG-NH_2 solution was removed by centrifuge filtration through 100 kDa MWCO Amicon filters and washed with water for 6 times. AFM and DLS were performed to characterize the GO morphology and size distribution of nanoconjugates [73].

3.2.3. Synthesis of $VEGF_{121}$-SH

$VEGF_{121}$ was incubated with Traut's reagent at a molar ratio of 1:15 at pH 8.0 for 2 h. The resulting $VEGF_{121}$-SH was purified by size exclusion column chromatography with PBS (pre-treated with Chelex 100 resin to prevent oxidation of the thiol) as the mobile phase.

3.2.4. Syntheses of GO-$VEGF_{121}$ nanoconjugates

GO-PEG-NH_2 was first mixed with p-SCN-Bn-NOTA at a molar ratio of 1:10 at pH 9.0, and reacted for 2 h at room temperature. The resulting NOTA-GO was purified by centrifugation with 100 kDa MWCO Amicon filters at 8,000 rpm for 15 min. Subsequently, NOTA-GO was reacted with SCM-PEG-Mal at a molar ratio of 1:30 at pH 8.5 for 2 h. The resulting NOTA-GO-PEG-Mal was purified by centrifugation with 100 kDa MWCO Amicon filters at 8,000 rpm for 15min. Afterwards, NOTA-GO-PEG-Mal was reacted with $VEGF_{121}$-SH at a molar of 1:10 at pH 7.5 in the presence of TCEP. The final products were purified by size exclusion column chromatography and termed as NOTA-GO-$VEGF_{121}$. Similar strategies were used for the synthesis of FITC-GO-$VEGF_{121}$ and FITC-GO nanoconjugates.

3.2.5. Cell lines and animal model

4T1 murine breast cancer, U87MG human glioblastoma, and HUVECs were obtained from the American Type Culture Collection (ATCC, Manassas, VA) and cultured as previously described [33]. Cells were used for in vitro and in vivo experiments when they reached ~80 % confluence. All animal studies were conducted under a protocol approved by the University of Wisconsin Institutional Animal Care and Use Committee. Four- to five-week-old female nude mice (Harlan, Indianapolis, IN) were each injected with 2×10^6 U87MG cells in the flank to generate the U87MG glioblastoma model. The mice were used for in vivo experiments when the tumor diameter reached 4-6 mm.

3.2.6. Flow cytometry

HUVECs (VEGFR positive) [74] and 4T1 (VEGFR negative) [75] cells were harvested and suspended in cold PBS with 2 % bovine serum albumin at a concentration of 5×10^6 cells/mL. Cells were incubated with FITC-GO-$VEGF_{121}$ or FITC-GO at a concentration of 5 μg/mL (based on GO) for 30 min at room temperature before washing for three times with cold PBS. Subsequently, the cells were analyzed using a BD FACSCalibur 4-color analysis cytometer equipped with 488 nm and 633 nm lasers (Becton-Dickinson, San Jose, CA) and FlowJo analysis software (Tree Star, Inc., Ashland, OR).

3.2.7. ^{64}Cu labeling

^{64}Cu was produced with an onsite cyclotron (GE PETrace) in University of Wisconsin - Madison. $^{64}CuCl_2$ (74 MBq) was diluted in 300 μL of 0.1 M sodium acetate buffer (pH 6.5) and mixed with 50 μg of NOTA-GO-$VEGF_{121}$ or NOTA-GO. The reaction was conducted at 37 ºC for 30

min with constant shaking [67, 76]. The resulting ^{64}Cu-NOTA-GO-VEGF$_{121}$ or ^{64}Cu-NOTA-GO was purified by size exclusion column chromatography using PBS as the mobile phase. The radioactive fractions containing ^{64}Cu-NOTA-GO-VEGF$_{121}$ or ^{64}Cu-NOTA-GO were collected for further in vitro and in vivo studies. Since all the GO nanoconjugates will contain the same NOTA and PEG chains, both "NOTA" and "PEG" were omitted from the acronyms of the final nanoconjugates for clarity.

3.2.8. Serum stability study

Serum stability study was carried out to ensure ^{64}Cu is stable on NOTA-GO-VEGF$_{121}$ for in vivo PET imaging. ^{64}Cu-NOTA-GO-VEGF$_{121}$ was incubated in PBS and complete serum at 37 ºC for up to 48 h. At different time points, portions of the mixture were sampled and filtered through 100 kDa MWCO filters. The radioactivity that remained on the filter was measured after discarding the filtrate. The retained (i.e., intact) ^{64}Cu on NOTA-GO-VEGF$_{121}$ was calculated using the equation (radioactivity on filter/total sampled radioactivity × 100%).

3.2.9. In vivo VEGFR targeted PET imaging and biodistribution studies

U87MG tumor-bearing mice were each intravenously injected with 5-10 MBq of ^{64}Cu-NOTA-GO-VEGF$_{121}$ or ^{64}Cu-NOTA-GO via tail vein. Serial PET scans were performed at various time points p.i. with using a microPET/microCT Inveon rodent model scanner (Siemens Medical Solutions USA, Inc.). Data acquisition, image re-construction, and ROI analysis of the PET data were performed as described previously [33, 67]. Quantitative PET data of the U87MG tumor and major organs was presented as %ID/g. After the last scan at 48 h p.i., biodistribution studies

were carried out to confirm that the %ID/g values based on PET imaging truly represented the radioactivity distribution in mice. Mice were euthanized and U87MG tumor, blood and major organs/tissues were collected and wet-weighed. The radioactivity in the tissue was measured using a γ counter (PerkinElmer) and presented as %ID/g (mean ± SD).

3.2.10. Histology

U87MG tumor-bearing mice were intravenously injected with GO-$VEGF_{121}$ and GO (5 mg/kg of mouse body weight) and euthanized at 3 h p.i. (when U87MG tumor uptake was at the peak based on PET imaging). Organs including U87MG tumor, liver, spleen and muscle were frozen and cryo-sectioned for histological analysis. Frozen tissue slices of 7 μm thickness were fixed with cold acetone and stained for endothelial marker CD31 by using a rat anti-mouse CD31 antibody and a Cy3-labeled donkey anti-rat IgG [7]. To stain $VEGF_{121}$, the same tissue slices were also incubated with Avastin (primary antibody) [77] and then AlexaFluor488-labeled goat anti-human IgG (secondary antibody). All images were acquired by using a Nikon Eclipse Ti microscope.

3.3. Results and discussion

3.3.1. Synthesis and characterization of GO nanoconjugates

GO was produced by Hummers method and modified with six-armed branched PEG as previously reported for enhanced in vivo stability and biocompatibility [61, 72]. The presence of amine groups at the terminal end could facilitate the further covalent conjugation of various functional entities. PEGylated GO (i.e. GO-PEG-NH_2) was then functionalized with NOTA (a

well-known chelator for copper-64 (^{64}Cu, $t_{1/2}$=12.7 h) labeling) and $VEGF_{121}$ as the targeting ligand for in vivo vasculature targeting.

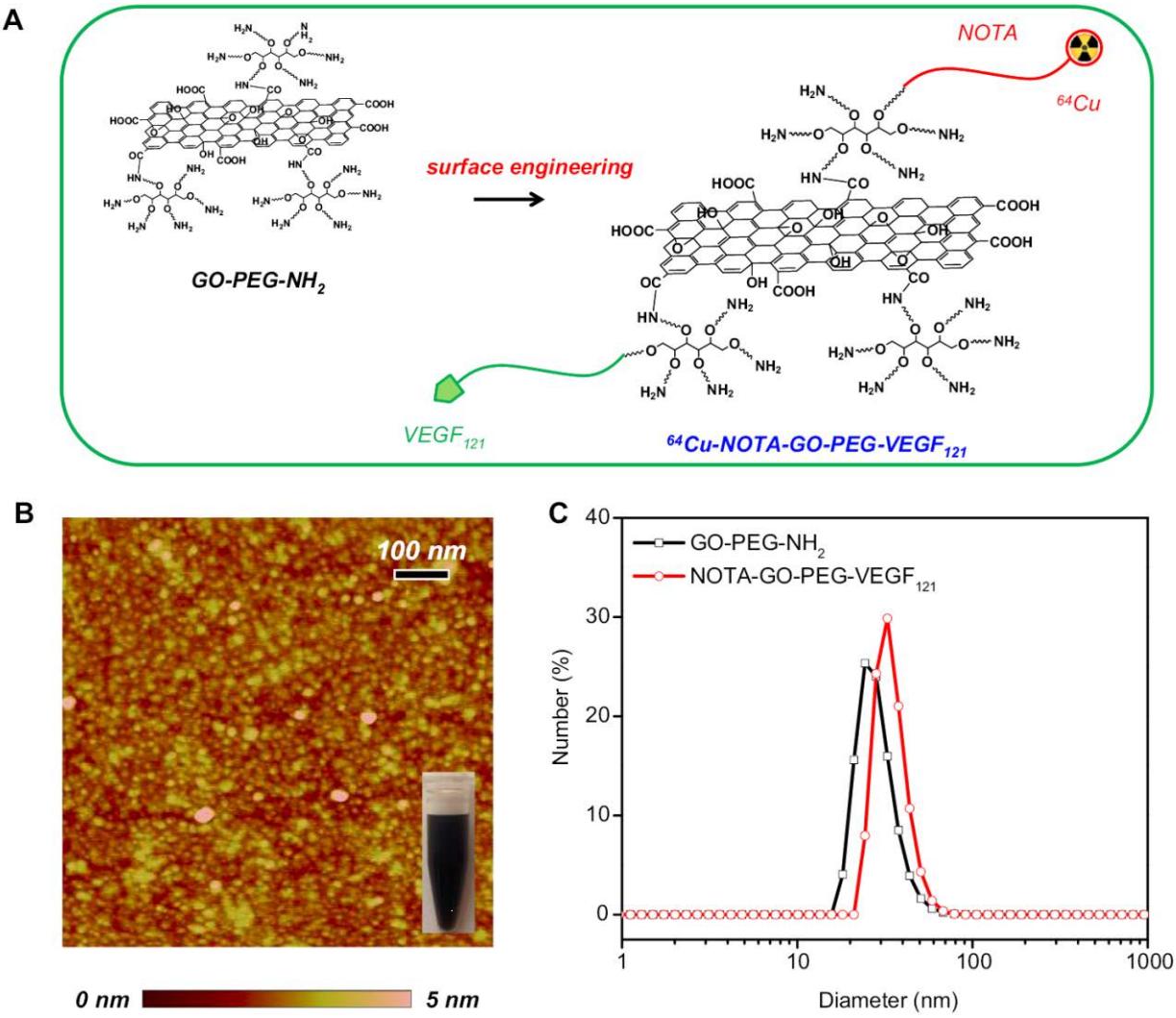

Figure 3.1. (**A**) A schematic illustration showing the surface engineering of GO nanoconjugates. (**B**) AFM image of GO-PEG-NH_2. (**C**) DLS size distribution of the GO-PEG-NH_2 (black line) and NOTA-GO-PEG-$VEGF_{121}$ nanoconjugates (red line).

A schematic structure of final GO nanoconjugate (i.e. ^{64}Cu-NOTA-GO-PEG-$VEGF_{121}$) after surface engineering is shown in Figure 3.1A. As synthesized GO-PEG-NH_2 existed a size range

of 20-50 nm, based on AFM measurements (Figure 3.1B). DLS study showed that GO-PEG-NH_2 has a hydrodynamic diameter of 27.7 ± 5.8 nm, whereas the diameter of NOTA-GO-$VEGF_{121}$ was found to be 32.9 ± 3.0 nm (Figure 3.1C). Since all the GO nanoconjugates will contain the same NOTA and PEG chains, in the following sections both "NOTA" and "PEG" were omitted from the acronyms of the final nanoconjugates for clarity.

3.3.2. In vitro VEGFR targeting

To validate in vitro VEGFR targeting capability of GO-$VEGF_{121}$ nanoconjugates, flow cytometry was carried out in HUVECs (VEGFR positive) [74] and 4T1 murine breast cancer cells (VEGFR negative) [75]. FITC was further conjugated to GO-$VEGF_{121}$ to form FITC-GO-$VEGF_{121}$ (targeted group). FITC-conjugated GO with no $VEGF_{121}$ (i.e. FITC-GO, non-targeted group) was used as the control. As evidenced in Figure 3.2A, the fluorescence signal from HUVECs was significantly enhanced (~20 fold higher than the negative control group) upon incubation with FITC-GO-$VEGF_{121}$, whereas only slight fluorescence enhancement was observed upon FITC-GO treatment. Note, concentration of GO and in vitro incubation time were all kept the same. No significant fluorescence signal enhancement was observed when using 4T1 cell line for both targeted and non-targeted groups. Taken together, flow cytometry results clearly demonstrated high VEGFR targeting specificity and minimal non-specific binding of GO-$VEGF_{121}$ nanoconjugates.

3.3.3. In vivo VEGFR targeting and ex vivo biodistribution studies

Previously, we reported PET imaging of VEGFR expression level using ^{64}Cu-labeled VEGF$_{121}$, and demonstrated higher VEGFR expression in smaller (~60 mm^3) U87MG glioblastoma tumors when compared with larger ones (~1,200 mm^3) [78]. In current study, U87MG tumor-bearing mice with tumor volume of ~60 mm^3 were used for in vivo targeted PET imaging studies.

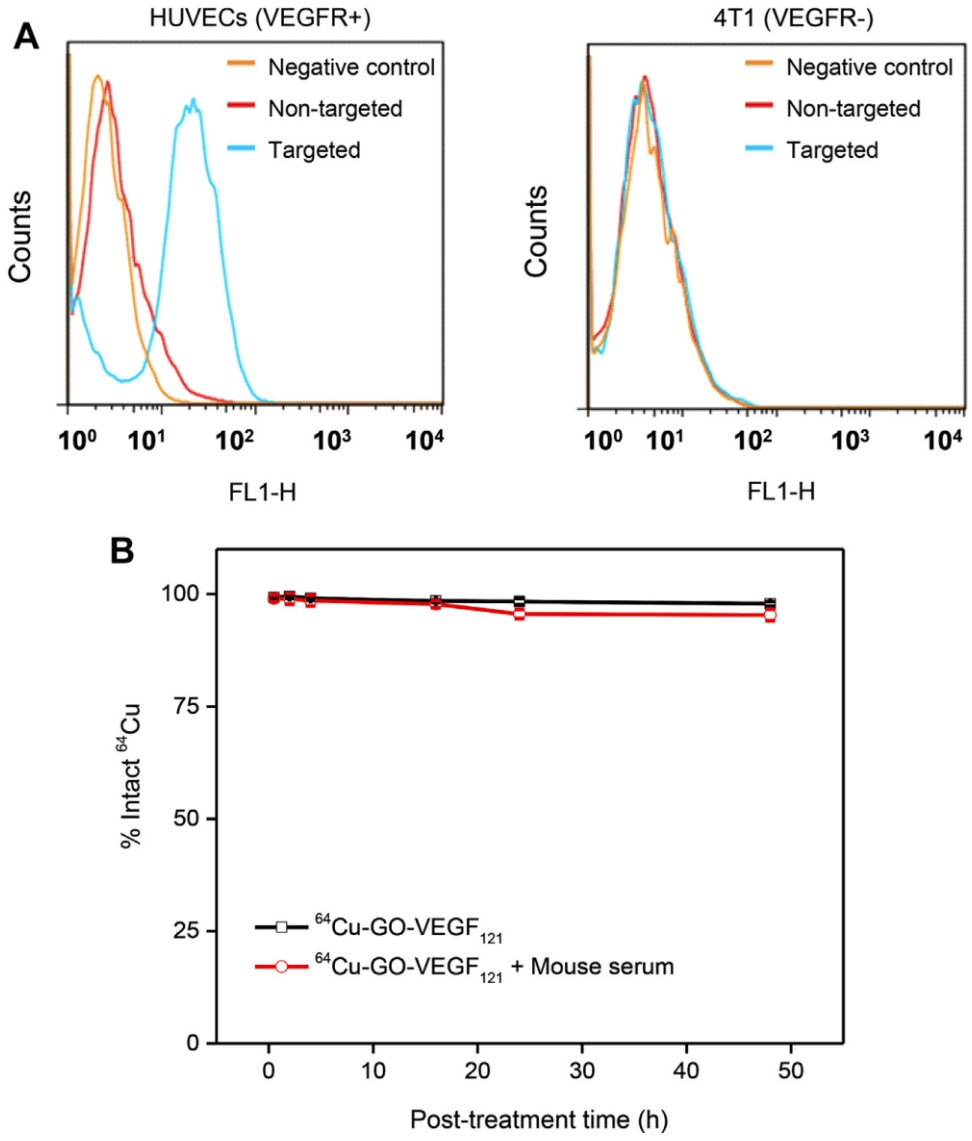

Figure 3.2. In vitro VEGFR targeting and serum stability studies. (**A**) Flow cytometry analysis of the GO nanoconjugates in HUVECs (VEGFR+) and 4T1 breast cancer cells (VEGFR-). (**B**) Serum stability study of ^{64}Cu-GO-VEGF$_{121}$ at 37 ºC for 48 h.

Both GO-$VEGF_{121}$ and GO nanoconjugates were labeled with ^{64}Cu, and purified by PD-10 column, to form ^{64}Cu-GO-$VEGF_{121}$ and ^{64}Cu-GO, respectively. In vitro serum stability was later performed by incubating ^{64}Cu-GO-$VEGF_{121}$ with complete mouse serum at 37 ºC for 48 h (Figure 3.2B). Our results showed that more than 95% of ^{64}Cu remained on the GO-$VEGF_{121}$ nanoconjugates, indicating high stability of ^{64}Cu-GO-$VEGF_{121}$ in mouse serum.

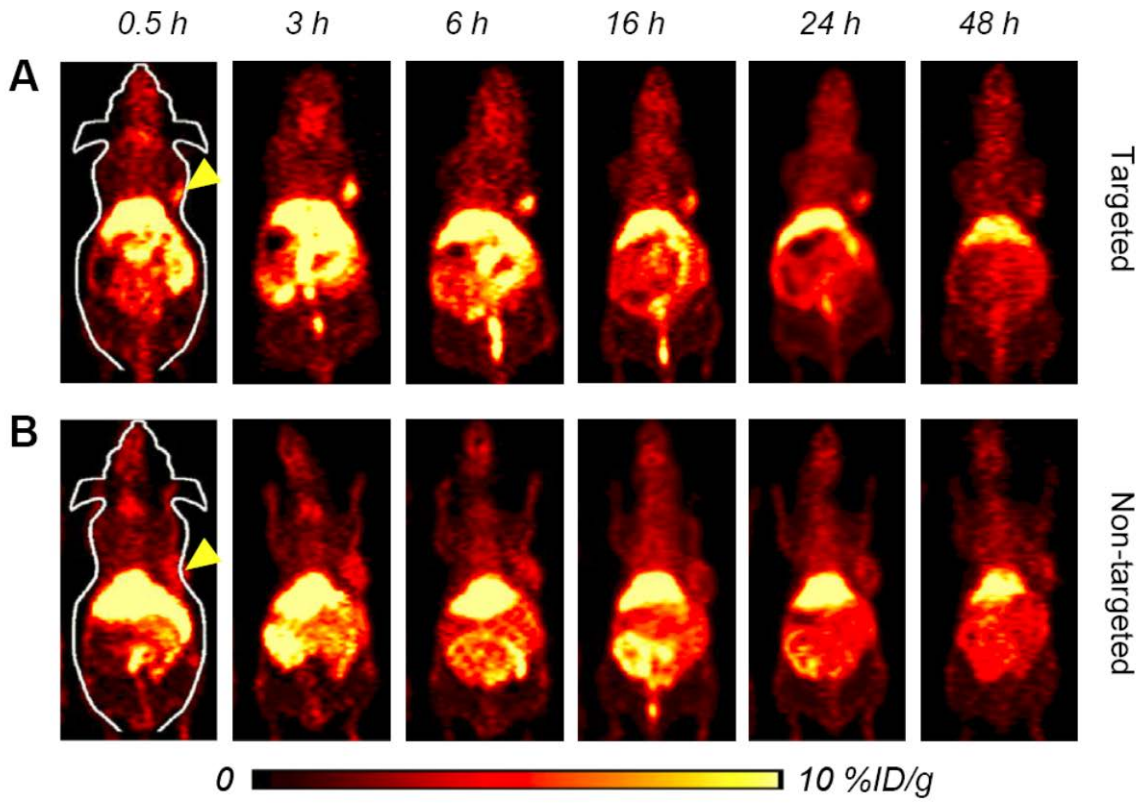

Figure 3.3. In vivo VEGFR targeted PET imaging. Serial coronal PET images of U87MG tumor-bearing mice at different time points post-injection of (**A**) ^{64}Cu-GO-$VEGF_{121}$ (targeted group) and (**B**) ^{64}Cu-GO (non-targeted group). Tumors are indicated by yellow arrowheads.

As prepared ^{64}Cu-GO-VEGF$_{121}$ and ^{64}Cu-GO were later intravenously injected to U87MG tumor-bearing mice and imaged using a microPET/microCT Inveon rodent model scanner at 0.5, 3, 6, 16, 24 and 48 h p.i.. Coronal PET images that contain the U87MG tumors are shown in Figure 3.3, and the quantitative data obtained from region-of-interest (ROI) analysis of the PET data are shown in Figure 3.4**.**

Systematic PET imaging and quantification analysis showed that U87MG tumor uptake of ^{64}Cu-GO-VEGF$_{121}$ (i.e. targeted group) could be clearly visible at 0.5 h p.i. (6.5 ± 1.7 percentage injected dose per gram of tissue [%ID/g]) and peaked at 3 h p.i. with tumor accumulation found to be 8.2 ± 1.4 %ID/g (Figure 3.3A, 3.4A). While, without the conjugation of VEGF$_{121}$, the accumulation of ^{64}Cu-GO was found ~2 fold lower at all time points examined (Figure 3.3B, 3.4B,C), clearly indicating that conjugation of VEGF$_{121}$ to GO could increase tumor uptake through active targeting of VEGFR on the tumor vasculature. Beside higher tumor accumulation, tumor-to-muscle (T/M) ratio was improved as well. The highest T/M ratio in targeted group was found to be 8.4 ± 2.1, which is >2 fold higher than the non-targeted group (Figure 3.4D).

Similar as what we observed in other GO nanoconjugates [33, 49, 67], besides tumor uptake, most of ^{64}Cu-GO-VEGF$_{121}$ was found in liver with the highest uptake estimated to be 24.9 ± 3.0 %ID/g at 0.5 h p.i. and gradually decreased to 10.1 ± 0.5 %ID/g at 48 h p.i. (n=4, Figure 3.3A, 3.4A). Similar high liver uptake was also observed in the non-targeted group (n=4, Figure 3.3B, 3.4B).

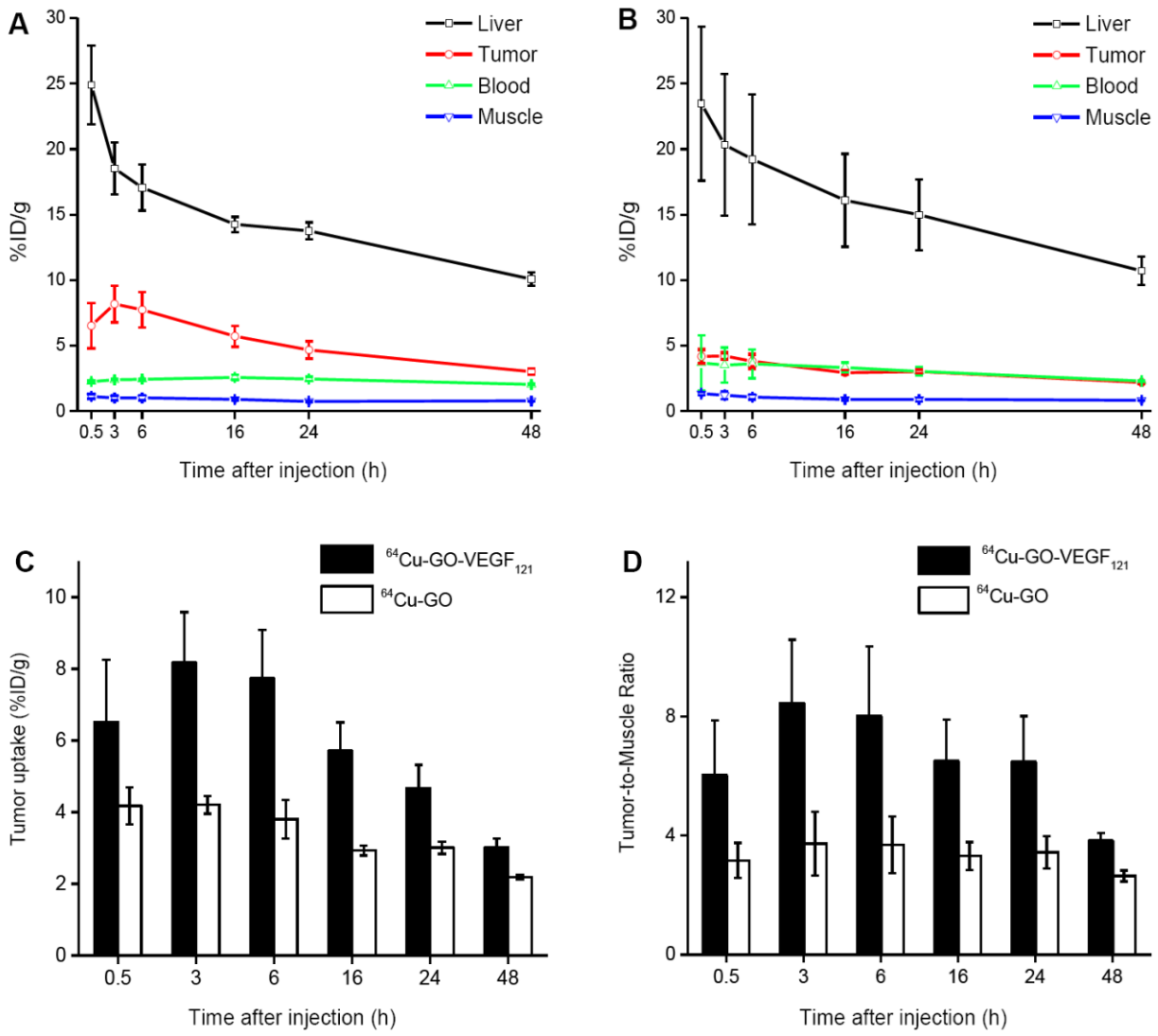

Figure 3.4. Quantitative analysis of the PET data. (**A**) Time□activity curves of the liver, U87MG tumor, blood, and muscle upon intravenous injection of ^{64}Cu-GO-VEGF$_{121}$ (targeted group). (**B**) Time□activity curves of the liver, U87MG tumor, blood, and muscle upon intravenous injection of ^{64}Cu-GO (non-targeted group). (**C**) Comparison of the U87MG tumor uptake in both targeted and non-targeted groups. (**D**) Comparison of the tumor-to-muscle ratio in targeted and non-targeted groups. The differences between the tumor uptake and tumor-to-muscle ratio of ^{64}Cu-GO-VEGF$_{121}$ and ^{64}Cu-GO were statistically significant ($P < 0.05$) at all time points. All data represent 4 mice per group.

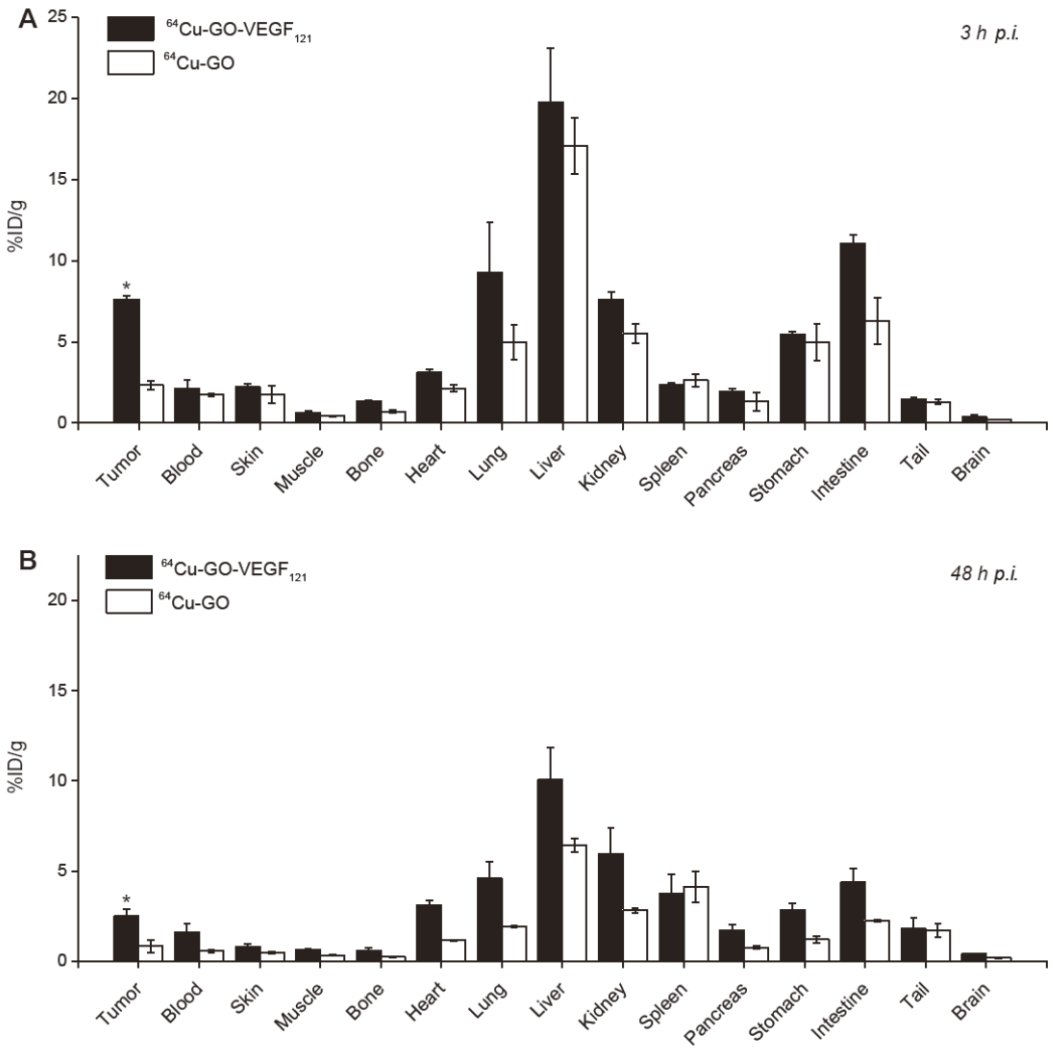

Figure 3.5. Biodistribution studies in U87MG tumor-bearing mice at (**A**) 3 h and (**B**) 48 h post-injection of the GO nanoconjugates. All data represent 4 mice per group

To further confirm the accuracy of PET quantification analysis, ex vivo biodistribution studies were carried out at 3 h p.i. (when tumor uptake peaked based on PET imaging in Figure 3.3A) and 48 h p.i. (after the last PET scan). As shown in Figure 3.5, the quantitative results based on PET and biodistribution studies matched very well, confirming that serial non-invasive PET imaging accurately reflected the distribution of ^{64}Cu-GO-VEGF$_{121}$ and ^{64}Cu-GO in U87MG tumor-bearing mice.

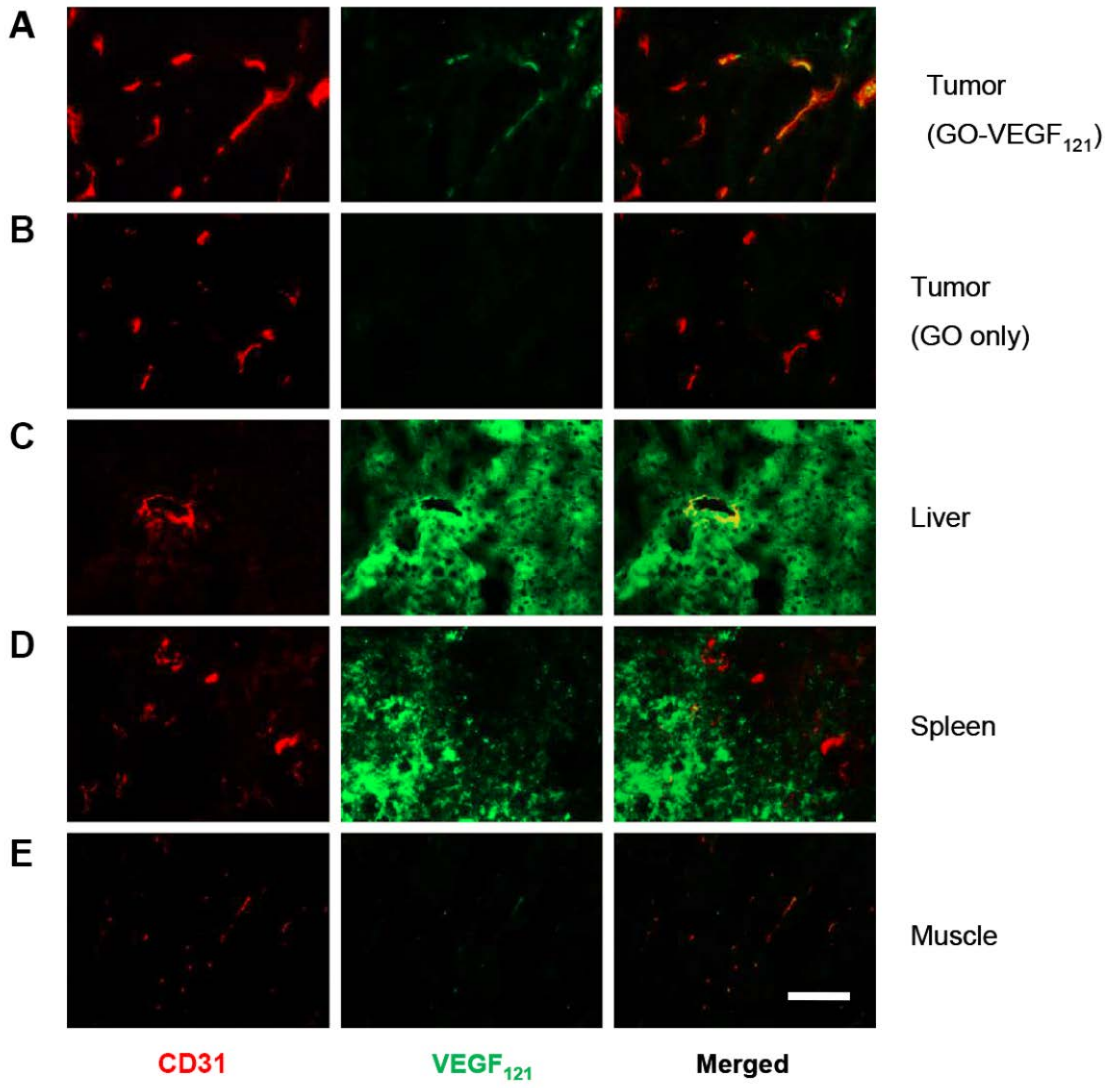

Figure 3.6. Histology study. Immunofluorescence staining of various tissue slices of (**A**) U87MG tumor (targeted group), (**B**) U87MG tumor (non-targeted group), (**C**) Liver, (**D**) Spleen and (**E**) Muscle. Red staining represents CD31 (using anti-mouse CD31 primary antibody), while green staining represents GO-$VEGF_{121}$ (using Avastin as the primary antibody). Scale bar: 100 μm. Note, Slices of liver, spleen and muscle were all from targeted group.

3.3.4. Histology

To further confirm that tumor uptake of ^{64}Cu-GO-VEGF$_{121}$ is VEGFR specific and GO nanoconjugates were indeed delivered to the tumor, histological studies were performed. U87MG tumor-bearing mice were intravenously injected with GO-VEGF$_{121}$ and GO (dose: 5 mg/kg) and euthanized at 3 h p.i. (when U87MG tumor uptake was at the peak based on PET imaging). Organs including U87MG tumor, liver, spleen and muscle were collected, frozen and cryo-sectioned for histological analysis. Well-established protocols were later used for the staining of CD31 and VEGF$_{121}$ [7, 77].

As shown in Figure 3.6A, GO-VEGF$_{121}$ distribution in the U87MG tumor was found primary on the vasculature with little extravasation, as evidenced by the excellent overlay of the CD31 (red) and GO-VEGF$_{121}$ (green), while no obvious green signal could be found in U87MG tumor from the non-targeted group (Figure 3.6B). Strong green fluorescence signal from the liver and spleen slices were observed outside the vasculature, indicating non-specific RES uptake and hepatobiliary clearance of GO-VEGF$_{121}$ (Figure 3.6C,D). In addition, little green fluorescence was observed in the muscle, which is consistent with the results of PET and biodistribution studies (Figure 3.6E). Taken together, our histology study clearly demonstrated the VEGFR targeting specificity of GO-VEGF$_{121}$.

3.4. Conclusion

In conclusion, we performed the surface engineering and in vivo tumor vasculature targeting of GO nanoconjugates in U87MG tumor-bearing mice, with ^{64}Cu as the radiolabel and VEGF$_{121}$ as the targeting ligand. Excellent stability and high targeting specificity of GO-VEGF$_{121}$ were

achieved based on systematic in vivo/in vitro/ex vivo studies. More importantly, our newly developed ^{64}Cu-GO-VEGF$_{121}$ nanoconjugate was able to target vascular VEGFR efficiently in U87MG model with the highest tumor uptake found to be >8 %ID/g, giving an extra boost to tumor uptake based on passive targeting alone (~4 %ID/g). We believe that GO-VEGF$_{121}$ with significantly improved tumor targeting efficiency could inspire future design of smart GO-based nanosystems and show great potential for enhanced theranostics in living systems.

Chapter 4 Chelator-Free Radiolabeling of Graphene: Breaking the Stereotype of Chelation

4.1. Background

The success of positron emission tomography (PET) in early cancer detection has triggered extensive development of molecular radiotracers[3, 43, 79]. Numerous radiolabeled nanomaterials, such as quantum dots (QDs)[57, 80, 81], superparamagnetic iron oxide nanoparticles (SPIONs)[82], graphene[33, 67, 83], gold nanoparticles[84, 85], silica nanoparticles[86] and polymeric nanoparticles[87, 88], have been successfully applied for PET imaging in living systems after conjugation with different kinds of chelators, such as DOTA (1,4,7,10-tetraazacyclododecane-1,4,7,10-tetraacetic acid) and NOTA (1,4,7-Triazacyclononane-1,4,7-triacetic acid). Chelators are especially important in radiolabeling, since they can stably incorporate radiometals and prevent transchelation by intrinsic proteins, making chelator-based radiolabeling of nanomaterials the gold standard for examining their *in vivo* properties[89]. However, chelator-based radiolabeling and PET imaging has its inevitable challenges. The incorporation of chelators might alter the size, surface charge and hydrophilicity of the tracer, which may eventually lead to completely different imaging consequences[90-93]. In addition, due to their macrocyclic structure and relatively hydrophobic nature[94], chelators might nonspecifically attach on the surface of the nanoparticles and leach out after entering the blood circulation, influencing the overall imaging results. Therefore, although chelators have been widely employed in radiometal- assisted PET imaging of nanomaterials in the past decade, it is questionable whether such a practice precisely depicts their real biodistribution.

To better understand the *in vivo* behavior of the nanoparticles and avoid the influence of the chelators, a novel chelator-free radiolabeling approach can be employed, whereby radiometals can directly label onto the nanoparticles through certain surface interactions[15,]. Intrinsically radiolabeled nanoparticles would potentially maintain their native biodistribution and pharmacokinetics, thereby accurately reflecting the real *in vivo* behavior of the nanoparticles [95, 96]. Moreover, the additional surface functional groups can be employed for improving the conjugation efficiency of targeting ligands or drug encapsulation, for enhanced targeting efficiency and therapeutic efficacy[97]. Last but not the least, chelator-free radiolabeling allows for more flexible surface engineering to make the nanoparticle a versatile theranostic platform.

In this study, graphene, one of the most attractive nanomaterials in the research community, has been employed for chelator-free ^{64}Cu-radiolabeling and PET imaging[33, 67, 83]. Among all the radiometals, ^{64}Cu is one of the most promising and well-investigated radiometals, due to its desirable half-life ($t_{1/2}$ = 12.7 h) for *in vivo* disease detection and patient management[98]. Two subtypes of graphene nanomaterials, reduced graphene oxide (RGO) and graphene oxide (GO), were labeled with ^{64}Cu via transition metal-π interaction based on the electron transfer between $^{64}Cu^{2+}$ cation and π bond on the surface of graphene nanosheets[99-101]. This specific interaction has been demonstrated previously by physical simulations and experiments[99-101]. Herein, we have for the first time harnessed the transition metal-pi interactions between graphene and Cu^{2+} cations for chelator-free radiolabeling and subsequent PET imaging with the as-developed ^{64}Cu-graphene radiotracers for in vivo tumor targeting and imaging. Additionally, we compare the labeling and imaging characteristics of intrinsically radiolabeled graphene with that radiolabeled via the conventional NOTA chelator, in order to probe the technique in more detail.

4.2. Materials and methods

4.2.1. Reagents

^{64}Cu was produced by a GE PETtrace cyclotron using the ^{64}Ni(p,n)^{64}Cu reaction. ^{89}Zr was produced by a GE PETrace cyclotron using the ^{89}Y(p,n)^{89}Zr reaction. NOTA was purchased from Macrocyclics, Inc. (Dallas, TX). Chelex 100 resin (50-100 mesh; Sigma-Aldrich, St. Louis, MO), complete mouse serum (Jackson Immuno Research Laboratories, West Grove, PA) and PD-10 desalting columns (GE Healthcare, Piscataway, NJ) were all acquired from commercial sources. Water and all buffers were of Millipore grade and pre-treated with Chelex 100 resin to ensure that the aqueous solution was free of heavy metal. All other chemicals and buffers were obtained from Thermo Fisher Scientific (Fair Lawn, NJ).

4.2.2 Cell lines and animal models

4T1 murine breast cancer cells were obtained from American Type Culture Collection (ATCC, Manassas, VA) and cultured according to the supplier's instructions. When they reached ~80% confluence, the cells were collected for tumor implantation[102]. Four-to-five-week-old female Balb/c mice (Harlan, Indianapolis, IN) were each subcutaneously injected with 2×10^6 4T1 cells in the flank to generate the 4T1 breast cancer model. The mice were used for *in vivo* experiments when the tumor diameter reached 6-8 mm. All animal studies were conducted under a protocol approved by the University of Wisconsin Institutional Animal Care and Use Committee.

4.2.3. Synthesis of RGO-PEG, GO-PEG and derivatives

RGO and GO was produced by a modified Hummers method, using flake expandable graphite as the original material, as detailed in our previous reports[72, 73]. The prepared RGO was mixed with C_{18}PMH-PEG_{5000} at a weight ratio of 1:10 and incubated under sonication for 1.5 h to form RGO-PEG, while the prepared GO was mixed 6-arm PEG (10 kDa) at a weight ratio of 1:6 and reacted for ~12 h in the presence of N-(3-dimethylaminopropyl-N'-ethylcarbodiimide) hydrochloride to form GO-PEG. Excess PEG in the as-synthesized RGO-PEG and GO-PEG solution was removed by centrifugal filtration through 300 kDa MWCO Amicon filters and 100 kDa MWCO Amicon filters and washed with water for 6 times respectively. The resulting RGO-PEG was characterized by atomic-force microscopy and dynamic light scattering. To generate the control nanoconjugates NOTA-PEG-RGO, RGO was firstly modified with C_{18}PMH-PEG_{5000}-NH_2 and then reacted with p-SCN-Bn-NOTA at a molar ratio of 1:10 at pH 9.0 for 2 h at room temperature and purified with PD-10 desalting column to yield NOTA-PEG-RGO.

After synthesis of RGO-PEG, DOX was loaded by incubating with RGO-PEG at a weight ratio of 2:1 for 3 h. The excess DOX was removed with 100 kDa MWCO Amicon filters. As-prepared DOX-loaded RGO-PEG was defined as (DOX)RGO-PEG. In addition, NOTA-loaded RGO-PEG, defined as (NOTA)RGO-PEG, was prepared with similar loading procedures.

4.2.4. Characterization

The size and morphology of graphene nanosheets were measured by AFM (Bruker Biospin Corporation, Billerica, MA). The size distribution was further confirmed by DLS on Nano-Zetasizer (Malvern Instruments Ltd., Worcestershire, UK). Fourier transform infrared (FT-IR)

spectra were obtained in the range of 650–3500 cm^{-1} using a Bruker Equinox 55/S FT-IR/NIR Spectrophotometer.

4.2.5. Radiolabeling and labeling stablility

$^{64}CuCl_2$ (74 MBq) was diluted in 300 μL of 0.1 M sodium acetate buffer (pH 5.5) and mixed with RGO-PEG, GO-PEG and their derivatives. The reactions were conducted at 37 ºC for 60 min with constant shaking. The resulting ^{64}Cu-RGO-PEG, ^{64}Cu-GO-PEG, ^{64}Cu-NOTA-PEG-RGO, (^{64}Cu-NOTA)RGO-PEG and (^{64}Cu-DOX)RGO-PEG were purified by size exclusion column chromatography using PBS as the mobile phase. The labeling yield was measured by thin layer chromatography (TLC) using 0.5 M Ethylenediaminetetraacetic acid (EDTA) as the mobile phase to eliminate unstable adsorption of isotopes. The labeling yields at different reaction times were calculated from autoradiography images of TLC plates. To examine the radiolabeling specificity, ^{89}Zr-oxalate (74 MBq) was mixed with RGO-PEG and GO-PEG in 300 μL of 0.5 M HEPES buffer (pH 7.0) at 37 ºC for 60 min with constant shaking. The labeling yields were tested by TLC plates with the same setting as described above.

To test the labeling stability, ^{64}Cu-RGO-PEG, ^{64}Cu-GO-PEG and other controls were incubated in both PBS and complete mouse serum at 37 ºC for up to 24 h under constant shaking. Portions of the mixture were sampled at different time points and filtered through 300 kDa MWCO filter. The radioactivity that remained on the filter was measured after discarding the filtrate, and retained (i.e., intact) ^{64}Cu-RGO-PEG, ^{64}Cu-GO-PEG and their derivatives were calculated using the equation (radioactivity on filter/total sampling radioactivity × 100%).

4.2.6. In vivo PET and biodistribution studies

Serial PET scans of ^{64}Cu-RGO-PEG was performed in 4T1 tumor-bearing mice (n = 3) using a microPET/microCT Inveon rodent model scanner (Siemens Medical Solutions USA, Inc.), at different time points (0.5 h, 3 h, 6 h and 24 h) post-injection (p.i.) via tail vein. Data acquisition, image reconstruction, and region-of-interest (ROI) analysis of the PET data were performed as previously described[103]. Quantitative data of ROI analysis on tumor and other organs was presented as percentage injected dose per gram of tissue (%ID/g). As control groups, 4T1 mice injected with ^{64}Cu-NOTA-PEG-RGO and (^{64}Cu-NOTA)RGO-PEG were also scanned (n = 3).After the last scan at 24 h p.i., mice were sacrificed under anaesthesia for ex vivo biodistribution studies. Tumor, blood and major organs/tissues were collected and weighted. The radioactivity in the tissue was measured using a γ counter (PerkinElmer) and presented as %ID/g (mean ± SD).

4.2.7. Photoacoustic Imaging

Photoacoustic imaging was performed on Vevo LAZR Photoacoustic Imaging System (VisualSonics, Inc., Toronto, Canada) with a laser excitation wavelength of 808 nm and a focal depth of 100 mm. 4T1 tumor-bearing mice were intravenously injected with RGO-PEG (200 µL, 0.2 mg/ml) and scanned at 3 h post-injection. The same volumes of PBS were injected in 4T1 tumor-bearing mice as control groups.

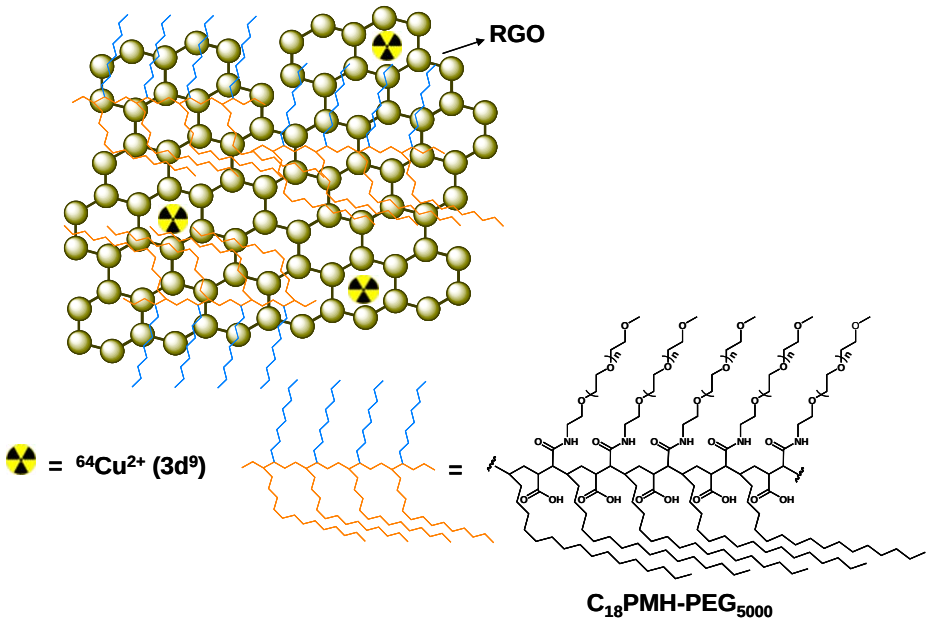

Figure 4.1. Schematic illustration of ^{64}Cu chelator-free labeled graphene nanoparticles.

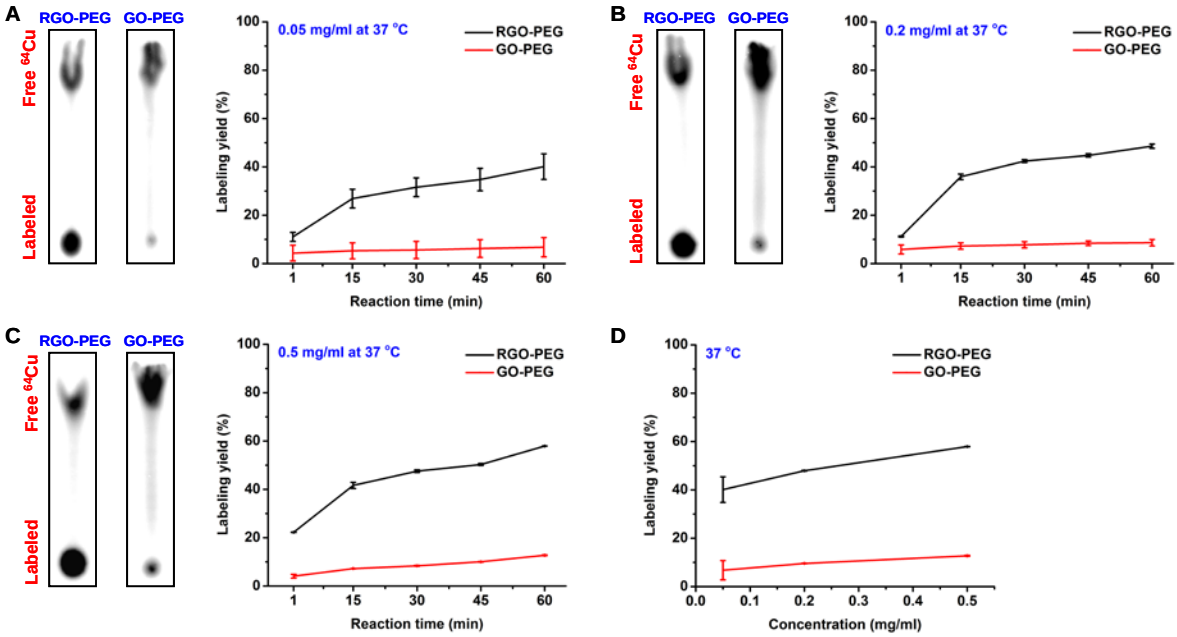

Figure 4.2. Chelator-free labeling of RGO-PEG and GO-PEG at 37 ºC. Autoradiographic images of TLC plates and their labeling yield at different time points were acquired at concentrations of 0.05 mg/ml (**A**), 0.2 mg/ml (**B**) and 0.5 mg/ml (**C**). (**D**) Comparison of the labeling yields of RGO-PEG and GO-PEG at different concentrations after 60 min incubation.

4.3. Results

4.3.1. Chelator-free radiolabeling of RGO and GO

Chelator-free radiolabeling of the nanomaterials was achieved by simply mixing RGO and GO with ^{64}Cu in 0.1 M sodium acetate buffer (Figure 4.1). Theoretically, $^{64}Cu^{2+}$ ions ($3d^9$) need one electron to form a stable electronic configuration; π bonds of graphene are able to provide the additional electron to stably incorporate the $^{64}Cu^{2+}$ acceptor ions onto the surface of graphene[99, 100]. Therefore, the amount of π bonds on the graphene nanomaterials becomes an essential factor influencing the labeling efficiency and radiostability.

To validate our hypothesis regarding the mechanism of chelator-free labeling on graphene, we performed the ^{64}Cu labeling on both PEG modified RGO (RGO-PEG; 22.3 ± 4.5 nm) and GO-PEG at different concentrations and temperatures. Due to more abundant π bonds on RGO-PEG, we expect that RGO-PEG should have significantly higher labeling yield. At 37 ºC, RGO-PEG at an extremely low concentration (0.05 mg/ml) exhibited excellent yields (11.1 ± 1.9 %, 26.9 ± 3.9 %, 31.6 ± 3.9 %, 34.8 ± 4.7 % and 40.1 ± 5.3 % after 1, 15, 30, 45 and 60 min incubation, respectively), high enough for *in vivo* applications (Figure 4.2A and D). However, the labeling yields of GO-PEG were minimal (4.4 ± 3.3 %, 5.3 ± 3.3 %, 5.7 ± 3.6 %, 6.3 ± 3.7 % and 6.8 ± 4.0 % after 1, 15, 30, 45 and 60 min incubation) due to the lack of sufficient π bonds (Figure 4.2A), validating our premise that chelator-free radiolabeling is π-bond dependent. When increasing the concentration of graphene to 0.2 mg/ml, both RGO-PEG and GO-PEG exhibited enhanced labeling yields (48.0 ± 0.2 % with RGO-PEG and 9.6 ± 0.1 % with GO-PEG after 60 min incubation; Figure 4.2B and D), which was further enhanced upon increasing the

concentration of graphene to 0.5 mg/ml (58.0 ± 0.1 % with RGO-PEG and 12.8 ± 0.2 % with GO-PEG after 60 min incubation; Figure 4.2C and D). To understand the influence of temperature, the radiolabeling efficiency was examined at 75 ºC (Figure 4.3). Labeling yields, as high as 75.5 ± 1.7 % were observed for RGO-PEG, after 60 min incubation (Figure 4.3C and D). Such rapid and high radiolabeling yields are comparable to that achieved with NOTA, the most efficient commercially available ^{64}Cu chelator[54, 104], thereby suggesting the promising potential of chelator-free ^{64}Cu radiolabeling of RGO-PEG for *in vivo* PET imaging applications. On the contrary, the labeling yield with GO-PEG was still relatively low (15.5 ± 0.8 % after 60 min incubation; Figure 4.3C and D), even at higher temperatures, further validating our hypothesis. Taken together, the chelator-free labeling of ^{64}Cu was found to be highly dependent on the amount of π bonds, nanoparticle concentrations and temperature, demonstrating the Cu-π interactions as the underlying mechanism of enhanced intrinsic radiolabeling of graphene nanosheets.

The radiolabeling specificity via transition metal-π interactions was subsequently examined by directly mixing $^{89}Zr^{4+}$ ($4p^6$), which does not have π electrons at most outer atomic orbital, with RGO-PEG and GO-PEG at 0.2 mg/ml at 37 ºC. As expected, both RGO-PEG (about 9.0 %, 10.6 %, 11.0 %, 10.8 % and 9.2 % after 1, 15, 30, 45 and 60 min incubation) and GO-PEG (about 12.1 %, 11.4 %, 11.4 %, 12.3 % and 11.1 % after 1, 15, 30, 45 and 60 min incubation) exhibited minimal labeling yields, demonstrating that no transition metal-π interaction happened to $^{89}Zr^{4+}$. To further confirm the mechanism behind the chelator-free radiolabeling of RGO and the role of π bonds, Fourier transform infrared spectroscopy (FTIR) was conducted on both RGO and Cu-RGO. To avoid the inference from PEG, RGO and Cu-RGO nanoparticles for FTIR

examination were not PEGylated. As shown in Figure 4.4, two new peaks were observed at 1350 cm^{-1} and 3000 cm^{-1} from Cu-RGO, which resembled the peak of C-H bonds, representing the newly formed electron interactions between Cu and C. In addition, a red shift was observed for Cu-RGO bond from 1600 cm^{-1} to to 1750 cm^{-1}, indicating that C-C bond is lengthened by incorporation of Cu into the graphene carbon structures.

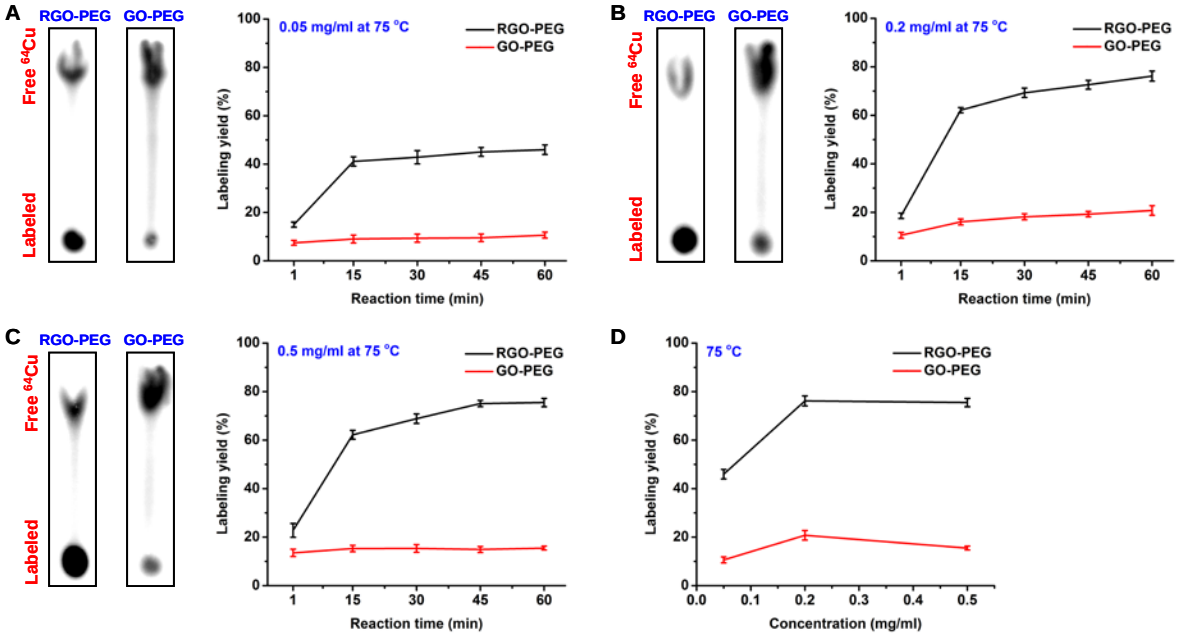

Figure 4.3. Chelator-free labeling of RGO-PEG and GO-PEG at 75 ºC. Autoradiographic images of TLC plates and their labeling yield at different time points were acquired at concentrations of 0.05 mg/ml (**A**), 0.2 mg/ml (**B**) and 0.5 mg/ml (**C**). (**D**) Comparison of the labeling yields of RGO-PEG and GO-PEG at different concentrations after 60 min incubation.

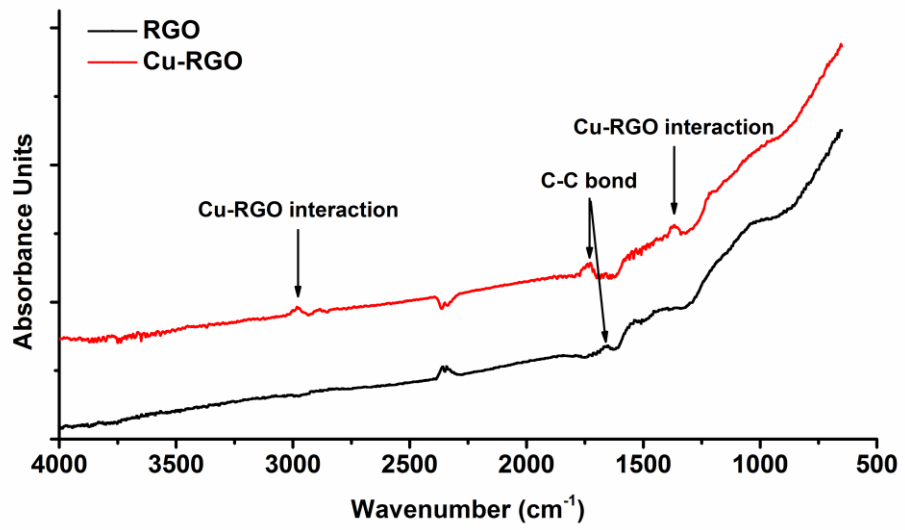

Figure 4.4. FTIR spectra of RGO and Cu chelator-free labeled RGO.

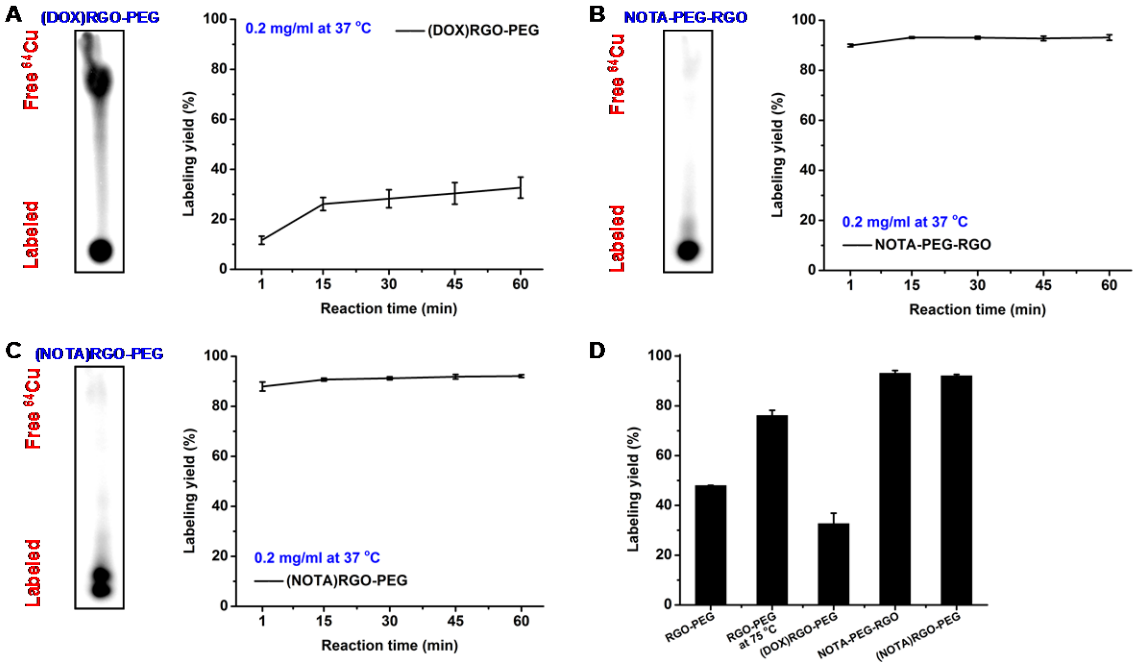

Figure 4.5. Autoradiographic images of TLC plates and their labeling yield at different time points were acquired after incubation ^{64}Cu with DOX-loaded RGO-PEG (**A**), NOTA-conjugated RGO-PEG (**B**) and NOTA-loaded RGO-PEG (**C**) at concentrations of 0.2 mg/ml at 37C. (**D**) Comparison of the labeling yields of RGO-PEG, (DOX)RGO-PEG, NOTA-PEG-RGO and (NOTA)RGO-PEG after 60 min incubation.

Since doxorubicin (DOX) is one of the most common chemotherapeutic drugs which have been widely applied in nanoparticle-based theranostics[105-107], the influence of DOX on the labeling efficiency was also tested, owing to its aromatic structure that contains π bonds. After loading DOX onto RGO-PEG nanosheets, at a weight ratio of 2:1 for 24 h, (DOX)RGO-PEG exhibited slightly reduced labeling yield (32.7 ± 4.2 % at 0.2 mg/ml after 60 min incubation; Figure 4.5A and D), possibly due to competition between DOX loading and ^{64}Cu labeling for π bonds on graphene.

Conventional chelator-based radiolabeling was also conducted after NOTA conjugation to RGO via reaction with amino groups on PEG, as a comparison to chelator-free radiolabeling. As expected, excellent labeling yield were achieved at low nanoparticle concentration (93.1 ± 1.1 % at 0.2 mg/ml after 60 min incubation; Figure 4.5B and D). Interestingly we found that NOTA itself could also be loaded onto of the RGO nanosheets (loading efficiency=28.9 %) without the need of covalent linkage, when we accidentally used RGO-PEG without amino groups (unable to react with NOTA). The loading may attributed to the hydrophobic interactions or the interaction between macrocyclic structure of NOTA and π bonds of RGO. Surprisingly NOTA-loaded RGO-PEG (denoted as (NOTA)RGO-PEG) also exhibited excellent labeling yield (92.1 ± 0.6 % at 0.2 mg/ml within 60 min incubation; Figure 4.5C and D), almost similar to that with NOTA-conjugated RGO (NOTA-PEG-RGO). These interesting results indicate that the decade-old gold-standard NOTA conjugated nanoparticles might not be the most accurate approach for PET imaging, since we cannot assure the purity of NOTA-conjugated RGO without any nonspecific loading.

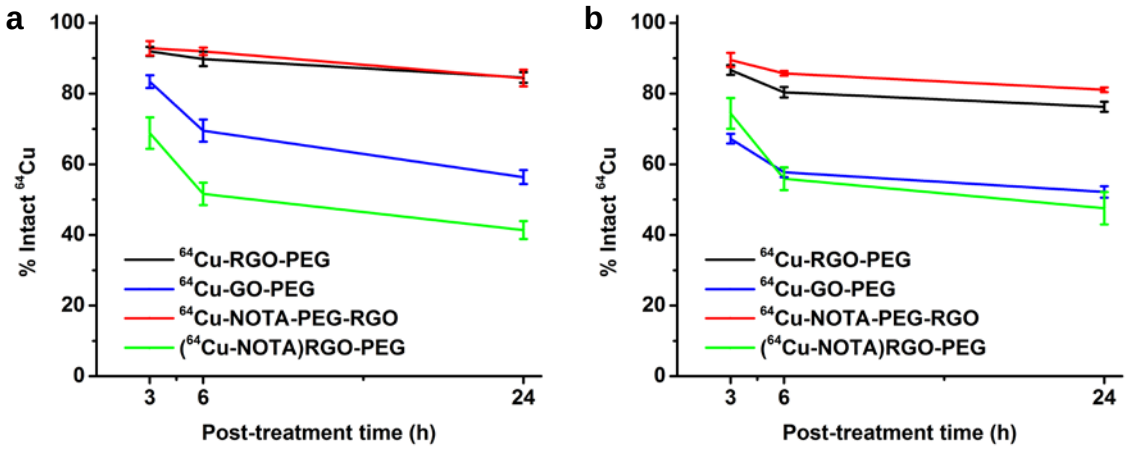

Figure 4.6. Labeling stability of graphene nanoparticles. Labeling stability was observed with ^{64}Cu-RGO-PEG, ^{64}Cu-GO-PEG, ^{64}Cu-NOTA-PEG-RGO and (^{64}Cu-NOTA)RGO-PEG in both PBS (**A**) and complete mouse serum (**B**) during 24 h incubation (n = 3).

4.3.2. Labeling stability of ^{64}Cu-labeled RGO

In vitro labeling stability is an important parameter to test the suitability of radiolabeled nanoparticles for further in vivo applications, since PET imaging can only detect the signal from the isotopes regardless the real biodistribution of the nanoparticles[33]. After incubation in PBS for 24 h, both chelator-free labeled and chelator-based labeled RGO showed excellent *in vitro* stability (84.6 ± 1.5 % with ^{64}Cu-RGO-PEG and 84.4 ± 2.4 % with ^{64}Cu-NOTA-PEG-RGO at 0.2 mg/ml; Figure 4.6A), however the radiostability of chelator-free labeled GO was relatively low (56.4 ± 2.0 % at 0.2 mg/ml after 24 h incubation; Figure 4.6A), indicating that the amount of π bonds affects not only the labeling efficiency but also the stability of the incorporated isotope. In addition, although (^{64}Cu-NOTA)RGO-PEG had excellent labeling efficiency, the labeling stability was relatively low (41.4 ± 2.5 % at 0.2 mg/ml after 24 h incubation; Figure 4.6A),

suggesting that NOTA-loaded RGO-PEG might not be a suitable for *in vivo* applications. The same tests were also performed in complete mouse serum, achieving similar results that ^{64}Cu-RGO-PEG and ^{64}Cu-NOTA-PEG-RGO displayed higher labeling stability compared to both ^{64}Cu-GO-PEG and (^{64}Cu-NOTA)RGO-PEG (Figure 4.6B).

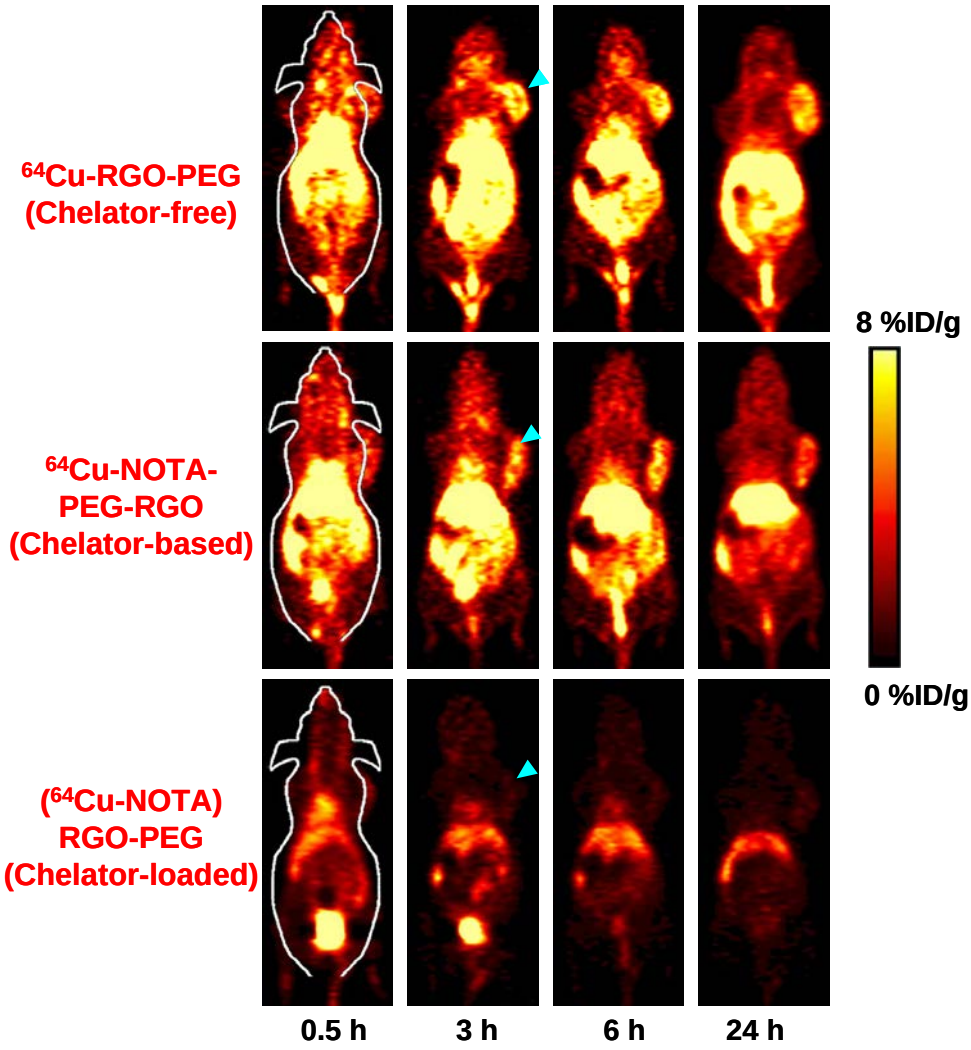

Figure 4.7. In vivo PET imaging. Serial coronal PET images at different time points post-injection of ^{64}Cu-RGO-PEG, ^{64}Cu-NOTA-RGO-PEG and (^{64}Cu-NOTA)RGO-PEG were acquired in 4T1 tumor-bearing mice. Three mice were scanned per group (n = 3).

4.3.3. In vivo PET imaging and photoacoustic imaging

Serial PET imaging was performed with ^{64}Cu-RGO-PEG after tail vein injection in 4T1 tumor-bearing mice. Due to their suitable size and optimized PEGylation, prolonged blood circulation of ^{64}Cu-RGO-PEG was observed (blood uptake: 16.9 ± 2.8, 9.8 ± 0.4, 7.2 ± 0.8 and 4.8 ± 0.9 %ID/g at 0.5, 3, 6 and 24 h p.i.; n = 6; Figure 4.7 and 4.8A), which induced a prompt and persistent tumor uptake (3.8 ± 0.6, 5.7 ± 0.7, 6.6 ± 0.7 and 6.4 ± 0.6 %ID/g at 0.5, 3, 6 and 24 h p.i.; n = 6; Figure 4.7 and 4.8A) via passive targeting (EPR effect). The prolonged blood circulation and superb tumor uptake also demonstrated the excellent *in vivo* radiostability of ^{64}Cu-RGO-PEG with minimal ^{64}Cu detachment. The accuracy of PET imaging was validated by *ex vivo* biodistribution studies (Figure 4.8E), which corroborated well with the region-of-interest (ROI) data from the PET images.

As a control ^{64}Cu-NOTA-PEG-RGO was also tested in the 4T1 tumor-bearing mice. Slightly shorter blood circulation (blood uptake: 13.7 ± 0.7, 7.0 ± 0.3, 5.4 ± 0.1 and 3.2 ± 0.1 %ID/g at 0.5, 3, 6 and 24 h p.i.; n = 3; Figure 4.7 and 4.8B) and lower tumor uptake (3.4 ± 0.5, 4.5 ± 1.0, 4.9 ± 1.8 and 3.9 ± 0.4 %ID/g at 0.5, 3, 6 and 24 h p.i.; n = 3; Figure 4.7, Figure 4.8B and D), suggesting that intrinsically radiolabeled ^{64}Cu-RGO-PEG possesses enhanced *in vivo* radiostability and improved imaging capacity than that of chelator-based ^{64}Cu-NOTA-PEG-RGO. Of note, slight bladder uptake could be observed in mice injected with ^{64}Cu-NOTA-PEG-RGO, stemming from the detachment of ^{64}Cu-NOTA from RGO nanosheets, which may be a mixture of ^{64}Cu-NOTA-PEG-RGO and (^{64}Cu-NOTA)RGO-PEG, since it is impossible to avoid NOTA loading into RGO during chelator conjugation.

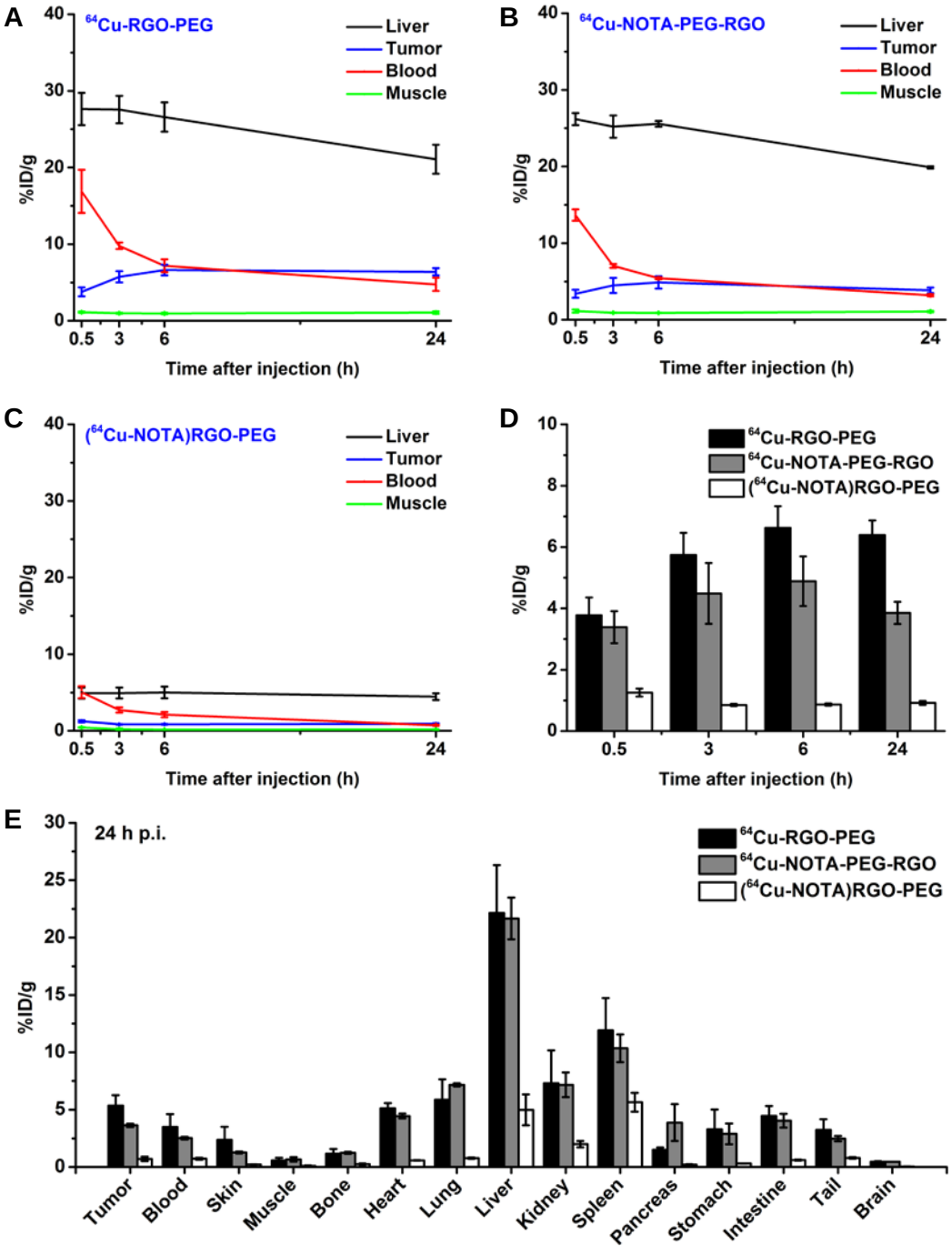

Figure 4.8. Quantitative analysis of the PET data and ex vivo bistribution. Time activity curves of the liver, 4T1 tumor, blood, and muscle upon intravenous injection of ^{64}Cu-RGO-PEG (**A**), ^{64}Cu-NOTA-RGO-PEG (**B**) and (^{64}Cu-NOTA)RGO-PEG (**C**) and comparison of their tumor uptake at different time points (**D**). (**E**) Ex vivo biodistribution of ^{64}Cu-RGO-PEG, ^{64}Cu-NOTA-RGO-PEG and (^{64}Cu-NOTA)RGO-PEG at 24 h p.i..

Accordingly, although (^{64}Cu-NOTA)RGO-PEG had the same labeling efficiency as that of ^{64}Cu-NOTA-PEG-RGO, the *in vivo* stability results were completely different, as evidenced by the PET imaging in mice injected with (^{64}Cu-NOTA)RGO-PEG under similar conditions. The radioactive signal from (^{64}Cu-NOTA)RGO-PEG was strongly depressed (attenuated signal from the heart, as early as 0.5 h post-injection; Figure 4.7) and most activity could only be detected in the bladder by 3 h p.i. (Figure 4.7, 4.8C and D), indicating that ^{64}Cu-NOTA detached from RGO-PEG immediately after entering the blood circulation and was excreted in the urine via renal clearance pathway. Taken together, PET imaging clearly illustrated that intrinsically radiolabeled RGO possesses higher *in vivo* radiostability and hence allows for more reliable evaluation of graphene biodistribution *in vivo.*

Photoacoustic tomography imaging is a rapidly emerging imaging modality relying on ultrasound signals created by light-induced thermoelastic expansion[108-111]. Taking advantage of the strong light absorbance of graphene nanomaterials[112, 113], photoacoustic imaging was performed in RGO-PEG injected mice to further confirm successful tumor retention, and test the multimodality imaging ability of our nanoconstructs. As expected, significantly enhanced signal was observed in tumors injected with RGO-PEG than that from the blank control (Figure 4.9), further corroborating the accuracy of the PET imaging results. Overall, RGO-PEG is a promising multimodality (PET/PA) imaging platform to precisely convey the functional and molecular information in living systems.

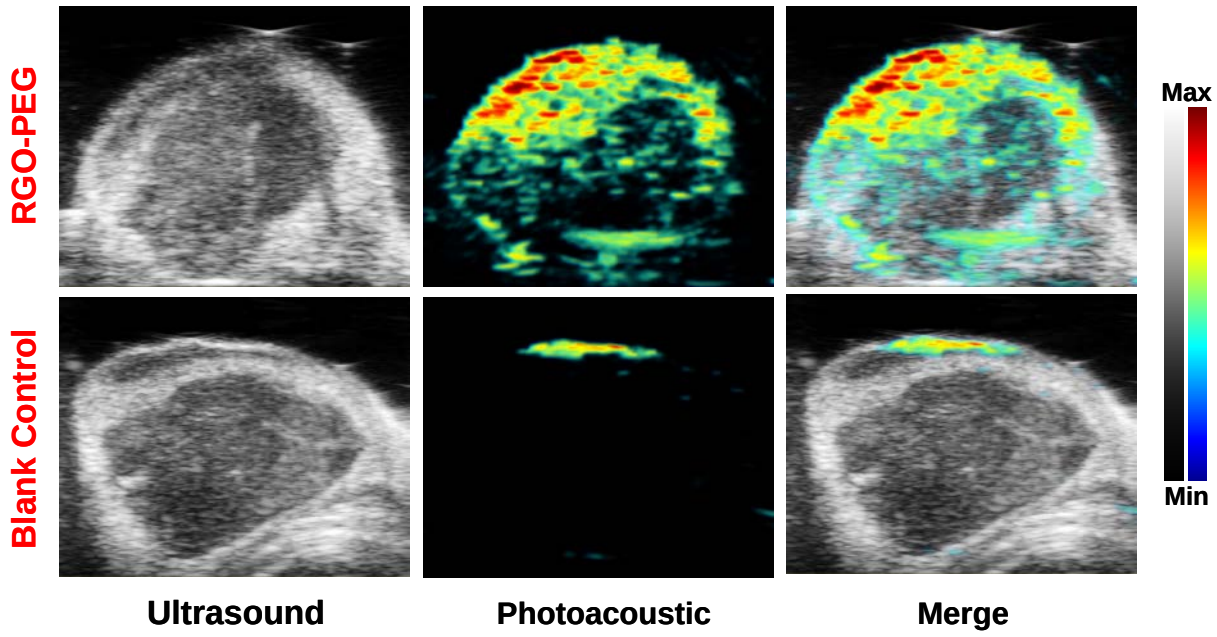

Figure 4.9. Ultrasound and photoacoustic imaging of tumor in the mouse upon intravenous injection of RGO-PEG and the blank control mouse.

4.4. Discussion

NOTA or DOTA conjugation has been routinely employed for small molecule and antibody-based PET imaging, offering sensitive, quantitative and non-invasive functional detection of diseases at cellular or molecular levels[89, 114-116]. In the past decade, with the explosive advances in nano-theranostic research, NOTA/DOTA have been expanded to the realm of nanoparticle-based PET imaging[79, 86, 117], which have assisted in the evaluation of new nanoparticles by better understanding their *in vivo* biodistribution. Unfortunately, owing to the numerous reports of successful nanoparticle-based PET imaging employing NOTA/DOTA aided radiometal chelation, it is now considered as the gold standard in PET-based evaluation of nanoparticle kinetics, without sufficient probe into the efficacy and reliability of the method.

Despite a series of studies having been performed with NOTA-conjugated graphene[33, 67, 83], herein we found that ^{64}Cu can be intrinsically incorporated into graphene nanosheets by direct mixing under the same radiolabeling conditions.. In the present study, the labeling was demonstrated to be based on Cu-π interactions, by which the electrons transfer from donor graphene to acceptor Cu^{2+}. From our rigorous experimentation under different radiolabeling conditions, we found that the labeling yields were highly dependent on sample concentration, labeling temperature, and the amount of π bonds on the nanoplatform. Due to higher order restored graphene structure with more π bonds[113, 118, 119], RGO demonstrated significantly higher labeling yields than those of GO, confirming the accuracy of our hypothesis. More importantly, chelator-free labeled RGO exhibited comparable labeling efficiency and radiostability as the gold-standard NOTA-RGO. NOTA conjugated RGO inevitably includes nonspecific and weak adsorption of NOTA onto the RGO surface, which despite an initially high labeling yield, displays poor *in vivo* radiostabiltiy, resulting in erroneous interpretation of the PET imaging results. Of note, these phenomena may not be limited graphene nanoparticles. Therefore, our study suggested that chelator-free labeling is more suitable for nanoparticle-based PET imaging. NOTA conjugation may become an unnecessary effort which would even negatively influence the accuracy of PET imaging, if chelator-free labeling is applicable.

The PET images for nanoparticulate radiotracers can be sometimes misleading, since free ^{64}Cu is also cleared by the liver and intestine and may accumulate in the tumor[120-122], similar to the biodistribution of ^{64}Cu-labeled nanoparticles, thereby underlining the important and urgent need to develop a highly stable and reliable method of incorporating the isotope into the nanoplatform. The major difference between free and chelated ^{64}Cu is that free ^{64}Cu is promptly cleared from

the blood circulation within several minutes of intravenous injection. Therefore, the signal from the blood at early time points after injection becomes an important criterion for experienced PET scientists to determine the *in vivo* radiostability of ^{64}Cu-labeled nanoparticles. For example, in this study, chelator-free labeled RGO-PEG exhibited excellent blood circulation in mice (Figure 4.8A and B), where the blood uptake was obvious as long as 6 h p.i., suggesting high *in vivo* radiostability. However, if no blood circulation was observed at early time points, even with high tumor uptake, the *in vivo* radiostability of such conjugates would be questionable, which may not be always due to poor PEGylagtion of sample. Furthermore, prominent bladder uptake is closely correlated with ^{64}Cu-labeled small molecule (for example, ^{64}Cu-NOTA, Figure 4.7) or small nanoparticles (< 5 nm)[50]. The important observations in this study draw our attention to the possible chelator-free labeling and nonspecific loading of chelators on NOTA-conjugated nanoparticles, which results in significantly different biodistribution profile. However, these observations may have till date been wrongly attributed to unknown biological errors or sample inconsistence.

Although chelator-free radiolabeling provides important advantages over conventional chelator-based radiolabeling[95, 97], it still poses certain challenges for real world clinical applications. Many chelator-free radiolabeling techniques require the addition of “hot” precursor during nanoparticle synthesis[63, 123, 124], which is not only cumbersome but also not practical in most clinical settings. Meanwhile many other reported methods require high temperature/harsh conditions for isotope incorporation[125], which cannot be performed with temperature-sensitive nanosystems, such as those functionalized with active targeting agents like antibodies or sensitive chemotherapeutic cargo. However, the novel chelator-free labeling via Cu-π

interactions proposed in this study is extremely simple, which can achieve excellent labeling efficiency and radiostability at 37 ºC and can be performed post nanoparticle synthesis by simply mixing the isotope and nanoparticle together, thereby exhibiting great clinical translation potential. Similar post--synthetic chelator-free radiolabeling of nanoparticles in mild environment is drawing more and more attention from the scientific community and promises to become one of the most exciting research directions of nuclear nanomedicine[95, 126-128].

By investigating the mechanism of chelator-free radiolabeling of graphene, we broke the stereotype that NOTA or DOTA conjugation is a necessary for ^{64}Cu-based *in vivo* PET imaging. Our study provides important guidelines for future research on radiochemistry and *in vivo* applications of nanomaterials: (1) Cu-π interaction is widely applicable to ^{64}Cu labeling with graphene, but not limited to it. Other π-bond-rich nanomaterials, such as carbon nanotubes, can be also used as promising candidates for chelator-free radiolabeling of ^{64}Cu. (2) NOTA or DOTA-conjugated nanoparticles may not always provide the most accurate PET imaging, and any results must be interpreted with caution. (3) Scientists have frequently overlooked the possible nonspecific interactions between the chelators and the nanoparticles, which may significantly influence the PET results. For example, NOTA/DOTA conjugation may not be suitable for very hydrophobic and aromatic nanoparticles. As such, thorough investigation of the chelator-conjugated nanoparticles is warranted, both in terms of their physicochemical properties as well as *in vitro* and *in vivo* radiostability. (4) It is beneficial to try chelator-free labeling before conventional chelator-based labeling, which may uncover a novel labeling mechanism providing better labeling efficiency and stability.

4.5. Conclusion

Herein, we successfully conducted the first example of chelator-free radiolabeling of RGO nanosheets with ^{64}Cu, which exhibited excellent labeling efficiency, superb radiostability and enhanced imaging capacity. Although chelator-free labeled RGO has comparable in vitro radiostability as the conventional NOTA-RGO, the in vivo radiostability of chelator-free labeled RGO is much higher, since nonspecific NOTA absorption is inevitable during NOTA conjugation. Therefore chelator-free radiolabeling becomes especially important for nanoparticle-based PET imaging. By investigating the mechanism of chelator-free radiolabeling of graphene, our study provided important guidance for the future research on radiochemistry and in vivo applications of graphene-based nanomaterials.

Chapter 5 Chelator-Free Labeling of Layered Double Hydroxide Nanoparticles for in Vivo PET Imaging

5.1. Background

LDH nanomaterial has been emerged as a novel delivery agent and attracted tremendous interests in the past decades. As a natural mineral and readily synthesized material, LDH has a hydrotalcite-like structure, consisting of positively charged brucite-like cationic layers, negatively charged interlayer anions, and hydrogen bonded water molecules, with a general composition formula of $[M^{2+}_{1-x}M^{3+}_{x}(OH)^{2}]^{x+}(A^{n-})_{x/n}\cdot mH_2O$, where M^{2+}, M^{3+} and A^{n-} represent divalent metal cation, trivalent metal cation and anion respectively [129, 130]. Due to its unique structure and properties, including rich surface functionality, excellent biocompatibility, wide availability and controllable ion-exchange, LDH exhibits great potential as a delivery agent for biomedical applications [131]. In regard to diagnostic imaging, numerous fluorescent dyes and inorganic nanoparticles have been tethered onto LDH for optical imaging, CT and magnetic MRI [132-138]. However, PET, which offers great sensitivity, superb tissue penetration, accurate quantification capability and excellent translational potential [1, 7, 59], has not been explored with LDH-based nanoparticles.

To perform PET imaging, radiometal (e.g. ^{64}Cu, ^{44}Sc and ^{89}Zr) is a primary category of radioisotopes for radiolabeling. The coordination of certain chelators is usually required for the stable labeling of radionuclides [127, 139]. However, due to the uniqueness of each radionuclide, particular coordination chemistry is necessary for each radionuclide, and hence selecting the best chelator and optimal labeling condition becomes an inevitable challenge [127]. To the contrary,

chelator-free labeling, which eliminates the need of coordination of chelators, has been considered as a promising labeling approach to nanoparticle-based PET imaging [95]. Due to ion-change property, LDH nanoparticles allow the synchronous incorporation of multiple bivalent and trivalent cations (M^{2+} and M^{3+}) into the brucite-like cationic layers [140]. Therefore, we hypothesize that different radionuclides can be incorporated into LDH nanoparticles through chelator-free manner without the use of any chelators, providing a novel nanoplatform for versatile radiolabeling.

Recently, we developed a reliable method to produce Mg_2Al-CO_3-based LDH nanoparticles, which have a well controlled size with 50-300 nm and can be homogeneously dispersed in the aqueous suspension [141, 142]. Because LDH nanoparticles are highly positively charged (zeta potential: 30–50 mV)[142], surface modification could be easily accomplished with negatively charged protein (e.g. BSA) to prevent possible aggregation in physiological buffer or in vivo environment. Therefore, in this study, we propose a chelator-free labeling of BSA-modified Mg_2Al-CO_3-based LDH nanoparticles by simply mixing LDH nanoparticles with a variety of PET isotopes (e.g. ^{64}Cu, ^{44}Sc and ^{89}Zr), followed by the evaluation of the labeling yield and stability to confirm the success of the labeling. In vivo PET imaging was also investigated with radiolabeled LDH nanoparticles for the first time. Rapid and persistent tumor uptake via passive targeting was witnessed.

5.2. Materials and methods

5.2.1. Reagents

Chelex 100 resin (50-100 mesh) was acquired from Sigma-Aldrich (St. Louis, MO). ^{64}Cu was produced by a GE PETrace cyclotron using the ^{64}Ni(p,n)^{64}Cu reaction. ^{44}Sc was produced by a GE PETrace cyclotron using the ^{44}Ca(p,n)^{44}Sc reaction. ^{89}Zr was produced by a GE PETrace cyclotron using the ^{89}Y(p,n)^{89}Zr reaction. Complete mouse serum were acquired from Jackson Immuno Research Laboratories (West Grove, PA). Water and all buffers were of Millipore grade and pretreated with Chelex 100 resin to ensure that the aqueous solution was free of heavy metals. PD-10 desalting columns were acquired from GE Healthcare (Piscataway, NJ). All other reaction buffers and chemicals were from Thermo Fisher Scientific.

5.2.2. Cell lines and animal models

4T1 murine breast cancer cells were obtained from American Type Culture Collection (ATCC, Manassas, VA) and cultured according to the supplier's instructions. When they reached ~80% confluence, the cells were collected for tumor implantation [102]. Four- to five-week-old female BALB/c mice (Harlan, Indianapolis, IN) were each injected with 2×10^6 4T1 cells in the flank to generate the 4T1 breast cancer model. The mice were used for in vivo experiments when the tumor diameter reached 6-8 mm. All animal studies were conducted under a protocol approved by the University of Wisconsin Institutional Animal Care and Use Committee.

5.2.3. Synthesis of LDH

Mg_2Al-CO_3-based LDH nanoparticles were synthesized with a quick precipitation and subsequent hydrothermal treatment as reported previously [129, 141, 142]. In brief, 2.0 mmol of $MgCl_2 \cdot 6H_2O$ and 1.0 mmol of $AlCl_3 \cdot 6H_2O$ were dissolved in 10 mL deionized water, and then

rapidly added to a basic solution (40 mL) containing 6.0 mmol of NaOH and 0.6 mmol of Na_2CO_3 within 5 s. As-prepared solution was then stirred in N_2 stream at room temperature for 10 min. Subsequently, the precipitate was collected after centrifugation, and re-dispersed in 40 mL of deionized water and placed in a 45 mL autoclave with Teflon linen. Lastly, hydrothermal treatment was carried out at 100 ºC in an oven for 16 h to generate the final suspension of $Mg_2Al–CO_3$ LDH nanoparticles.

5.2.4. BSA coating of LDH

0.2 ml of $Mg_2Al–CO_3$ LDH nanoparticles (14.0 mg/mL) were slowly and dropwise added to 0.4 ml BSA solution (50 mg/mL) under vigorous stirring. After stirring for 2 h at room temperature, the mixture solution was then centrifuged (4,000 rpm for 10 min) and washed with PBS for multiple times. As-prepared LDH-BSA suspension contains 4.7 mg/mL of LDH and 33.3 mg/mL of BSA. LDH and LDH-BSA was characterized with TEM and DLS to measure their structure and size.

5.2.5. Radiolabeling and labeling stablility

^{64}Cu, ^{44}Sc, and ^{89}Zr were produced with an onsite cyclotron (GE PETrace). $^{64}CuCl_2$ (74 MBq), $^{44}ScCl_3$ (74 MBq), and ^{89}Zr-oxalate (74 MBq) were diluted in 300 µL of 0.1 M sodium acetate buffer (pH 5.5), 0.5 M sodium acetate buffer (pH 4.5) and 0.5 M HEPES (4-(2-hydroxyethyl)-1-piperazineethanesulfonic acid) buffer (pH 7.0), respectively[33, 102, 143]. The diluted solutions were then mixed with 50 µL of LDH (4.7 mg/mL), LDH-BSA (4.7 mg/mL based on LDH concentration) or only BSA (33.3 mg/ml, the same concentration as that in LDH-BSA) for

chelator-free labeling. The labeling reaction was carried out at 37 ºC for 60 min under constant shaking. The labeling yield was measured by TLC using 0.5 M EDTA as the mobile phase to eliminate unstable adsorption of isotopes. The labeling yield at different reaction time was calculated from autoradiography images of TLC plates. The radioactive fraction was purified with PD-10 size exclusion column chromatography using PBS as the mobile phase.

To test the labeling stability, ^{64}Cu-LDH and ^{64}Cu-LDH-BSA were incubated in both PBS and complete mouse serum at 37 ºC for up to 24 h under constant shaking. Portions of the mixture were sampled at different time points and filtered through 100 kDa MWCO filters. The radioactivity that remained on the filter was measured after discarding the filtrate, and retained (i.e., intact) ^{64}Cu-LDH or ^{64}Cu-LDH-BSA was calculated using the equation (radioactivity on filter/total sampling radioactivity × 100%).

5.2.6. In vivo PET and biodistribution studies

Serial PET scans of ^{64}Cu-LDH-BSA was performed in 4T1 tumor-bearing mice (n = 3) using a microPET/microCT Inveon rodent model scanner (Siemens Medical Solutions USA, Inc.), at different time points (0.5 h, 3 h, 16 h , and 24 h) post-injection (p.i.) of ^{64}Cu-LDH-BSA via tail vein. Data acquisition, image reconstruction, and region-of-interest (ROI) analysis of the PET data were performed as previously described [7, 54, 83]. Quantitative data of ROI analysis on tumor and other organs was presented as percentage injected dose per gram of tissue (%ID/g). To validate the labeling and imaging of ^{64}Cu-LDH-BSA, ^{64}Cu-BSA was also scanned in 4T1 tumor-bearing mice (n = 3) as a control group. After the last scan at 24 h p.i., mice were sacrificed under anaesthesia for biodistribution studies. Tumor, blood and major organs/tissues were

collected and weighted. The radioactivity in the tissue was measured using a γ counter (PerkinElmer) and presented as %ID/g (mean ± SD).

5.3. Results

5.3.1 Synthesis and characterization of LDH nanoparticles

Mg_2Al-CO_3-based LDH nanoparticles were synthesized with a quick precipitation and subsequent hydrothermal treatment as reported previously [129, 141, 142]. As revealed by TEM, LDH nanoparticles are 2-dimentional nanomateirls in layered-sheet shape with the size in the range of 100-150 nm (Figure 5.1B). DLS measurement showed that LDH has an average size of 110 nm (PDI: 0.18) in water and 380 nm (PDI: 0.44) in culture media (Figure 5.1D). The obviously larger size and PDI of LDH in culture media indicate that LDH is not very stable in physiological environment, which restricts the application of LDH in radiolabeling and in vivo PET imaging.

To improve the stability of LDH in vitro/in vivo, negatively charged BSA was coated onto positively charged LDH surface via electrostatic interaction. After BSA coating, as-prepared LDH-BSA maintained stable in PBS for 7 days, whereas LDH without BSA coating precipitated in PBS after same-duration incubation (Figure 1.1C). DLS measurement showed that the average size of LDH-BSA slightly increased to 130 (PDI: 0.21) in water and 150 (PDI: 0.24) in culture media due to the integration of BSA (Figure 1.1D), which indicated that LDH-BSA remained stable in both water and PBS. The final structure of exampled LDH-nanoparticle (^{64}Cu-LDH-BSA) is illustrated in Figure 1.1A.

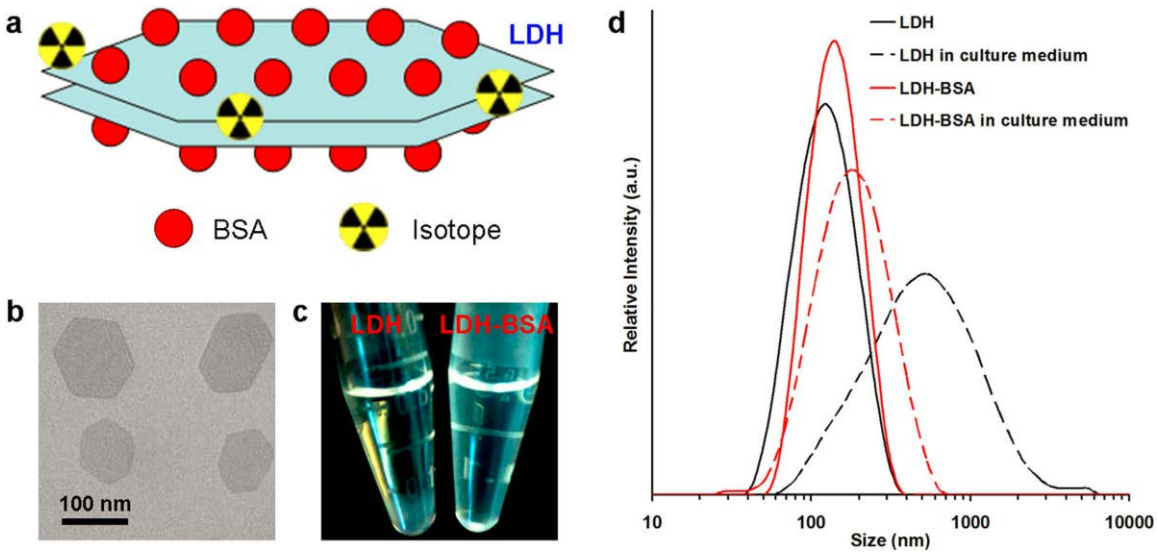

Figure 5.1. Schematic illustration and characterization of LDH nanoparticles. **(A)** A schematic structure of ^{64}Cu-LDH-BSA. **(B)** TEM image of LDH nanoparticles. Scale bar, 100 nm. **(C)** LDH aggregated but LDH-BSA remained stable after incubating LDH and LDH-BSA (4.7 mg/mL) in PBS for 7 days. **(D)** The size distribution of LDH and LDH-BSA in both water and culture media measured by DLS. The size of LDH nanoparticles increased significantly in culture media, whereas the size of LDH-BSA is similar in both water and culture media.

5.3.2 Chelator-free labeling

Different isotopes (^{64}Cu, ^{44}Sc and ^{89}Zr) were directly mixed with LDH-BSA in corresponding buffers (^{64}Cu: 0.1 M sodium acetate, pH 5.5; ^{44}Sc: 0.5 M sodium acetate, pH 4.5; ^{89}Zr: 0.5 M HEPES, pH 7.0) for chelator-free labeling. LDH without BSA coating and only BSA were also labeled to validate that LDH instead of BSA plays a more important role in the labeling. TLC was applied to measure the labeling yield with different isotopes using 0.5 M EDTA as the mobile phase, which can remove the unbounded isotopes and unstable adsorption, ensuring that the resulting labeling yield truly represent the capacity of LDH or BSA for chelator-free labeling.

As a result, $^{64}Cu^{2+}$ and $^{44}Sc^{3+}$ were successfully labeled on LDH and LDH-BSA but not BSA, since LDH allows incorporation of multiple bivalent and trivalent cations [140]. To the contrary, $^{89}Zr^{4+}$ could not be labeled on LDH and LDH-BSA, possibly because it does not fit into the LDH crystal structure (Figure 5.2). In detail, after 60 min incubation with $^{64}Cu^{2+}$, 59.0 % of them were labeled on LDH, and 16.6 % of them were labeled on LDH-BSA (Figure 5.2A and B). There decrease of labeling yield on LDH-BSA is possibly due to existence of BSA, which prevents the interaction of $^{64}Cu^{2+}$ and LDH. In addition, the stable labeling of $^{64}Cu^{2+}$ on BSA was minimal (~1.5 %), indicating that chelator-free labeling of $^{64}Cu^{2+}$ was mainly taken place on LDH rather than BSA. Similar results were also achieved with $^{44}Sc^{3+}$. After 60 min incubation, 41.4 % of them were labeled on LDH-BSA, much higher than those reacting with only BSA (1.7 %; Figure 5.2C and D). The labeling yield of only LDH with $^{44}Sc^{3+}$ was not acquired, due to the aggregation of LDH in highly ionized buffer (0.5 M sodium acetate) without protection of BSA. In comparison, after 60 min incubation with $^{89}Zr^{4+}$, the labeling yields were similarly on all 3 samples (LDH: 9.5 %; LDH-BSA: 12.5 %; BSA 18.4 %; Figure 5.2E and F), indicating that $^{89}Zr^{4+}$ cannot be efficiently labeled onto LDH via chelator-free labeling. Interestingly, it was observed that $^{89}Zr^{4+}$ could be labeled onto BSA, which is possibly due to high affinity of $^{89}Zr^{4+}$ to anionic oxygen donors in BSA [144, 145]. Of note, chelator-free labeling was very quick, as the labeling yield peaked at 15 min and remained stable at the later time points for all 3 isotopes (Figure 5.2B, D and F).

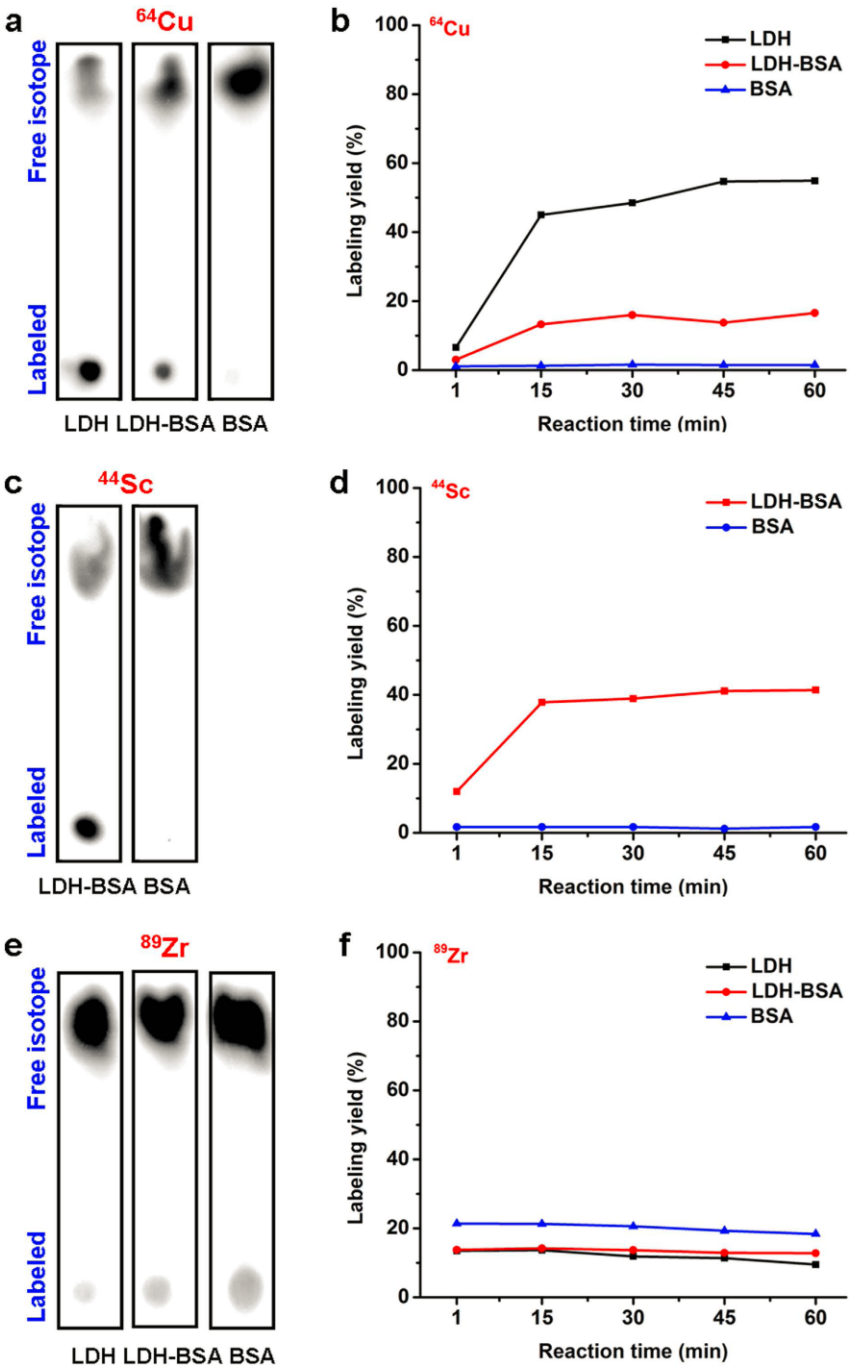

Figure 5.2. Chelator-free labeling of LDH nanoparticles. (**A**), (**C**) and (**E**) Autoradiographic images of TLC plates of LDH, LDH-BSA and BSA after chelator-free labeling with ^{64}Cu, ^{44}Sc and ^{89}Zr for 60 min. (**B**), (**D**) and (**F**) The labeling yield of LDH, LDH-BSA and BSA after chelator-free labeling with ^{64}Cu, ^{44}Sc and ^{89}Zr at different reaction time calculated from autoradiography images of TLC plates.

Labeling stability is a common concern for chelator-free labeling. Besides the usage of EDTA solution during TLC analysis to remove unstable adsorption, the stability of ^{64}Cu-LDH and ^{64}Cu-LDH-BSA was also tested in PBS and complete mouse serum before the potential application in living animals. After incubation with PBS for 24 h, 84.2 ± 11.4 % and 89.3 ± 1.6 % of $^{64}Cu^{2+}$ were still stable on LDH and LDH-BSA respectively (Figure 5.3). While after incubation with complete mouse serum for 24 h, 91.1 ± 3.9 % and 91.6 ± 3.1 % of $^{64}Cu^{2+}$ were stable on LDH and LDH-BSA respectively (Figure 5.3). These results demonstrate that the labeling in chelator-free manner is stable on LDH and LDH-BSA.

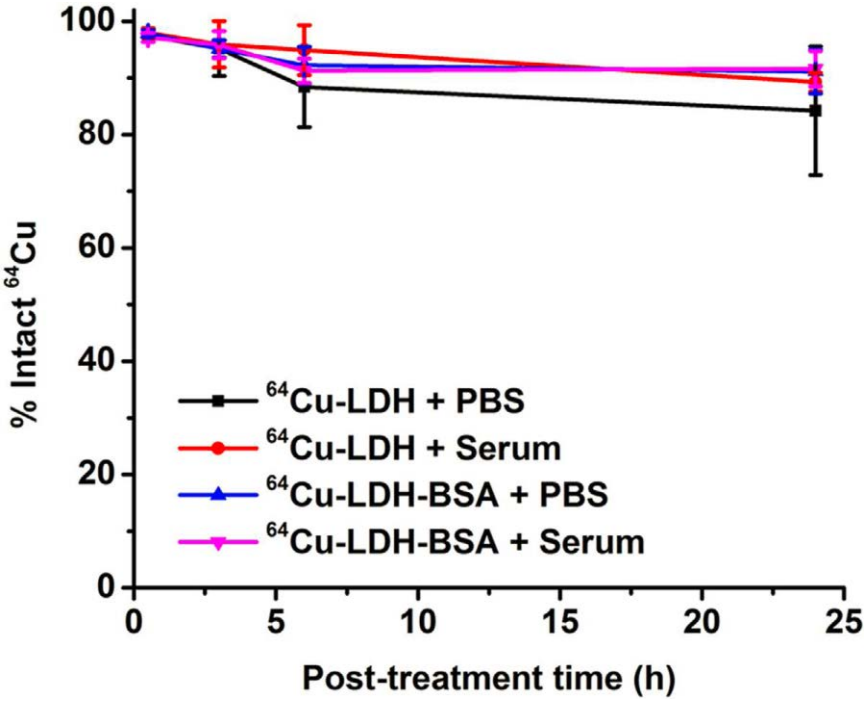

Figure 5.3. Labeling stability of LDH nanoparticles**.** Labeling stability was observed with ^{64}Cu-LDH and ^{64}Cu-LDH-BSA in both PBS and complete mouse serum during 24 h incubation.

5.3.3. In vivo PET and biostribution studies

After purification with PD-10 size exclusion column chromatography, ^{64}Cu-LDH-BSA was intravenously injected into 4T1 tumor-bearing mice to examine their in vivo distribution profile. PET imaging was performed at different time points (0.5 h, 3 h, 16 h and 24 h) post-injection (p.i.) using a microPET/microCT Inveon rodent model scanner. The coronal PET images are shown in Figure 5.4 and quantitative region-of-interest (ROI) analysis is shown in Figure 5.5 A prompt and persistent tumor uptake was achieved via passive targeting (3.5 ± 1.2, 7.2 ± 0.5, 7.7 ± 0.1 and 6.8 ± 0.2 %ID/g, at 0.5 h, 3 h, 16 h and 24 h p.i., respectively; n = 3; Figure 5.5A and C). In contrast, the probe retentions in blood and muscle were much lower at all time points (blood: 2.6 ± 0.2, 3.2 ± 0.1, 3.6 ± 0.1 and 3.6 ± 0.1 %ID/g, and muscle: 0.7 ± 0.1, 0.8 ± 0.1, 0.8 ± 0.1 and 0.8 ± 0.1 %ID/g, at 0.5 h, 3 h, 16 h and 24 h p.i., respectively; n = 3; Figure 5.5A). Tumor/muscle ratios of 4.9 ± 2.0, 8.9 ± 1.1, 9.1 ± 1.4 and 8.6 ± 0.9 were achieved at 0.5 h, 3 h, 16 h and 24 h p.i., respectively (n = 3; Figure 5.5D), suggesting an excellent tumor contrast. Furthermore, the signal in liver peaked at early time point and decreased with time (58.0 ± 7.7, 36.0 ± 6.9, 21.2 ± 1.5 and 21.7 ± 1.7 %ID/g, at 0.5 h, 3 h, 16 h and 24 h p.i., respectively; n = 3; Figure 5.5A), indicating the hepatic clearance of LDH nanoparticles. Taken together, with a prominent tumor uptake and image contrast, ^{64}Cu-LDH-BSA was proven to be a promising nanoplatform for in vivo tumor imaging via passing targeting after chelator-free labeling. With further surface engineering, it could also be applied to active tumor targeting and therapy.

Although the labeling yield of ^{64}Cu-BSA is much lower that that of ^{64}Cu-LDH-BSA, PET imaging was also performed with ^{64}Cu-BSA to compare with the imaging capacity of ^{64}Cu-LDH-BSA. After intravenous injection of ^{64}Cu-BSA into 4T1 tumor-bearing mice, a significantly

lower tumor uptake was acquired (2.9 ± 0.3, 3.4 ± 0.1, 4.1 ± 0.5 and 4.0 ± 0.3 %ID/g, at 0.5 h, 3 h, 16 h and 24 h p.i., respectively; n = 3; Figure 5.4 and Figure 5.5B and C). However, the background signal in muscle was higher (1.9 ± 0.2, 1.5 ± 0.2, 1.1 ± 0.1 and 1.0 ± 0.1 %ID/g, at 0.5 h, 3 h, 16 h and 24 h p.i., respectively; n = 3; Figure 5.5B), possibly due to the smaller size and slower clearance of ^{64}Cu-BSA compared with ^{64}Cu-LDH-BSA, which led to a lower imaging contrast (tumor/muscle ratio:1.5 ± 0.2, 2.2 ± 0.3, 3.6 ± 0.5 and 3.8 ± 0.5, at 0.5 h, 3 h, 16 h and 24 h p.i., respectively; n = 3; Figure 5D). Combining these data, we could draw a preliminary conclusion that the prominent tumor uptake of ^{64}Cu-LDH-BSA was primarily coming from LDH rather than BSA.

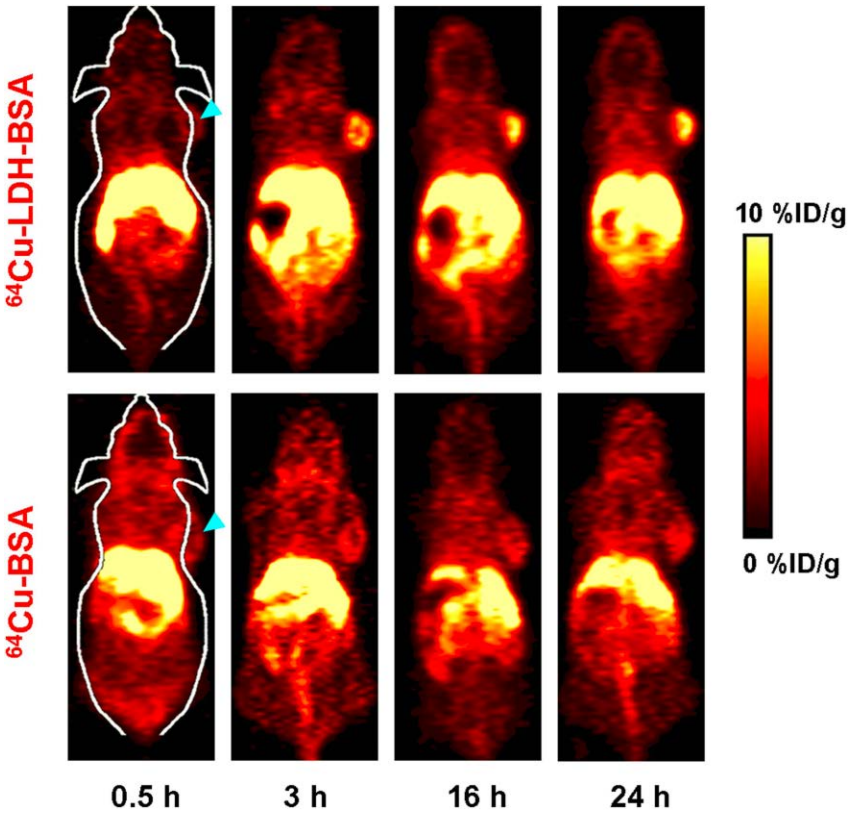

Figure 5.4. In vivo PET imaging**.** Serial coronal PET images at different time points post-injection of ^{64}Cu-LDH-BSA and ^{64}Cu-BSA were acquired in 4T1 tumor-bearing mice. Strong signal in tumor was observed in the mice injected with ^{64}Cu-LDH-BSA.

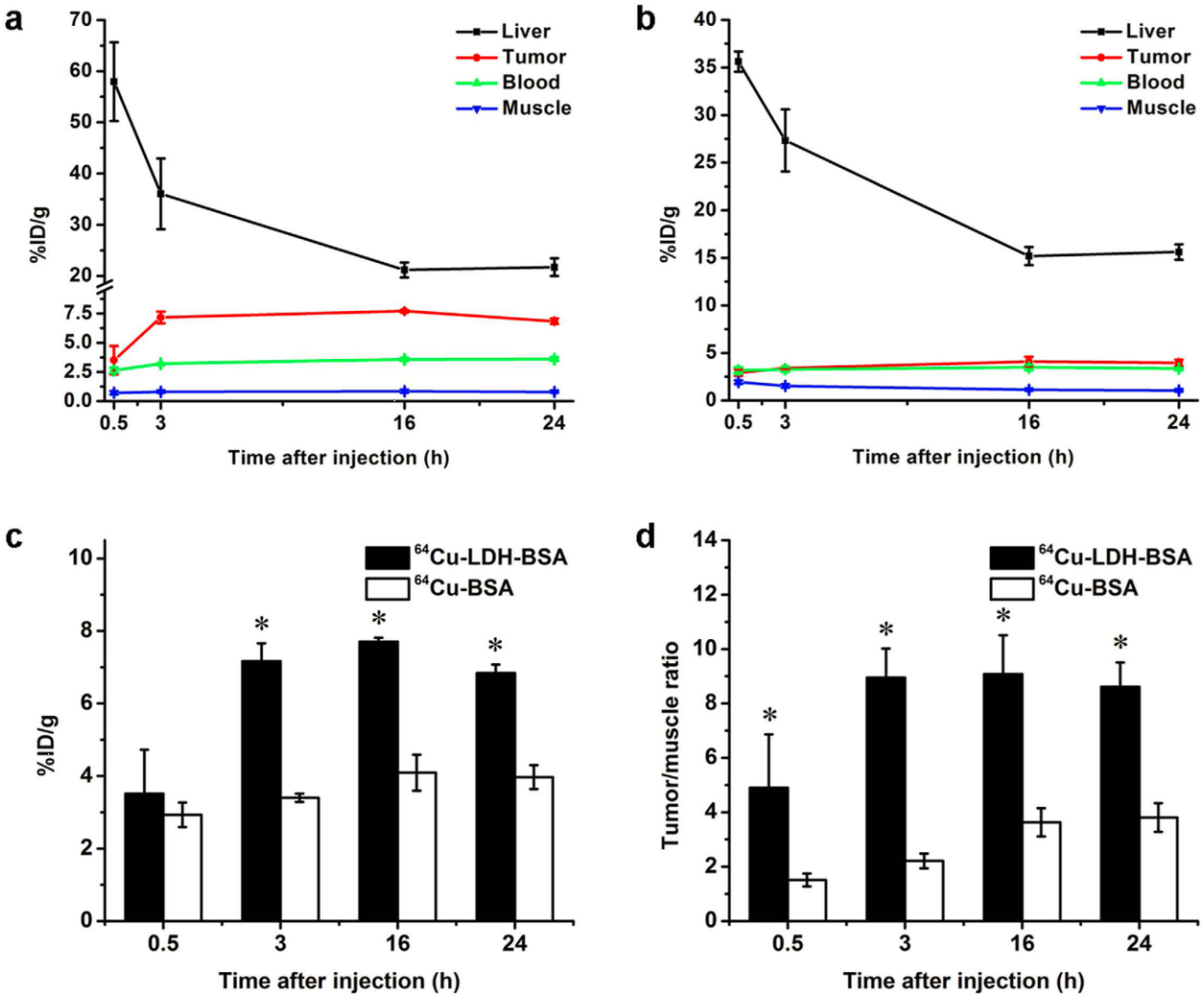

Figure 5.5. Quantitative analysis of the PET data. (**A**) Time activity curves of the liver, 4T1 tumor, blood, and muscle upon intravenous injection of ^{64}Cu-LDH-BSA. (**B**) Time activity curves of the liver, 4T1 tumor, blood, and muscle upon intravenous injection of ^{64}Cu-BSA. (**C**) Comparison of tumor uptake at different time points post injection of ^{64}Cu-LDH-BSA and ^{64}Cu-BSA. The differences of the tumor uptake were statistically significant ($P < 0.05$) at all time points except 0.5 h. (**D**) Comparison of tumor/muscle ratio at different time points post injection of ^{64}Cu-LDH-BSA and ^{64}Cu-BSA. The differences of tumor/muscle ratio were statistically significant ($P < 0.05$) at all time points. All data represent 3 mice per group.

After the last scan at 24 h p.i., 4T1 tumor-bearing mice injected with ^{64}Cu-LDH-BSA and ^{64}Cu-BSA were sacrificed for biodistribution studies. The quantitative data of the uptakes from tumor and other tissues in biodistribution studies well matched the results of ROI analysis, which confirmed the accuracy of PET imaging and ROI analysis (Figure 5.6).

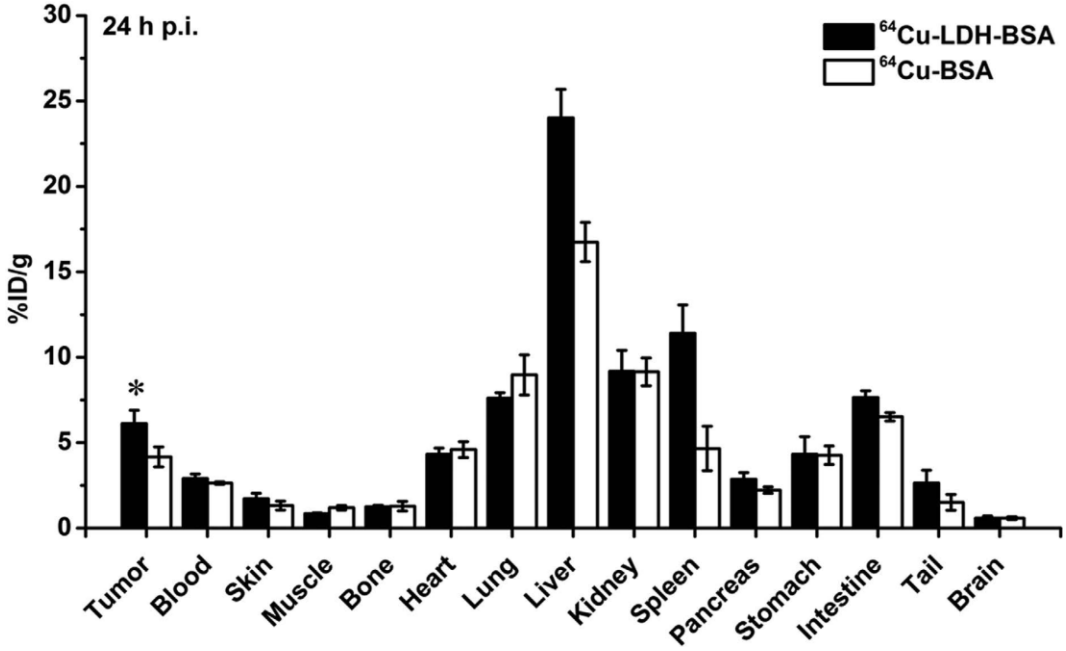

Figure 5.6. Biodistribution of ^{64}Cu-LDH-BSA and ^{64}Cu-BSA in 4T1 tumor-bearing mice. The tumor uptake of ^{64}Cu-LDH-BSA was significantly higher than that of ^{64}Cu-BSA at 24 h post injection ($P < 0.05$; $n = 3$).

5.4. Discussion

Compared with conventional chelator-based labeling, chelator-free labeling possesses several unique advantages. First, chelator-free labeling is a versatile approach, which may be suitable for various radionuclides. Therefore, one design of nanoparticles can potentially be employed in the different clinical settings. Second, it is known that incorporation of chelators could sometimes

alter the in vivo biodistribution and pharmacokinetics of nanoparticles, which may not accurately reflect the pharmacological behavior of unlabeled nanoparticles [63, 96, 146]. Chelator-free labeling which avoids the use of a chelating agent, therefore, can maintain the native pharmacokinetic profile of the nanoparticles. Third, chelator-free labeling does not require functional groups on the surface of nanoparticles for conjugation of chelators. Therefore, all the surface functional groups on the nanoparticles could be employed for further functionalization with fluorescent agents, therapeutic agents, or targeting ligands to generate multifunctional nanoplatforms. At last, the mechanism for chelator-free labeling could be very simple and effective, which allows the labeling of isotopes which could not be achieved in a traditional strategy such as ^{72}As and ^{69}Ge [95, 127, 147]. Both ^{72}As and ^{69}Ge were very challenging to label via conventional techniques, with few reported successes in the literature.

Chelator-free labeling also has several drawbacks. One of the drawbacks is that the surface modification of nanoparticles can significantly affect the labeling yield, since the surface of nanoparticles directly interacts with the isotopes during labeling. For example, BSA coating decreased the labeling yield of LDH-BSA with ^{64}Cu in this study. In addition, the labeling stability through chelator-free manner could be varied from case to case, since it is still underexplored and very few examples can be referred to. In one previous study on chelator-free labeling of As, obvious bladder uptake was observed from PET images with *As-SPION, which indicated that the labeling was not stable in vivo [127]. However, in this study, no bladder uptake was observed in vivo, suggesting a great potential of LDH nanoparticles for chelator-free labeling with excellent stability.

In this proof-of-principle study, ion-exchange is believed to play an important role in chelator-free labeling of LDH nanoparticles [148]. Through Coulombic interaction between LDH nanoparticles and metal radioisotopes, metal radioisotopes (guest species) tend to compensate for the charge deficit of LDH (host species) [148]. It allows the incorporation of various divalent and trivalent metal cations but not tetravalent metal cations. However, further studies are needed to better understand the mechanism of chelator-free labeling of LDH nanoparticles. The valence of radioisotopes might not be the only decisive factor for chelator-free labeling of LDH nanoparticles. Other factors, such as labeling buffer, temperature, pH value and concentration, might also influence the labeling results.

For nanoparticle-related imaging, toxicity of the nanoparticles is always one of concerns. Of note, LDH is considered as one of inorganic nanoparticles with low toxicity [149]. The toxicity potential of LDH is usually dose and time dependent, and the shape, size and surface charge also play a role in toxicity in vitro and in vivo [148]. In addition, aggregation or agglomeration of LDH nanoparticles upon physiological fluids is another reason to bring out possible toxicity [131, 150]. In this respect, BSA was coated onto LDH via electrostatic interaction, which is straightforward and efficient. The solubility of LDH-BSA was significantly increased to prevent the possible aggregation in vivo. Besides BSA, other molecules, such as polyethylene glycol (PEG) or Tween-80, have also been modified onto LDH nanoparticles as previously reported, which exhibited reduced toxicity in comparison with uncoated ones [151, 152]. Although LDH-nanoparticles have been proven to be highly biocompatible in vitro and many approaches have been investigated to modify the LDH surface for reduced toxicity potential, the long-term in vivo toxicity test is still of significance, considering that some elements (e.g. Al) possible lead to side

effects if taken over a certain quantity or in the presence of certain physiological environment [131, 153-155].

5.5. Conclusion

In conclusion, we achieve the first chelator-free labeling and in vivo PET imaging with LDH nanoparticles. Upon appropriate surface modification, bivalent cation $^{64}Cu^{2+}$ and tribalent $^{44}Sc^{3+}$ cation were successfully labeled on LDH and LDH-BSA with excellent labeling yield and stability. Prompt and persistent tumor uptake was also achieved with ^{64}Cu-LDH-BSA via passive targeting. Without comprising the native properties (e.g. drug loading), LDH could be a versatile platform for PET image and drug delivery.

Chapter 6 Iron Oxide Decorated MoS_2 Nanosheets with Double PEGylation for Chelator-Free Radiolabeling and Multimodal Imaging Guided Photothermal Therapy

6.1 Background

Since the discovery of graphene, ultrathin two dimensional (2D) nanomaterials have attracted tremendous interests due to their unique structures and properties [156]. Recently, transitional metal dichalcogenides (TMDCs) have emerged as next-generation 2D materials alternatives to graphene[157, 158]. With many intriguing properties similar to those of graphene, TMDCs nanosheets on the other side have abundant elemental compositions, which enable more precise tuning of their physical & chemical properties, an advantage over graphene. Therefore, in the past several years there have been numerous reports exploring the applications of TMDCs as electronic devices [159], transistors [160, 161], energy storage materials [162, 163], and catalysts [164, 165]. Recently, a few groups including ours have found that atomically thin TMDC nanosheets are also promising in the biomedical field. Chou et al. discovered that sulfur terminated molecules could be used to modify MoS_2 nanosheets to acquire better physiological stability and biocompatibility [166]. Applying their high absorbance in near-infrared (NIR) region, MoS_2 [167], WS_2 [168] or $Bi_2Se_{3[169]}$ nanosheets have been utilized in photothermal therapy of cancers. Take advantage of the large surface area attributed to 2D structure, MoS_2-based biosensors [170] and drug delivery systems [171, 172] have been developed. However, there is still much room to develop TMDC-based nanoscale platforms, particularly to integrate TMDCs with other functional nanostructures, for applications in cancer theranostics.

Multimodal imaging, which is able to compensate inherent limitations of each single imaging modality, has been an important trend in the development of new biomedical imaging instruments [173] and contrasting agents [174, 175]. On the other side, to realize personalized medicine, optimize therapeutic efficiency, and monitor therapeutic responses, imaging before, during, and after therapy has been playing increasingly important roles to guide the planning of treatment for individual patient [176]. Therefore, nanoscale theranostic platforms [177-179] with highly integrated imaging and therapy functionalities are of great interests in biomedicine nowadays.

Motivated by the above needs, in this work, we developed a multifunctional TMDC-based nano-platform for multimodal imaging guided photothermal therapy of cancer. It was found that DMSA modified IONPs could self-assemble on the surface of atomic-thin MoS_2 nanosheets, likely via sulfur chemistry occurring on the defect sites of MoS_2. Subsequently, the obtained MoS_2-IO nanocomposites were simultaneously functionalized by lipoic acid terminated polyethylene glycol (LA-PEG) which is anchored on MoS_2, and amino-terminated 6-arm PEG which is conjugated to IONPs (Figure 6.1A). Such double PEGylated MoS_2-IO (MoS_2–IO-(d)PEG) exhibited great stability in physiological environments in the presence of glutathione. Intriguingly, without the need of chelating agents, MoS_2–IO-(d)PEG could be efficiently labeled by ^{64}Cu radioisotope with high labeling yield (~70%) and great stability. Utilizing ^{64}Cu labeled nanocomposites which in the mean time exhibit high near-infrared (NIR) absorbance attributed from MoS_2 nanosheets and strong superparamagnetic property offered by decorated IONPs, triple-modal positron emission tomography (PET), photoacoustic tomography (PAT), and magnetic resonance (MR) imaging were conducted in tumor-bearing mice, revealing efficient

tumor accumulation of nanocomposites. Our work presents a facile design to incorporate many different functionalities into one single theranostic nano-platform based on TMDCs, promising for future biomedical applications.

6.2 Materials and methods

6.2.1 Reagents

Complete mouse serum was purchased from Jackson Immuno Research Laboratories (West Grove, PA). MWCO Amicon filters were purchased from Millipore (Billerica, Ma). PD-10 desalting columns were purchased from GE Healthcare (Piscataway, NJ). Water and all buffers were of Millipore grade and pretreated with Chelex 100 resin to ensure that the aqueous solution was free of heavy metal ions. All the other reaction buffers and chemicals were obtained from Thermo Fisher Scientific (Fair Lawn, NJ) and from Sigma-Aldrich (St. Louis, MO).

6.2.2. Synthesis of DMSA- IONPs

All chemicals, unless specified otherwise, were purchased from Sigma-Aldrich and used as received. IONP were synthesized in a typical organic-phase synthesis procedure. Briefly, Fe $(acac)_3$ (2 mmol), 1,2-dodecanediol (10 mmol), oleic acid (6 mmol) , oleylamine (6 mmol), and benzyl ether (20 ml) were added into a three-necked flask. After magnetically stirring under a flow of nitrogen, the mixture was heated to 200 ^{o}C for 2 h, and then heated to 300 ^{o}C for 1 h. Nitrogen protection was kept in the whole course. After cooling down to room temperature, the black-colored mixture was precipitated by ethanol (40 ml) under the ambient condition. The

sediment was washed by hexane and ethanol for several times, and re-dispersed into THF at the concentration of 5 mg ml^{-1}.

To functionalize IONPs, 100 mg DMSA was dissolved in 1 ml deionized water at pH ~10, and then dropwisely added into 20 mg IONPs dispersed in 4 ml THF under sonication. After further sonication for 1 h and then stirring for 3 h, this solution was washed with water by centrifugation at 14,800 rpm for 5 min to remove THF and excess DMSA. The precipitated DMSA modified IONPs were finally dispersed in 4 ml deionized water for further use.

6.2.3. Synthesis of MoS_2- IO-(d)PEG

MoS_2 nanosheets were synthesized by the Morrison method. Typically, 5 ml n-butyllithium in hexane was added to dissolve 1 mg MoS_2 bulk powder in a glove box under the protection of nitrogen gas. After two days of intercalation, the MoS_2 solution was washed by hexane. The precipitation was taken out from the glove box and then dissolved into 100 ml deionized water. During ultrasonication, the lithium atoms between MoS_2 layers would react with water and rapidly produce copious hydrogen gas to push MoS_2 nanosheets away from each other. At last, multilayered MoS_2 was discarded by centrifugation under 6,000 rpm for 15 min, and excess hexane and lithium ions were removed by dialyzing against deionized water, yielding water-soluble single-layered MoS_2 nanosheets.

To prepare MoS_2-IO nanocomposites, an aqueous solution of MoS_2 nanosheets (1 mg ml^{-1}) was slowly added into an aqueous solution of DMSA modified IONPs (1 mg ml^{-1}) at different

feeding mass ratios (MoS_2 : IONPs = 1:2, 1:5, and 1:10) under sonication. After magnetic stirring overnight, the nanocomposites were precipitated by adding saline and centrifugation. The obtained MoS_2-IONPs were re-dispersed in water with the concentration of 1 mg ml^{-1}.

LA-PEG was synthesized following a reported protocol [180]. 10 mg LA-PEG was added into 12 mg MoS_2-IO (2 mg MoS_2) in water under sonication. The solution was then stirred overnight to modify MoS_2 nanosheets via sulfur chemistry, obtaining MoS_2-IO-(s)PEG with better stability in PBS. For further PEGylation, 10 mg of 6-arm-PEG-amine (10 kDa) were mixed with MoS_2-IO-(s) PEG. 10 mg EDC was added every 30 min for 3 times to initiate the reaction between amino groups on 6-arm-PEG-amine and carboxyl group on DMSA modified IONPs. Excess PEG polymers were removed by centrifugal filtration with 100 kDa molecular weight cut-off (MWCO) filters (Millipore) and several times of water washing. The obtained MoS_2-IO-(d)PEG was re-dispersed in water for further use.

6.2.4. Characterization

TEM images were obtained using a FEI Tecnai F20 transmission electron microscope at an acceleration voltage of 200 kV. UV-vis-NIR spectra were obtained with PerkinElmer Lambda 750 UV-vis-NIR spectrophotometer. Heating curves were recorded by an IR thermal camera (IRS E50 Pro Thermal Imaging Camera). The real ratio of MoS_2 and IONPs were tested by ICP-AES (Vista Mpx 700-ES).

6.2.5. Cell lines and animal model

4T1 murine breast cancer, MCF-7 human breast cancer, and HUVECs were obtained from the American Type Culture Collection (ATCC, Manassas, VA) and cultured as previously described. Cells were used for in vitro and in vivo experiments when they reached ~80% confluence. All animal studies were conducted under a protocol approved by the University of Wisconsin Institutional Animal Care and Use Committee. Four- to five-week-old female BALB/c mice (Harlan, Indianapolis, IN) were each injected with 2×10^6 4T1 cells in the flank to generate the 4T1 breast cancer model. The mice were used for in vivo experiments when the tumor diameter reached 6-8 mm.

6.2.7. ^{64}Cu-labeling and serum stability studies

^{64}Cu was produced with an onsite cyclotron (GE PETtrace). $^{64}CuCl_2$ (148 MBq) was diluted in 300 ml of 0.1 M sodium acetate buffer (pH 5.5) and mixed with 30 μL of MoS_2-IO-(d)PEG (2 mg ml^{-1}). The reaction was conducted at 37 ºC for 60 min with constant shaking and the labeling yield was determined by thin-layer chromatography (TLC) at different time points. The resulting ^{64}Cu- MoS_2-IO-(d)PEG was purified by PD-10 column using PBS as the mobile phase.

To ensure that ^{64}Cu-MoS_2-IO-(d)PEG was sufficiently stable for in vivo applications, serum stability studies were carried out. ^{64}Cu- MoS_2-IO-(d)PEG was incubated in complete mouse serum and PBS at 37 ºC for up to 48 h. Portions of the mixture were sampled at different time points and filtered through 100 kDa MWCO filters. The radioactivity that remained on the filter was measured after discarding the filtrate, and retained (i.e., intact) ^{64}Cu-MoS_2-IO-(d)PEG was calculated using the equation (radioactivity on filter/total radioactivity × 100%).

6.2.8. In vivo multimodal imaging

PET scans of 4T1 tumor-bearing mice (4 mice per group) at various time points post i.v. injection of 5-10 MBq of ^{64}Cu-MoS_2-IO-(d)PEG were performed using a microPET/microCT Inveon rodent model scanner (Siemens Medical Solutions USA, Inc.). Data acquisition, image re-construction, and region-of-interest (ROI) analysis of the PET data were performed as described previously [67, 181-183]. Quantitative PET data of the 4T1 tumor and major organs was presented as percentage injected dose per gram of tissue (%ID/g). After the last scan at 24 h p.i., biodistribution studies were carried out to confirm that the %ID/g values based on PET imaging truly represented the radioactivity distribution in mice. Mice were euthanized and 4T1 tumor, blood and major organs/tissues were collected and wet-weighed. The radioactivity in the tissue was measured using a γ-counter (PerkinElmer) and presented as %ID/g (mean ± SD).

PAT imaging was conducted by a photoacoustic computed tomography scanner (Endra Nexus 128, Ann Arbor, MI). During PAT imaging, anesthesia was maintained using pentobarbital (50 mg/kg) and the body temperature of the mice was kept by a water heating system at 37.5 °C. T2-weighted MR imaging was performed by a 9.4T MR scanner designed for small animal imaging (Bruker Biospin Corporation, Billerica, MA).

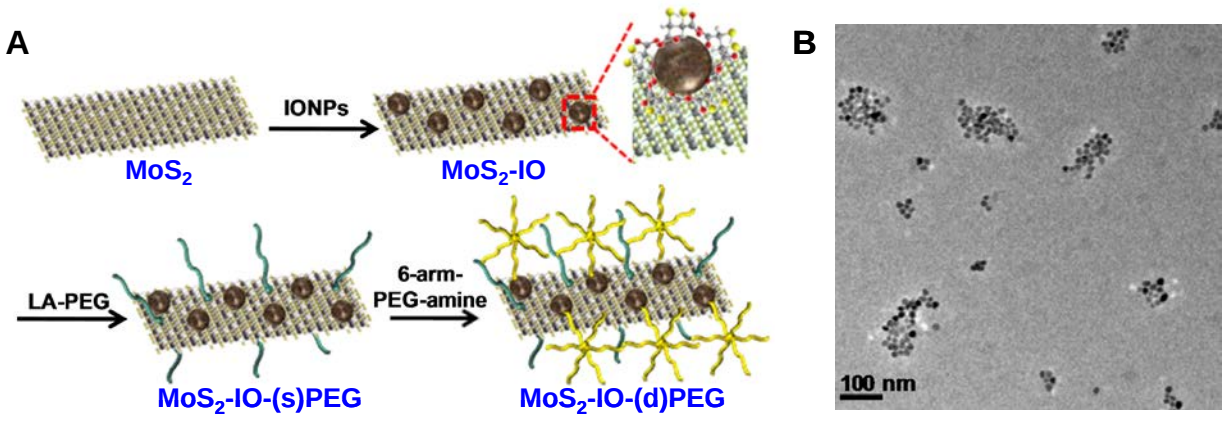

Figure 6.1. Synthesis and characterization of MoS_2–IO-(d)PEG nanoparticles. (**A**) Schematic illustration of the synthesis process of MoS_2–IO-(d)PEG nanoparticles. (**B**) TEM image of MoS_2–IO-(d)PEG nanoparticles.

6.3. Results and Discussions

6.3.1. Systhesis of MoS2–IO-(d)PEG nanoparticles

Single-layered MoS_2 nanosheets were synthesized by the Morrison method[184], a commonly adopted method to exfoliate TMDCs in large scales. Typically, bulk MoS_2 was inserted by n-butyllithium in hexane under protection of N_2 in a glove box. After departing excess lithium and hexane, the precipitate was taken out and sonicated in water, followed by washing via centrifugation and dialysis to obtain water-soluble single-layered MoS_2 nanosheets. As revealed by transmission electron microscopy (TEM) (Figure 6.1B), as-made MoS_2 nanosheets were mostly single-layer sheets with sizes in the range of 50 nm - 200 nm. During drastic intercalation and exfoliation, some of sulfur atoms would be lost from the sandwich surface of MoS_2 nanosheets, forming defects available for binding by sulfur terminated molecules[166]. Ultra-small IONPs synthesized by the classical thermo-decomposition method and functionalized with DMSA were then mixed with as-made MoS_2 nanosheets under ultra-sonication. Although both

negatively charged, DMSA modified IONPs could self-assemble on the MoS_2 surface as a well-controlled single particle-layer, owing to the binding of thiol groups on DMSA coated IONPs to the defect sites on MoS_2 nanosheets. The exact MoS_2: IONPs mass ratio in the final product was measured by inductively coupled plasma atomic emission spectroscopy (ICP-AES) to be 1:6.4. Compared with previously reported methods to synthesize TMDC-nanoparticle composites in which Au, Ag, Pd[185] , or Fe_3O_4 nanoparticles[186] were directly grown on the surface of TMDC nanosheets, our method relying on the self-assembly of pre-made high quality nanoparticles synthesized by the state-of-art method on the surface of TMDCs is a rather easy and controllable approach.

Although soluble in water, MoS_2–IO would quickly aggregate and precipitate in the presence of salts. Next, to enhance the stability of our nanocomposite in physiological solutions to enable further biomedical applications, thiolated polymer LA-PEG was adopted to modify MoS_2–IO just like the way to prepare PEGylated WS_2 [168] or MoS_2 [171, 172] nanosheets (Figure 6.1A). After stirring overnight, the disulfide group of LA-PEG was strongly bonded to the defect site on MoS_2, obtaining MoS_2–IO-(s)PEG with great stability in saline. However, different from as-made MoS_2, the number of surface defects reactive to LA-PEG in the MoS_2–IO composite should be lower due to occupation of IONPs on the surface of MoS_2 nanosheets, reducing PEGylation efficiency. In the presence of glutathione, a thiol-containing molecule widely found in physiological environments, such MoS_2–IO-(s)PEG showed obviously reduced stability owing to the replacement of LA-PEG by glutathione. To further improve the physiological stability of our nanocomposite, amine-terminated branched PEG was then conjugated to the carboxyl groups on the IONP surface via amide formation. The obtained MoS_2 with double PEGylation (MoS_2–

IO-(d)PEG) showed the same uniform single particle-layer structure (Figure 6.1A) with slightly larger hydrodynamic size compared to MoS_2–IO-(s)PEG. Due to the enhancement in PEGylation efficiency, MoS_2–IO-(d)PEG exhibited excellent stability in the saline solution containing glutathione. In addition, although not demonstrated in this work, the free amine groups on the surface of MoS_2–IO-(d)PEG sheets would be available for conjugation of other functional biomolecules (e.g. fluorescent dyes, targeting molecules). The final composition nanoparticles showed neutralized surface charge, which is also preferred for applications in biological environments. Notably, direct conjugation of amine-terminated branched PEG to as-made MoS_2–IO was not as effective owing to the salt-induced aggregation of nanomaterials during the conjugation process, in which 1-Ethyl-3-(3-dimethylaminopropyl)carbodiimide · HCl (EDC·HCl) was added to trigger the amide formation.

6.3.2. Chelator-free radiolabeling and radiostability

^{64}Cu labeling was straightforwardly executed by mixing $^{64}CuCl_2$ with MoS_2-PEG or MoS_2–IO-(d)PEG at 37 ºC for 60 min under constant shaking. As determined by TLC at different time points (Fig. 6.2A), we found that ^{64}Cu was immediately adsorbed onto MoS_2-PEG and MoS_2–IO-(d)PEG nanosheets, with labeling yields measured to be as high as 85 % and 70 % after 60 min of incubation, respectively (Figure 6.2B). In contrast, control experiment by labeling PEGylated IONPs with ^{64}Cu by the same procedure resulted in a negligible labeling yield, suggesting that free ^{64}Cu ions could be attached on the surface of MoS_2 nanosheets but not on IONPs (Figure 6.2B). Such labeling is possibly due to the anchoring of Cu^{2+} ions on the Mo defect sites of MoS_2 nanosheets.

To ensure that the ^{64}Cu labeling on MoS_2–IO-(d)PEG was sufficiently stable for in vivo applications, serum stability test was carried out. By measuring the remained radioactivities in those samples, we found that ^{64}Cu labeling in ^{64}Cu-MoS_2–IO-(d)PEG was highly stable within 48 h in serum (Figure 6.2B) [187]. Therefore, ^{64}Cu labeled MoS_2–IO-(d)PEG could be adopted as a non-invasive PET imaging contrast agent to precisely reveal its biodistribution and pharmacokinetics in vivo.

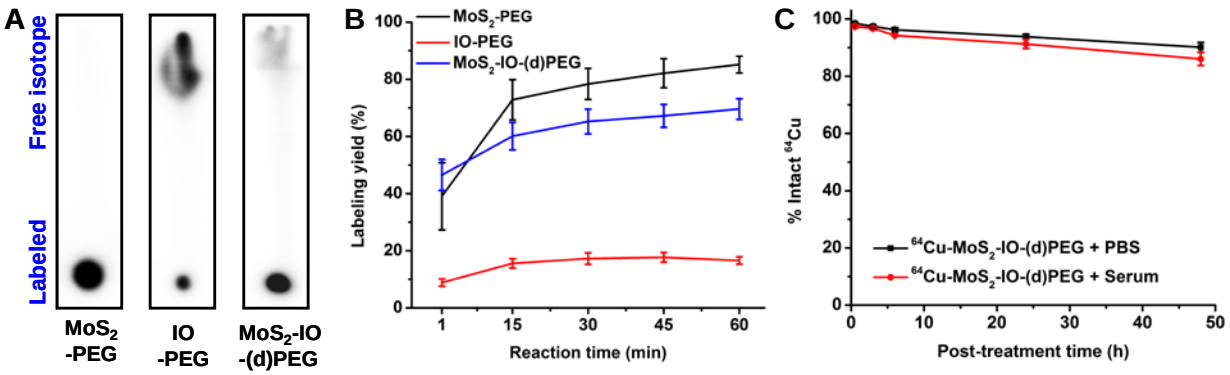

Figure 6.2. Chelator-free labeling of MoS_2–IO-(d)PEG nanoparticles. (**A**) Autoradiographic images of TLC plates of MoS_2–PEG, IO-PEG and MoS_2–IO-(d)PEG after chelator-free labeling with ^{64}Cu for 60 min. (**B**) The labeling yield of MoS_2–PEG, IO-PEG and MoS_2–IO-(d)PEG after chelator-free labeling with ^{64}Cu at different reaction times calculated from autoradiography images of TLC plates. (**C**) Labeling stability of MoS_2–IO-(d)PEG nanoparticles in both PBS and mouse serum for 60 min incubation (n = 3).

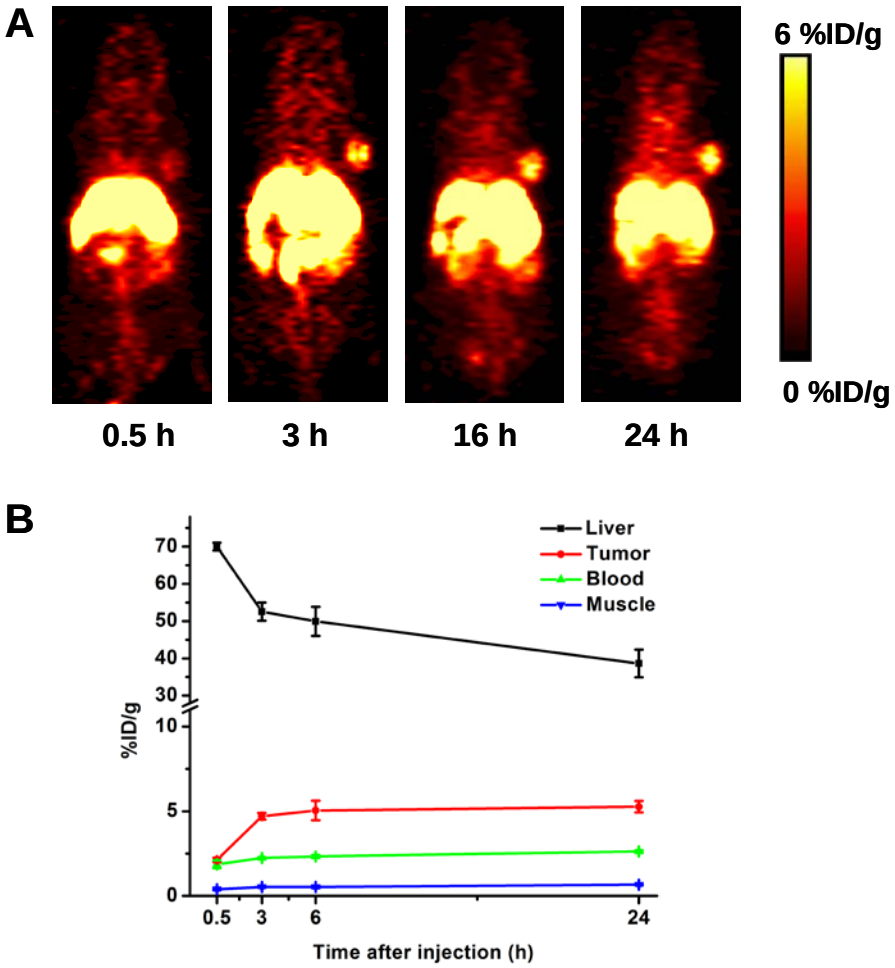

Figure 6.3. In vivo PET imaging. (**A**) Serial coronal PET images at different time points post-injection of ^{64}Cu-MoS_2–IO-(d)PEG were acquired in 4T1 tumor-bearing mice. (**B**) Time activity curves of the liver, 4T1 tumor, blood, and muscle upon intravenous injection of ^{64}Cu-MoS_2–IO-(d)PEG. All data represent 3 mice per group (n = 3).

6.3.3. In vivo multimodal tumor imaging

PET scans of 4T1 tumor-bearing mice at various time points post intravenous (i.v.) injection of ^{64}Cu-MoS_2–IO-(d)PEG (5-10 MBq) were performed using a microPET Inveon rodent model scanner (Figure 6.3A). Obvious tumor contrast was observed at 3 h after injection, suggesting

effective tumor retention of nanocomposites due to the enhanced permeability and retention effect (EPR) of cancerous tumors. Quantitative PET data presented as percentage injected dose per gram of tissue (%ID/g) further confirmed the time-dependent increase of ^{64}Cu signals in the tumor post injection of ^{64}Cu-MoS_2–IO-(d)PEG (Figure 6.3B). In order to further understand the in vivo biodistribution of MoS_2–IO-(d)PEG, mice were sacrificed 24 h after injection of ^{64}Cu labeled nanocomposites and the radioactivities in major tissues and organs were measured using a γ-counter (Figure 6.4). In addition to the tumors, high radioactivities were also noted in liver and spleen, which were RES organs responsible for the clearance of foreign nanoparticles by macrophage uptake [188].

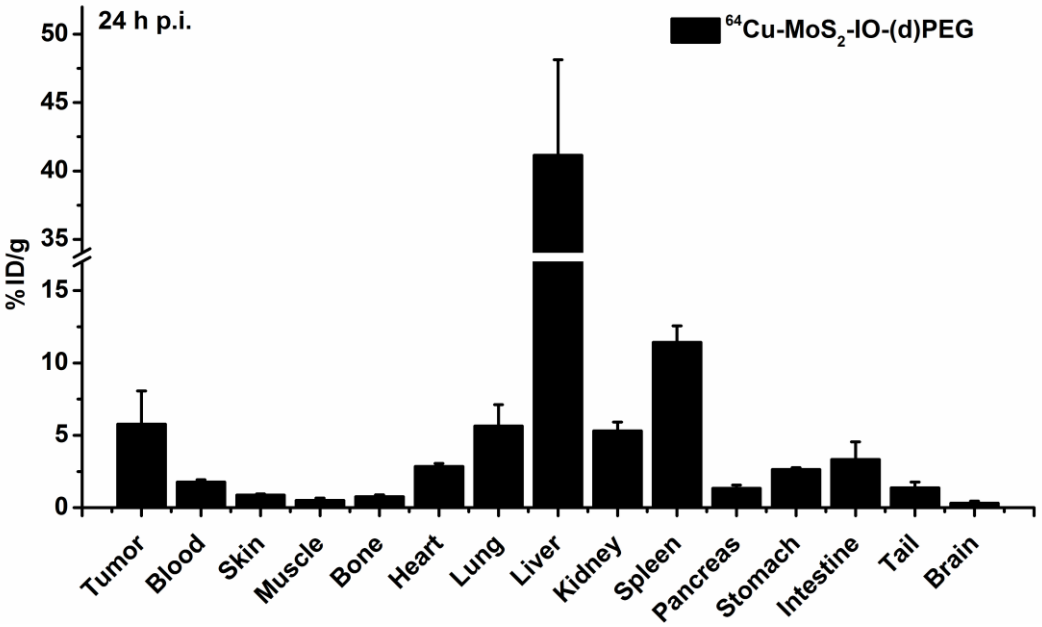

Figure 6.4. Ex vivo biodistribution studies of ^{64}Cu-MoS_2–IO-(d)PEG in 4T1 tumor-bearing mice. All data represent 3 mice per group (n = 3).

Photoacoustic imaging is a newly-developed method combining the high contrast of optical imaging and deep tissue penetration of ultrasound based on the photoacoustic effect [189]. In

photoacoustic imaging, optical energy absorbed by light-absorbing tissues or contrasting agents would result in thermoelastic expansion that creates reflected ultrasound signals [110]. In our experiments, mice were i.v. injected with MoS_2–IO-(d)PEG nanosheets ([MoS_2] = 0.68 mg ml^{-1}, 0.2 ml). Compared to the photoacoustic image of tumor before injection, strong PAT signals showed up after i.v. injection of MoS_2–IO-(d)PEG (Figure 6.5A), suggesting highly efficient tumor retention of our NIR-absorbing nano-agent.

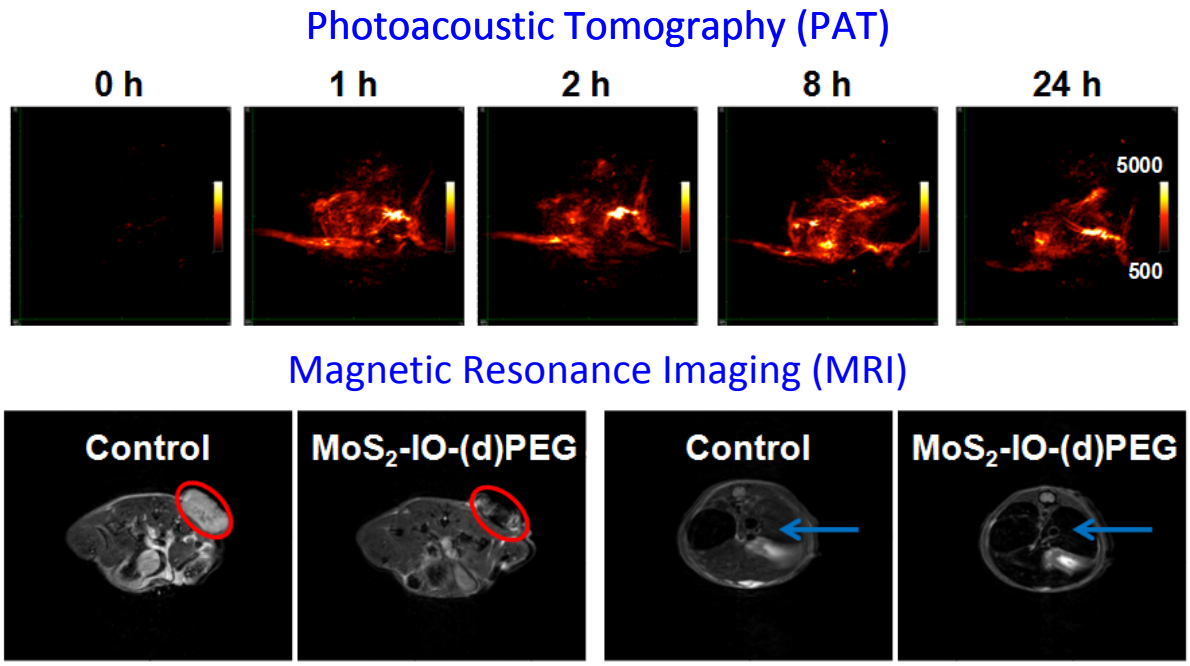

Figure 6.5. In vivo PAT and MR imaging. (**A**) PAT images of tumor on mice acquired before and at various time points after i.v. injection with MoS_2-IO-(d)PEG (dose of MoS_2 = 6.85 mg/kg). (**B**) T_2-weighted MR images showing the transverse sections of a tumor-bearing mouse before and after injection with MoS_2-IO-(d)PEG (dose of MoS_2 = 6.85 mg/kg). The red circles and blue arrows highlight the 4T1 tumor and liver of mice, respectively.

While PET imaging values in high sensitivity tracking of positron-emitting radiotracers and photoacoustic imaging provides useful information regarding the distribution of nanoparticles inside the tumor, MR imaging would be able to show high soft-tissue contrast with anatomic information [173]. For MR imaging, 4T1 tumor-bearing mice i.v. injected with MoS_2–IO-(d)PEG were imaged by a 9 T MR Scanner before injection and 24 h post injection (p.i.) ([MoS_2] = 0.68 mg ml^{-1}, 0.2 ml). Compared to untreated mice, the tumor of mice 24 h p.i. showed obvious darkening effects in T2-weighted MR images, indicating the prominent passive accumulation of MoS_2–IO-(d)PEG in the tumor (Figure 6.5B). Meanwhile, RES organs such as liver also showed strong darkening contrast, consistent with PET imaging results.

6.4. Conclusion

In summary, a novel 2D nanocomposite by self-assembly of IONPs on MoS_2 nanosheets is successfully fabricated and functionalized with dual PEG coatings to achieve enhanced biocompatibility. It was found that such nanocomposite could be efficiently labeled with PET isotope ^{64}Cu by simple mixing without the need of chelation chemistry. Utilizing ^{64}Cu labeled MoS_2–IO-(d)PEG which in the mean time exhibits high NIR absorbance and strong T2 MR contrast, triple modal PET, photoacoustic, and MR imaging was conducted on 4T1 tumor-bearing mice, revealing time-dependent tumor retention of nanoparticles after i.v. injection. Our work shows the great potential of TMDCs as a 2D platform to construct nanoscale theranostic agents with highly integrated functionalities.

Chapter 7 Summary and Perspectives

In this dissertation, three novel nanomaterials are explored; graphene, LDH, and MoS_2. Unlike the traditional nanocarriers, these next-generation nanomaterials possess intrinsic diagnostic or therapeutic potential, making them tremendously attractive in the research community. For example, the unique structure of graphene can be used for different types of drug and gene delivery. The strong π-π interaction allows for the loading of various aromatic drug molecules such as doxorubicin (DOX) [105, 190-192] and camptothecin (CPT) [105, 193, 194], while hydrophobic surface provides a chance to bind to numerous poorly water-soluble drugs, such as paclitaxel, without compromising their potency or efficiency In addition, the strong light absorbance and heat conversion ability make it useful in photothermal and photodynamic therapy to eliminate the tumor without damaging the normal tissue. LDH is another promising nanomaterial for drug delivery. Distinct charge among layers provides a versatile platform to load different positively or negatively charged drugs, while the dynamic chemical composition significantly enhances the drug loading efficiency. Similar to graphene, MoS_2 exhibits strong NIR absorbance and can be used in photothermal and photodynamic therapy. Elemental composition of transition metal dichalcogenides enables more precise tuning of their physical and chemical properties.

Since nanomaterials are highly useful for cancer treatment, to understand their in vivo behavior becomes extremely important for the development of novel nanomaterials for biomedical applications. Taking advantage of PET, we have examined the in vivo biodistribution of ^{64}Cu-labeled RGO, GO, LDH and MoS_2 nanoparticles. Even without targeting ligands, the PEGylated or BSA-coating nanoparticles exhibited prompt tumor retention as early as 3 h p.i. via EPR effect.

The tumor uptake was further enhanced (~ 2 fold) by conjugating anti-angiogenesis antibody TRC105 and protein $VEGF_{121}$, which exhibited excellent tumor contrast and tumor vasculature specificity. Compared with cancer cell targeting, angiogenesis targeting is especially suitable to nanoparticles due to their relatively large size and difficulty in tumor extravasation. Angiogenesis targeting is one of the most important aspects that need to be further investigated for nanoparticle-based tumor targeting.

Although NOTA-chelation has been considered as the gold standard and widely practiced in our previous studies, the accuracy of PET images of NOTA-linked nanoparticles is always questionable. On the contrary, chelator-free radiolabeling has emerged as a novel labeling approach that avoids the use of chemical chelators, so as to maintain the native pharmacokinetics and truly reflect the biodistribution of the nanoparticles. Compared with conventional chelator-based labeling, chelator-free labeling has numerous other advantages. For example, chelator-free labeling is a versatile approach, which may be suitable for various radionuclides. Therefore, one design of nanoparticles can potentially be employed in different clinical settings. In addition, chelator-free labeling does not require functional groups on the surface of nanoparticles for conjugation of chelators. Therefore, all the surface functional groups on the nanoparticles could be employed for further functionalization with fluorescent agents, therapeutic agents or targeting ligands to generate multifunctional nanoplatforms. Last but not least, the mechanism for chelator-free labeling could be very simple and effective, making it especially useful on some new nanoparticles which prove difficult for functionalization with chelators such as NOTA. The gold standard was broken by the chelator-free labeling with graphene. Although both ^{64}Cu-RGO-PEG and ^{64}Cu-NOTA-PEG-RGO are stable in vitro, the in vivo stability of ^{64}Cu-RGO-PEG was

higher. We also surprisingly found that NOTA itself can be loaded on graphene and lead to incorrect signals in PET imaging. Therefore bypassing the use of NOTA becomes especially important for certain nanoparticle-based PET imaging applications. Chelator-free labeling and tumor imaging were further demonstrated with ^{64}Cu-labelled LDH and MoS_2 nanoparticles.

Besides the nanoparticles that were investigated in this dissertation, several other materials are also very promising, to serve as theranostic platforms. One of the best examples is silica nanoparticle, which is generally recognized as safe by the United States Food and Drug Administration (FDA) and can be employed for drug and gene delivery, photothermal therapy, photodynamic therapy and molecular imaging after appropriate surface engineering. By coating a porous shell around a large central cavity inside the nanoparticle, hollow mesoporous silica nanoparticles can be prepared with enhanced drug loading and imaging capacity. Recently, ^{89}Zr was found to successfully label mesoporous silica nanoparticles with extreme stability via chelator-free mechanism [128], making silica-based nanoparticle a promising direction to work on.

The future direction of molecular imaging and nanotechnology is increasingly interdisciplinary, requiring researchers to possess a combination of expertise in varied fields. The research in this dissertation covers a broad range of areas including biology, chemistry, materials science, nanotechnology, oncology and radiology, which have offered me the precious opportunity of training in all the relevant fields. Besides the work on nanomaterial-based molecular imaging, I also lead several antibody-related PET imaging projects [103, 195]. Prof. Weibo Cai spent tremendous time and effort on guiding my work and provided me valuable opportunities to write several review articles [11, 196] and present in several world-known conferences, all of which have contributed to

my growth as a scientist. In addition, the reported research was accomplished in collaboration with Prof. Zhuang Liu's group at Soochow University and Prof. Zhi Ping Xu's group at The University of Queensland. Both Prof. Liu and Prof. Xu are eminent researchers in their research fields. From the international collaborations, I have developed not only a deeper understanding of the proposed collaborative work but also an unfettered mind to benefit my whole academic life.

References:

[1] Massoud TF, Gambhir SS. Molecular imaging in living subjects: seeing fundamental biological processes in a new light. Genes Dev. 2003;17:545-80.

[2] Cai W, Hsu AR, Li ZB, Chen X. Are quantum dots ready for in vivo imaging in human subjects? Nanoscale Res Lett. 2007;2:265-81.

[3] Weissleder R, Pittet MJ. Imaging in the era of molecular oncology. Nature. 2008;452:580-9.

[4] Haberkorn U, Strauss LG, Reisser C, Haag D, Dimitrakopoulou A, Ziegler S, et al. Glucose uptake, perfusion, and cell proliferation in head and neck tumors: relation of positron emission tomography to flow cytometry. J Nucl Med. 1991;32:1548-55.

[5] Cai W, Zhang X, Wu Y, Chen X. A thiol-reactive 18F-labeling agent, N-[2-(4-18F-fluorobenzamido)ethyl]maleimide, and synthesis of RGD peptide-based tracer for PET imaging of alpha v beta 3 integrin expression. J Nucl Med. 2006;47:1172-80.

[6] Wang H, Cai W, Chen K, Li ZB, Kashefi A, He L, et al. A new PET tracer specific for vascular endothelial growth factor receptor 2. Eur J Nucl Med Mol Imaging. 2007;34:2001-10.

[7] Hong H, Yang Y, Zhang Y, Engle JW, Barnhart TE, Nickles RJ, et al. Positron emission tomography imaging of CD105 expression during tumor angiogenesis. Eur J Nucl Med Mol Imaging. 2011;38:1335-43.

[8] Haddad D, Zanzonico PB, Carlin S, Chen CH, Chen NG, Zhang Q, et al. A vaccinia virus encoding the human sodium iodide symporter facilitates long-term image monitoring of virotherapy and targeted radiotherapy of pancreatic cancer. J Nucl Med. 2012;53:1933-42.

[9] Varma NR, Janic B, Iskander AS, Shankar A, Bhuiyan MP, Soltanian-Zadeh H, et al. Endothelial progenitor cells (EPCs) as gene carrier system for rat model of human glioma. PLoS One. 2012;7:e30310.

[10] Cai W, Chen X. Nanoplatforms for targeted molecular imaging in living subjects. Small. 2007;3:1840-54.

[11] Shi S, Chen F, Ehlerding EB, Cai W. Surface engineering of graphene-based nanomaterials for biomedical applications. Bioconjug Chem. 2014;25:1609-19.

[12] Goel S, Chen F, Cai W. Synthesis and biomedical applications of copper sulfide nanoparticles: from sensors to theranostics. Small. 2014;10:631-45.

[13] Chen F, Ehlerding EB, Cai W. Theranostic nanoparticles. J Nucl Med. 2014;55:1919-22.

[14] Bruchez Jr M. Semiconductor Nanocrystals as Fluorescent Biological Labels. Science. 1998;281:2013-6.

[15] Chan WC, Nie S. Quantum dot bioconjugates for ultrasensitive nonisotopic detection. Science. 1998;281:2016-8.

[16] Balasubramanian K, Burghard M. Chemically functionalized carbon nanotubes. Small. 2005;1:180-92.

[17] Lacerda L, Bianco A, Prato M, Kostarelos K. Carbon nanotubes as nanomedicines: from toxicology to pharmacology. Adv Drug Deliv Rev. 2006;58:1460-70.

[18] Hirsch LR, Gobin AM, Lowery AR, Tam F, Drezek RA, Halas NJ, et al. Metal nanoshells. Ann Biomed Eng. 2006;34:15-22.

[19] Thorek DL, Chen AK, Czupryna J, Tsourkas A. Superparamagnetic iron oxide nanoparticle probes for molecular imaging. Ann Biomed Eng. 2006;34:23-38.

[20] Novoselov KS, Geim AK, Morozov SV, Jiang D, Zhang Y, Dubonos SV, et al. Electric field effect in atomically thin carbon films. Science. 2004;306:666-9.

[21] Geim AK, Novoselov KS. The rise of graphene. Nat Mater. 2007;6:183-91.

[22] Service RF. Materials science. Carbon sheets an atom thick give rise to graphene dreams. Science. 2009;324:875-7.

[23] Pumera M. Graphene-based nanomaterials and their electrochemistry. Chem Soc Rev. 2010;39:4146-57.

[24] Li X, Wang X, Zhang L, Lee S, Dai H. Chemically derived, ultrasmooth graphene nanoribbon semiconductors. Science. 2008;319:1229-32.

[25] Huang X, Yin Z, Wu S, Qi X, He Q, Zhang Q, et al. Graphene-based materials: synthesis, characterization, properties, and applications. Small. 2011;7:1876-902.

[26] Novoselov KS, Fal'ko VI, Colombo L, Gellert PR, Schwab MG, Kim K. A roadmap for graphene. Nature. 2012;490:192-200.

[27] Feng L, Liu Z. Graphene in biomedicine: opportunities and challenges. Nanomedicine (Lond). 2011;6:317-24.

[28] Yang K, Feng L, Shi X, Liu Z. Nano-graphene in biomedicine: theranostic applications. Chem Soc Rev. 2012;42:530-47.

[29] Zhang Y, Nayak TR, Hong H, Cai W. Graphene: a versatile nanoplatform for biomedical applications. Nanoscale. 2012;4:3833-42.

[30] Davis ME, Chen ZG, Shin DM. Nanoparticle therapeutics: an emerging treatment modality for cancer. Nat Rev Drug Discov. 2008;7:771-82.

[31] Torchilin VP. Recent advances with liposomes as pharmaceutical carriers. Nat Rev Drug Discov. 2005;4:145-60.

[32] Peer D, Karp JM, Hong S, Farokhzad OC, Margalit R, Langer R. Nanocarriers as an emerging platform for cancer therapy. Nat Nanotechnol. 2007;2:751-60.

[33] Hong H, Yang K, Zhang Y, Engle JW, Feng L, Yang Y, et al. In vivo targeting and imaging of tumor vasculature with radiolabeled, antibody-conjugated nanographene. ACS Nano. 2012;6:2361-70.

[34] Zhang Y, Hong H, Severin GW, Engle JW, Yang Y, Goel S, et al. ImmunoPET and near-infrared fluorescence imaging of CD105 expression using a monoclonal antibody dual-labeled with ^{89}Zr and IRDye 800CW. Am J Transl Res. 2012;4:333-46.

[35] Ruoslahti E, Bhatia SN, Sailor MJ. Targeting of drugs and nanoparticles to tumors. J Cell Biol. 2010;188:759-68.

[36] Hong H, Zhang Y, Sun J, Cai W. Molecular imaging and therapy of cancer with radiolabeled nanoparticles. Nano Today. 2009;4:399-413.

[37] Hanahan D, Weinberg RA. The hallmarks of cancer. Cell. 2000;100:57-70.

[38] Seon BK, Haba A, Matsuno F, Takahashi N, Tsujie M, She X, et al. Endoglin-targeted cancer therapy. Curr Drug Deliv. 2011;8:135-43.

[39] Fonsatti E, Nicolay HJ, Altomonte M, Covre A, Maio M. Targeting cancer vasculature via endoglin/CD105: a novel antibody-based diagnostic and therapeutic strategy in solid tumours. Cardiovasc Res. 2010;86:12-9.

[40] Feng L, Zhang S, Liu Z. Graphene based gene transfection. Nanoscale. 2011;3:1252-7.

[41] Dallas NA, Samuel S, Xia L, Fan F, Gray MJ, Lim SJ, et al. Endoglin (CD105): a marker of tumor vasculature and potential target for therapy. Clin Cancer Res. 2008;14:1931-7.

[42] Rosen LS, Hurwitz HI, Wong MK, Goldman J, Mendelson DS, Figg WD, et al. A phase I first-in-human study of TRC105 (Anti-Endoglin Antibody) in patients with advanced cancer. Clin Cancer Res. 2012;18:4820-9.

[43] Gambhir SS. Molecular imaging of cancer with positron emission tomography. Nat Rev Cancer. 2002;2:683-93.

[44] Alauddin MM. Positron emission tomography (PET) imaging with ^{18}F-based radiotracers. Am J Nucl Med Mol Imaging. 2012;2:55-76.

[45] Eary JF, Hawkins DS, Rodler ET, Conrad EUI. ^{18}F-FDG PET in sarcoma treatment response imaging. Am J Nucl Med Mol Imaging. 2011;1:47-53.

[46] Grassi I, Nanni C, Allegri V, Morigi JJ, Montini GC, Castellucci P, et al. The clinical use of PET with ^{11}C-acetate. Am J Nucl Med Mol Imaging. 2012;2:33-47.

[47] Liu X, Tao H, Yang K, Zhang S, Lee ST, Liu Z. Optimization of surface chemistry on single-walled carbon nanotubes for in vivo photothermal ablation of tumors. Biomaterials. 2011;32:144-51.

[48] Hong H, Zhang Y, Severin GW, Yang Y, Engle JW, Niu G, et al. Multimodality Imaging of Breast Cancer Experimental Lung Metastasis with Bioluminescence and a Monoclonal Antibody Dual-Labeled with ^{89}Zr and IRDye 800CW. Mol Pharm. 2012;9:2339-49.

[49] Hong H, Zhang Y, Engle JW, Nayak TR, Theuer CP, Nickles RJ, et al. In vivo targeting and positron emission tomography imaging of tumor vasculature with ^{66}Ga-labeled nano-graphene. Biomaterials. 2012;33:4147-56.

[50] Choi HS, Liu W, Misra P, Tanaka E, Zimmer JP, Itty Ipe B, et al. Renal clearance of quantum dots. Nat Biotechnol. 2007;25:1165-70.

[51] Robinson JT, Tabakman SM, Liang Y, Wang H, Casalongue HS, Vinh D, et al. Ultrasmall reduced graphene oxide with high near-infrared absorbance for photothermal therapy. J Am Chem Soc. 2011;133:6825-31.

[52] Iagaru A. ^{18}F-FDG PET/CT: timing for evaluation of response to therapy remains a clinical challenge. Am J Nucl Med Mol Imaging. 2011;1:63-4.

[53] Vach W, Høilund-Carlsen PF, Fischer BM, Gerke O, Weber W. How to study optimal timing of PET/CT for monitoring of cancer treatment. Am J Nucl Med Mol Imaging. 2011;1:54-62.

[54] Zhang Y, Hong H, Engle JW, Bean J, Yang Y, Leigh BR, et al. Positron emission tomography imaging of CD105 expression with a ^{64}Cu-labeled monoclonal antibody: NOTA is superior to DOTA. PLoS One. 2011;6:e28005.

[55] Dearling JLJ, Voss SD, Dunning P, Snay E, Fahey F, Smith SV, et al. Imaging cancer using PET -- the effect of the bifunctional chelator on the biodistribution of a ^{64}Cu-labeled antibody. Nucl Med Biol. 2011;38:29-38.

[56] Liu Z, Cai W, He L, Nakayama N, Chen K, Sun X, et al. In vivo biodistribution and highly efficient tumour targeting of carbon nanotubes in mice. Nat Nanotechnol. 2007;2:47-52.

[57] Cai W, Chen K, Li ZB, Gambhir SS, Chen X. Dual-function probe for PET and near-infrared fluorescence imaging of tumor vasculature. J Nucl Med. 2007;48:1862–70.

[58] Cai W, Chen X. Preparation of peptide conjugated quantum dots for tumour vasculature targeted imaging. Nat Protoc. 2008;3:89-96.

[59] Cai W, Chen X. Multimodality molecular imaging of tumor angiogenesis. J Nucl Med. 2008;49 Suppl 2:113S-28S.

[60] Cai W, Shin DW, Chen K, Gheysens O, Cao Q, Wang SX, et al. Peptide-labeled near-infrared quantum dots for imaging tumor vasculature in living subjects. Nano Lett. 2006;6:669-76.

[61] Liu Z, Robinson JT, Sun X, Dai H. PEGylated nanographene oxide for delivery of water-insoluble cancer drugs. J Am Chem Soc. 2008;130:10876-7.

[62] Tang LA, Wang J, Loh KP. Graphene-based SELDI probe with ultrahigh extraction and sensitivity for DNA oligomer. J Am Chem Soc. 2010;132:10976-7.

[63] Zhou M, Zhang R, Huang M, Lu W, Song S, Melancon MP, et al. A chelator-free multifunctional [64Cu]CuS nanoparticle platform for simultaneous micro-PET/CT imaging and photothermal ablation therapy. J Am Chem Soc. 2010;132:15351-8.

[64] He S, Song B, Li D, Zhu C, Qi W, Wen Y, et al. A Graphene Nanoprobe for Rapid, Sensitive, and Multicolor Fluorescent DNA Analysis. Adv Funct Mater. 2010;20:453-9.

[65] Yang K, Hu L, Ma X, Ye S, Cheng L, Shi X, et al. Multimodal imaging guided photothermal therapy using functionalized graphene nanosheets anchored with magnetic nanoparticles. Adv Mater. 2012;24:1868-72.

[66] Miao W, Shim G, Lee S, Choe YS, Oh YK. Safety and tumor tissue accumulation of pegylated graphene oxide nanosheets for co-delivery of anticancer drug and photosensitizer. Biomaterials. 2013;34:3402-10.

[67] Shi S, Yang K, Hong H, Valdovinos HF, Nayak TR, Zhang Y, et al. Tumor vasculature targeting and imaging in living mice with reduced graphene oxide. Biomaterials. 2013;34:3002-9.

[68] Ferrara N. The role of VEGF in the regulation of physiological and pathological angiogenesis. EXS. 2005:209-31.

[69] Chen F, Zhang Y, Cai W. Molecular MRI of VEGFR-2 reveals intra-tumor and inter-tumor heterogeneity. Am J Nucl Med Mol Imaging. 2013;3:312-6.

[70] Sun ZC, Huang P, Tong G, Lin J, Jin A, Rong PF, et al. VEGF-loaded graphene oxide as theranostics for multi-modality imaging-monitored targeting therapeutic angiogenesis of ischemic muscle. Nanoscale. 2013;5:6857-66.

[71] El-Mousawi M, Tchistiakova L, Yurchenko L, Pietrzynski G, Moreno M, Stanimirovic D, et al. A vascular endothelial growth factor high affinity receptor 1-specific peptide with antiangiogenic activity identified using a phage display peptide library. J Biol Chem. 2003;278:46681-91.

[72] Yang K, Zhang S, Zhang G, Sun X, Lee ST, Liu Z. Graphene in mice: ultrahigh in vivo tumor uptake and efficient photothermal therapy. Nano Lett. 2010;10:3318-23.

[73] Yang K, Feng L, Hong H, Cai W, Liu Z. Preparation and functionalization of graphene nanocomposites for biomedical applications. Nat Protoc. 2013;8:2392-403.

[74] Imoukhuede PI, Popel AS. Expression of VEGF receptors on endothelial cells in mouse skeletal muscle. PLoS One. 2012;7:e44791.

[75] Willmann JK, Lutz AM, Paulmurugan R, Patel MR, Chu P, Rosenberg J, et al. Dual-targeted contrast agent for US assessment of tumor angiogenesis in vivo. Radiology. 2008;248:936-44.

[76] Orbay H, Zhang Y, Valdovinos HF, Song G, Hernandez R, Theuer CP, et al. Positron emission tomography imaging of CD105 expression in a rat myocardial infarction model with (64)Cu-NOTA-TRC105. Am J Nucl Med Mol Imaging. 2013;4:1-9.

[77] Lambrechts D, Lenz HJ, de Haas S, Carmeliet P, Scherer SJ. Markers of response for the antiangiogenic agent bevacizumab. J Clin Oncol. 2013;31:1219-30.

[78] Cai W, Chen K, Mohamedali KA, Cao Q, Gambhir SS, Rosenblum MG, et al. PET of vascular endothelial growth factor receptor expression. J Nucl Med. 2006;47:2048-56.

[79] Goel S, England CG, Chen F, Cai W. Positron emission tomography and nanotechnology: A dynamic duo for cancer theranostics. Adv Drug Deliv Rev. 2016.

[80] Michalet X, Pinaud FF, Bentolila LA, Tsay JM, Doose S, Li JJ, et al. Quantum dots for live cells, in vivo imaging, and diagnostics. Science. 2005;307:538-44.

[81] Schipper ML, Cheng Z, Lee SW, Bentolila LA, Iyer G, Rao J, et al. microPET-based biodistribution of quantum dots in living mice. J Nucl Med. 2007;48:1511-8.

[82] Yang X, Hong H, Grailer JJ, Rowland IJ, Javadi A, Hurley SA, et al. cRGD-functionalized, DOX-conjugated, and (6)(4)Cu-labeled superparamagnetic iron oxide nanoparticles for targeted anticancer drug delivery and PET/MR imaging. Biomaterials. 2011;32:4151-60.

[83] Shi S, Yang K, Hong H, Chen F, Valdovinos HF, Goel S, et al. VEGFR targeting leads to significantly enhanced tumor uptake of nanographene oxide in vivo. Biomaterials. 2015;39:39-46.

[84] Frigell J, Garcia I, Gomez-Vallejo V, Llop J, Penades S. 68Ga-labeled gold glyconanoparticles for exploring blood-brain barrier permeability: preparation, biodistribution studies, and improved brain uptake via neuropeptide conjugation. J Am Chem Soc. 2014;136:449-57.

[85] Xie H, Wang ZJ, Bao A, Goins B, Phillips WT. In vivo PET imaging and biodistribution of radiolabeled gold nanoshells in rats with tumor xenografts. Int J Pharm. 2010;395:324-30.

[86] Chen F, Hong H, Zhang Y, Valdovinos HF, Shi S, Kwon GS, et al. In vivo tumor targeting and image-guided drug delivery with antibody-conjugated, radiolabeled mesoporous silica nanoparticles. ACS Nano. 2013;7:9027-39.

[87] Zhang Y, Jeon M, Rich LJ, Hong H, Geng J, Shi S, et al. Non-invasive multimodal functional imaging of the intestine with frozen micellar naphthalocyanines. Nat Nanotechnol. 2014;9:631-8.

[88] Rossin R, Muro S, Welch MJ, Muzykantov VR, Schuster DP. In vivo imaging of 64Cu-labeled polymer nanoparticles targeted to the lung endothelium. J Nucl Med. 2008;49:103-11.

[89] Price EW, Orvig C. Matching chelators to radiometals for radiopharmaceuticals. Chem Soc Rev. 2014;43:260-90.

[90] Albanese A, Tang PS, Chan WC. The effect of nanoparticle size, shape, and surface chemistry on biological systems. Annu Rev Biomed Eng. 2012;14:1-16.

[91] Blanco E, Shen H, Ferrari M. Principles of nanoparticle design for overcoming biological barriers to drug delivery. Nat Biotechnol. 2015;33:941-51.

[92] Wilhelm S, Tavares AJ, Dai Q, Ohta S, Audet J, Dvorak HF, et al. Analysis of nanoparticle delivery to tumours. Nature Reviews Materials. 2016;1:16014.

[93] Stasiuk GJ, Long NJ. The ubiquitous DOTA and its derivatives: the impact of 1,4,7,10-tetraazacyclododecane-1,4,7,10-tetraacetic acid on biomedical imaging. Chem Commun (Camb). 2013;49:2732-46.

[94] Cox JPL, Craig AS, Helps IM, Jankowski KJ, Parker D, Eaton MAW, et al. Synthesis of C- and N-functionalised derivatives of 1,4,7-triazacyclononane-1,4,7-triyltriacetic acid (NOTA), 1,4,7,10-tetra-azacyclododecane-1,4,7,10-tetrayltetra-acetic acid (DOTA), and diethylenenetriaminepenta-acetic acid (DTPA): bifunctional complexing agents for the derivatisation of antibodies. Journal of the Chemical Society, Perkin Transactions 1. 1990:2567-76.

[95] Goel S, Chen F, Ehlerding EB, Cai W. Intrinsically radiolabeled nanoparticles: an emerging paradigm. Small. 2014;10:3825-30.

[96] Sun X, Cai W, Chen X. Positron emission tomography imaging using radiolabeled inorganic nanomaterials. Acc Chem Res. 2015;48:286-94.

[97] Shi S, Fliss BC, Gu Z, Zhu Y, Hong H, Valdovinos HF, et al. Chelator-Free Labeling of Layered Double Hydroxide Nanoparticles for in Vivo PET Imaging. Sci Rep. 2015;5:16930.

[98] Wadas TJ, Wong EH, Weisman GR, Anderson CJ. Copper chelation chemistry and its role in copper radiopharmaceuticals. Curr Pharm Des. 2007;13:3-16.

[99] Shekar SC, Swathi RS. Cation−π Interactions and Rattling Motion through Two-Dimensional Carbon Networks: Graphene vs Graphynes. J Phys Chem C. 2015;119:8912-23.

[100] Ma L, Koka J, Stace AJ, Cox H. Gas phase UV spectrum of a Cu(II)-bis(benzene) sandwich complex: experiment and theory. J Phys Chem A. 2014;118:10730-7.

[101] Yi HB, Lee HM, Kim KS. Interaction of Benzene with Transition Metal Cations: Theoretical Study of Structures, Energies, and IR Spectra. J Chem Theory Comput. 2009;5:1709-17.

[102] Hong H, Severin GW, Yang Y, Engle JW, Zhang Y, Barnhart TE, et al. Positron emission tomography imaging of CD105 expression with 89Zr-Df-TRC105. Eur J Nucl Med Mol Imaging. 2012;39:138-48.

[103] Shi S, Orbay H, Yang Y, Graves SA, Nayak TR, Hong H, et al. PET Imaging of Abdominal Aortic Aneurysm with 64Cu-Labeled Anti-CD105 Antibody Fab Fragment. J Nucl Med. 2015;56:927-32.

[104] Cooper MS, Ma MT, Sunassee K, Shaw KP, Williams JD, Paul RL, et al. Comparison of (64)Cu-complexing bifunctional chelators for radioimmunoconjugation: labeling efficiency, specific activity, and in vitro/in vivo stability. Bioconjug Chem. 2012;23:1029-39.

[105] Zhang L, Xia J, Zhao Q, Liu L, Zhang Z. Functional Graphene Oxide as a Nanocarrier for Controlled Loading and Targeted Delivery of Mixed Anticancer Drugs. Small. 2010;6:537-44.

[106] Kim H, Lee D, Kim J, Kim T-i, Kim WJ. Photothermally Triggered Cytosolic Drug Delivery via Endosome Disruption Using a Functionalized Reduced Graphene Oxide. ACS Nano. 2013;7:6735-46.

[107] Yang X, Zhang X, Liu Z, Ma Y, Huang Y, Chen Y. High-Efficiency Loading and Controlled Release of Doxorubicin Hydrochloride on Graphene Oxide. J Phys Chem C. 2008;112:17554-8.

[108] Kim C, Favazza C, Wang LV. In Vivo Photoacoustic Tomography of Chemicals: High-Resolution Functional and Molecular Optical Imaging at New Depths. Chem Rev. 2010;110:2756-82.

[109] Ntziachristos V. Going deeper than microscopy: the optical imaging frontier in biology. Nat Meth. 2010;7:603-14.

[110] Wang LV, Hu S. Photoacoustic tomography: in vivo imaging from organelles to organs. Science. 2012;335:1458-62.

[111] Nie L, Chen X. Structural and functional photoacoustic molecular tomography aided by emerging contrast agents. Chem Soc Rev. 2014;43:7132-70.

[112] Weber J, Beard PC, Bohndiek SE. Contrast agents for molecular photoacoustic imaging. Nat Methods. 2016;13:639-50.

[113] Zhang Y, Hong H, Engle JW, Yang Y, Barnhart TE, Cai W. Positron Emission Tomography and Near-Infrared Fluorescence Imaging of Vascular Endothelial Growth Factor with Dual-Labeled Bevacizumab. Am J Nucl Med Mol Imaging. 2012;2:1-13.

[114] Cai W, Wu Y, Chen K, Cao Q, Tice DA, Chen X. In vitro and in vivo characterization of 64Cu-labeled Abegrin, a humanized monoclonal antibody against integrin alpha v beta 3. Cancer Res. 2006;66:9673-81.

[115] Luo H, Hernandez R, Hong H, Graves SA, Yang Y, England CG, et al. Noninvasive brain cancer imaging with a bispecific antibody fragment, generated via click chemistry. Proc Natl Acad Sci U S A. 2015;112:12806-11.

[116] Yang Y, Hernandez R, Rao J, Yin L, Qu Y, Wu J, et al. Targeting CD146 with a 64Cu-labeled antibody enables in vivo immunoPET imaging of high-grade gliomas. Proc Natl Acad Sci U S A. 2015;112:E6525-34.

[117] Aryal S, Key J, Stigliano C, Landis MD, Lee DY, Decuzzi P. Positron emitting magnetic nanoconstructs for PET/MR imaging. Small. 2014;10:2688-96.

[118] Bagri A, Mattevi C, Acik M, Chabal YJ, Chhowalla M, Shenoy VB. Structural evolution during the reduction of chemically derived graphene oxide. Nat Chem. 2010;2:581-7.

[119] Lin LC, Grossman JC. Atomistic understandings of reduced graphene oxide as an ultrathin-film nanoporous membrane for separations. Nat Commun. 2015;6:8335.

[120] Peng F, Lu X, Janisse J, Muzik O, Shields AF. PET of human prostate cancer xenografts in mice with increased uptake of 64CuCl2. J Nucl Med. 2006;47:1649-52.

[121] Qin C, Liu H, Chen K, Hu X, Ma X, Lan X, et al. Theranostics of malignant melanoma with 64CuCl2. J Nucl Med. 2014;55:812-7.

[122] Kim KI, Jang SJ, Park JH, Lee YJ, Lee TS, Woo KS, et al. Detection of increased 64Cu uptake by human copper transporter 1 gene overexpression using PET with 64CuCl2 in human breast cancer xenograft model. J Nucl Med. 2014;55:1692-8.

[123] Wong RM, Gilbert DA, Liu K, Louie AY. Rapid size-controlled synthesis of dextran-coated, 64Cu-doped iron oxide nanoparticles. ACS Nano. 2012;6:3461-7.

[124] Zhao Y, Sultan D, Detering L, Cho S, Sun G, Pierce R, et al. Copper-64-alloyed gold nanoparticles for cancer imaging: improved radiolabel stability and diagnostic accuracy. Angew Chem Int Ed Engl. 2014;53:156-9.

[125] Burke BP, Baghdadi N, Kownacka AE, Nigam S, Clemente GS, Al-Yassiry MM, et al. Chelator free gallium-68 radiolabelling of silica coated iron oxide nanorods via surface interactions. Nanoscale. 2015;7:14889-96.

[126] Chakravarty R, Valdovinos HF, Chen F, Lewis CM, Ellison PA, Luo H, et al. Intrinsically germanium-69-labeled iron oxide nanoparticles: synthesis and in-vivo dual-modality PET/MR imaging. Adv Mater. 2014;26:5119-23.

[127] Chen F, Ellison PA, Lewis CM, Hong H, Zhang Y, Shi S, et al. Chelator-free synthesis of a dual-modality PET/MRI agent. Angew Chem Int Ed Engl. 2013;52:13319-23.

[128] Chen F, Goel S, Valdovinos HF, Luo H, Hernandez R, Barnhart TE, et al. In Vivo Integrity and Biological Fate of Chelator-Free Zirconium-89-Labeled Mesoporous Silica Nanoparticles. ACS Nano. 2015;9:7950-9.

[129] Xu ZP, Jin YG, Liu SM, Hao ZP, Lu GQ. Surface charging of layered double hydroxides during dynamic interactions of anions at the interfaces. J Colloid Interf Sci. 2008;326:522-9.

[130] Wang Q, O'Hare D. Recent advances in the synthesis and application of layered double hydroxide (LDH) nanosheets. Chem Rev. 2012;112:4124-55.

[131] Kura AU, Hussein MZ, Fakurazi S, Arulselvan P. Layered double hydroxide nanocomposite for drug delivery systems; bio-distribution, toxicity and drug activity enhancement. Chem Cent J. 2014;8:47.

[132] Xu ZP, Kurniawan ND, Bartlett PF, Lu GQ. Enhancement of relaxivity rates of Gd-DTPA complexes by intercalation into layered double hydroxide nanoparticles. Chemistry. 2007;13:2824-30.

[133] Kim SY, Oh JM, Lee JS, Kim TJ, Choy JH. Gadolinium (III) diethylenetriamine pentaacetic acid/ layered double hydroxide nanohybrid as novel T1-magnetic resonant nanoparticles. J Nanosci Nanotechnol. 2008;8:5181-4.

[134] Wang L, Xing H, Zhang S, Ren Q, Pan L, Zhang K, et al. A Gd-doped Mg-Al-LDH/Au nanocomposite for CT/MR bimodal imagings and simultaneous drug delivery. Biomaterials. 2013;34:3390-401.

[135] Chen C, Yee LK, Gong H, Zhang Y, Xu R. A facile synthesis of strong near infrared fluorescent layered double hydroxide nanovehicles with an anticancer drug for tumor optical imaging and therapy. Nanoscale. 2013;5:4314-20.

[136] Li D, Zhang YT, Yu M, Guo J, Chaudhary D, Wang CC. Cancer therapy and fluorescence imaging using the active release of doxorubicin from MSPs/Ni-LDH folate targeting nanoparticles. Biomaterials. 2013;34:7913-22.

[137] Lee JH, Jung DY, Kim E, Ahn TK. Fluorescein dye intercalated layered double hydroxides for chemically stabilized photoluminescent indicators on inorganic surfaces. Dalton Trans. 2014;43:8543-8.

[138] Yoo SS, Razzak R, Bedard E, Guo L, Shaw AR, Moore RB, et al. Layered gadolinium-based nanoparticle as a novel delivery platform for microRNA therapeutics. Nanotechnology. 2014;25:425102.

[139] Cutler CS, Hennkens HM, Sisay N, Huclier-Markai S, Jurisson SS. Radiometals for combined imaging and therapy. Chem Rev. 2013;113:858-83.

[140] Zhou JZ, Liang Y, Zhang J, Li L, Xu Y, Ruan X, et al. Quick and efficient co-treatment of Zn(2+)/Ni(2+) and CN(-) via the formation of Ni(CN)4(2-) intercalated larger ZnAl-LDH crystals. J Hazard Mater. 2014;279:141-7.

[141] Xu ZP, Stevenson GS, Lu CQ, Lu GQ, Bartlett PF, Gray PP. Stable suspension of layered double hydroxide nanoparticles in aqueous solution. J Am Chem Soc. 2006;128:36-7.

[142] Xu ZP, Stevenson G, Lu CQ, Lu GQ. Dispersion and size control of layered double hydroxide nanoparticles in aqueous solutions. J Phys Chem B. 2006;110:16923-9.

[143] Chakravarty R, Goel S, Valdovinos HF, Hernandez R, Hong H, Nickles RJ, et al. Matching the decay half-life with the biological half-life: ImmunoPET imaging with (44)Sc-labeled cetuximab Fab fragment. Bioconjug Chem. 2014;25:2197-204.

[144] van de Watering FC, Rijpkema M, Perk L, Brinkmann U, Oyen WJ, Boerman OC. Zirconium-89 labeled antibodies: a new tool for molecular imaging in cancer patients. Biomed Res Int. 2014;2014:203601.

[145] Deri MA, Zeglis BM, Francesconi LC, Lewis JS. PET imaging with (8)(9)Zr: from radiochemistry to the clinic. Nucl Med Biol. 2013;40:3-14.

[146] Polasek M, Hermann P, Peters JA, Geraldes CF, Lukes I. PAMAM dendrimers conjugated with an uncharged gadolinium(III) chelate with a fast water exchange: the influence of chelate charge on rotational dynamics. Bioconjug Chem. 2009;20:2142-53.

[147] Chakravarty R, Valdovinos HF, Chen F, Lewis CM, Ellison PA, Luo H, et al. Intrinsically Germanium-69-Labeled Iron Oxide Nanoparticles: Synthesis and In Vivo Dual-Modality PET/MR Imaging. Adv Mater. 2014.

[148] Dutta D, Vasudevan S. Accommodating unwelcome guests in inorganic layered hosts: inclusion of chloranil in a layered double hydroxide. Inorg Chem. 2012;51:8064-72.

[149] Alexa IF, Popovici RF, Ignat M, Popovici E, Voicu VA. Non-Toxic Nanocomposite Containing Captopril Intercalated into Green Inorganic Carrier. Dig J Nanomater Biostruct. 2011;6:1091-101.

[150] Choi SJ, Lee JK, Jeong J, Choy JH. Toxicity evaluation of inorganic nanoparticles: considerations and challenges. Mol Cell Toxicol. 2013;9:205-10.

[151] Kura AU, Hussein-Al-Ali SH, Hussein MZ, Fakurazi S. Preparation of Tween 80-Zn/Al-levodopa-layered double hydroxides nanocomposite for drug delivery system. ScientificWorldJournal. 2014;2014:104246.

[152] Yan M, Zhang Z, Cui S, Lei M, Zeng K, Liao Y, et al. Improvement of pharmacokinetic and antitumor activity of layered double hydroxide nanoparticles by coating with PEGylated phospholipid membrane. Int J Nanomedicine. 2014;9:4867-78.

[153] Brown RO, Morgan LM, Bhattacharya SK, Johnson PL, Minard G, Dickerson RN. Potential aluminum exposure from parenteral nutrition in patients with acute kidney injury. Ann Pharmacother. 2008;42:1410-5.

[154] Proudfoot AT. Aluminium and zinc phosphide poisoning. Clin Toxicol (Phila). 2009;47:89-100.

[155] Yue CS, Christie M, Lavergne V, Sikaneta T, Taskapan H, Mardini K, et al. Aluminum toxicokinetics in peritoneal dialysis patients. Clin Toxicol (Phila). 2011;49:659-63.

[156] Novoselov K, Jiang D, Schedin F, Booth T, Khotkevich V, Morozov S, et al. Two-dimensional atomic crystals. Proc Natl Acad Sci USA. 2005;102:10451-3.

[157] Butler SZ, Hollen SM, Cao L, Cui Y, Gupta JA, Gutiérrez HR, et al. Progress, Challenges, and Opportunities in Two-Dimensional Materials Beyond Graphene. ACS Nano. **2013**;7:2898-926.

[158] Huang X, Zeng Z, Zhang H. Metal dichalcogenide nanosheets: preparation, properties and applications. Chem Soc Rev. **2013**;42:1934-46.

[159] Wang QH, Kalantar-Zadeh K, Kis A, Coleman JN, Strano MS. Electronics and optoelectronics of two-dimensional transition metal dichalcogenides. Nat Nanotechnol. 2012;7:699-712.

[160] Peng H, Dang W, Cao J, Chen Y, Wu D, Zheng W, et al. Topological insulator nanostructures for near-infrared transparent flexible electrodes. Nat Chem. 2012;4:281-6.

[161] Yin Z, Li H, Li H, Jiang L, Shi Y, Sun Y, et al. Single-layer MoS2 phototransistors. ACS Nano. 2011;6:74-80.

[162] Soon JM, Loh KP. Electrochemical double-layer capacitance of MoS2 nanowall films. Electrochem Solid St. 2007;10:A250-A4.

[163] Du G, Guo Z, Wang S, Zeng R, Chen Z, Liu H. Superior stability and high capacity of restacked molybdenum disulfide as anode material for lithium ion batteries. Chem Commun. 2010;46:1106-8.

[164] Chhowalla M, Shin HS, Eda G, Li L-J, Loh KP, Zhang H. The chemistry of two-dimensional layered transition metal dichalcogenide nanosheets. Nat Chem. 2013;5:263-75.

[165] Chianelli RR, Siadati MH, De la Rosa MP, Berhault G, Wilcoxon JP, Bearden Jr R, et al. Catalytic properties of single layers of transition metal sulfide catalytic materials. Catal Rev. 2006;48:1-41.

[166] Chou SS, De M, Kim J, Byun S, Dykstra C, Yu J, et al. Ligand Conjugation of Chemically Exfoliated MoS2. J Am Chem Soc. 2013;135:4584-7.

[167] Chou SS, Kaehr B, Kim J, Foley BM, De M, Hopkins PE, et al. Chemically Exfoliated MoS2 as Near-Infrared Photothermal Agents. Angew Chem. 2013;125:4254 -8.

[168] Cheng L, Liu J, Gu X, Gong H, Shi X, Liu T, et al. Imaging: PEGylated WS2 Nanosheets as a Multifunctional Theranostic Agent for in vivo Dual-Modal CT/Photoacoustic Imaging Guided Photothermal Therapy (Adv. Mater. 12/2014). Adv Mater. 2014;26:1794-.

[169] Li J, Jiang F, Yang B, Song X-R, Liu Y, Yang H-H, et al. Topological insulator bismuth selenide as a theranostic platform for simultaneous cancer imaging and therapy. Sci Rep. 2013;3.

[170] Zhu C, Zeng Z, Li H, Li F, Fan C, Zhang H. Single-Layer MoS2-Based Nanoprobes for Homogeneous Detection of Biomolecules. J Am Chem Soc. 2013;135:5998-6001.

[171] Liu T, Wang C, Gu X, Gong H, Cheng L, Shi X, et al. Drug Delivery with PEGylated MoS2 Nano-sheets for Combined Photothermal and Chemotherapy of Cancer. Adv Mater. 2014.

[172] Liu T, Wang C, Cui W, Gong H, Liang C, Shi X, et al. Combined photothermal and photodynamic therapy delivered by PEGylated MoS 2 nanosheets. Nanoscale. 2014;6:11219-25.

[173] Judenhofer MS, Wehrl HF, Newport DF, Catana C, Siegel SB, Becker M, et al. Simultaneous PET-MRI: a new approach for functional and morphological imaging. Nat Med. 2008;14:459-65.

[174] Kim J, Piao Y, Hyeon T. Multifunctional nanostructured materials for multimodal imaging, and simultaneous imaging and therapy. Chem Soc Rev. 2009;38:372-90.

[175] Qin C, Cheng K, Chen K, Hu X, Liu Y, Lan X, et al. Tyrosinase as a multifunctional reporter gene for Photoacoustic/MRI/PET triple modality molecular imaging. Sci Rep. 2013;3.

[176] Chen Q, Liang C, Wang X, He J, Li Y, Liu Z. An albumin-based theranostic nano-agent for dual-modal imaging guided photothermal therapy to inhibit lymphatic metastasis of cancer post surgery. Biomaterials. 2014;35:9355-62.

[177] Sumer B, Gao J. Theranostic nanomedicine for cancer. Nanomedicine (Lond). 2008;3:137-40.

[178] Liu Y, Yin J-J, Nie Z. Harnessing the collective properties of nanoparticle ensembles for cancer theranostics. Nano Res. 2014:1-12.

[179] Xie J, Lee S, Chen X. Nanoparticle-based theranostic agents. Adv Drug Deliv Rev. 2010;62:1064-79.

[180] Cheng L, Yang K, Li Y, Chen J, Wang C, Shao M, et al. Facile Preparation of Multifunctional Upconversion Nanoprobes for Multimodal Imaging and Dual-Targeted Photothermal Therapy. Angew Chem. 2011;123:7523-8.

[181] Hong H, Yang K, Zhang Y, Engle JW, Feng L, Yang Y, et al. In vivo targeting and imaging of tumor vasculature with radiolabeled, antibody-conjugated nanographene. ACS Nano. 2012;6:2361-70.

[182] Zhang Y, Hong H, Severin GW, Engle JW, Yang Y, Goel S, et al. ImmunoPET and near-infrared fluorescence imaging of CD105 expression using a monoclonal antibody dual-labeled with 89Zr and IRDye 800CW. Am J Transl Res. 2012;4:333-46.

[183] Hong H, Zhang Y, Severin GW, Yang Y, Engle JW, Niu G, et al. Multimodality imaging of breast cancer experimental lung metastasis with bioluminescence and a monoclonal antibody dual-labeled with 89Zr and IRDye 800CW. Mol Pharm. 2012;9:2339-49.

[184] Coleman JN, Lotya M, O'Neill A, Bergin SD, King PJ, Khan U, et al. Two-dimensional nanosheets produced by liquid exfoliation of layered materials. Science. **2011**;331:568-71.

[185] Huang X, Zeng Z, Bao S, Wang M, Qi X, Fan Z, et al. Solution-phase epitaxial growth of noble metal nanostructures on dispersible single-layer molybdenum disulfide nanosheets. Nat Commun. 2013;4:1444.

[186] Chen Y, Song B, Tang X, Lu L, Xue J. Ultrasmall Fe3O4 Nanoparticle/MoS2 Nanosheet Composites with Superior Performances for Lithium Ion Batteries. Small. 2014;10:1536-43.

[187] Liu T, Shi S, Liang C, Shen S, Cheng L, Wang C, et al. Iron oxide decorated MoS2 nanosheets with double PEGylation for chelator-free radiolabeling and multimodal imaging guided photothermal therapy. ACS Nano. 2015;9:950-60.

[188] Moghimi SM, Hunter C. Capture of stealth nanoparticles by the body's defences. Crit Rev Ther Drug Carrier Syst. 2001;18.

[189] Rosencwaig A, Gersho A. Theory of the photoacoustic effect with solids. J Appl Phys. 1976;47:64-9.

[190] Sun X, Liu Z, Welsher K, Robinson JT, Goodwin A, Zaric S, et al. Nano-Graphene Oxide for Cellular Imaging and Drug Delivery. Nano Res. 2008;1:203-12.

[191] Zhang W, Guo ZY, Huang DQ, Liu ZM, Guo X, Zhong HQ. Synergistic effect of chemo-photothermal therapy using PEGylated graphene oxide. Biomaterials. 2011;32:8555-61.

[192] Wen H, Dong C, Dong H, Shen A, Xia W, Cai X, et al. Engineered redox-responsive PEG detachment mechanism in PEGylated nano-graphene oxide for intracellular drug delivery. Small. 2012;8:760-9.

[193] Sahoo NG, Bao HQ, Pan YZ, Pal M, Kakran M, Cheng HKF, et al. Functionalized carbon nanomaterials as nanocarriers for loading and delivery of a poorly water-soluble anticancer drug: a comparative study. Chem Commun (Camb). 2011;47:5235-7.

[194] Bao HQ, Pan YZ, Ping Y, Sahoo NG, Wu TF, Li L, et al. Chitosan-Functionalized Graphene Oxide as a Nanocarrier for Drug and Gene Delivery. Small. 2011;7:1569-78.

[195] Shi S, Hong H, Orbay H, Graves SA, Yang Y, Ohman JD, et al. ImmunoPET of tissue factor expression in triple-negative breast cancer with a radiolabeled antibody Fab fragment. Eur J Nucl Med Mol Imaging. 2015;42:1295-303.

[196] Shi S, Chen F, Cai W. Biomedical applications of functionalized hollow mesoporous silica nanoparticles: focusing on molecular imaging. Nanomedicine (Lond). 2013;8:2027-39.